

**The Impact of Renewable Power Generation and
Extreme Weather Events on the Stability and
Resilience of AC Power Grids**

DISSERTATION

zur Erlangung des akademischen Grades

doctor rerum naturalium

(Dr. rer. nat.)

im Fach: Physik

Spezialisierung: Theoretische Physik

eingereicht an der
Mathematisch-Naturwissenschaftlichen Fakultät
der Humboldt-Universität zu Berlin

von
M.Sc. Anton Plietzsch

Präsident (komm.) der Humboldt-Universität zu Berlin:
Prof. Dr. Peter Frensch

Dekanin der Mathematisch-Naturwissenschaftlichen Fakultät:
Prof. Dr. Caren Tischendorf

Gutachter/innen:

1. Prof. Dr. Dr. h.c. mult. Jürgen Kurths
2. Prof. Dr. Pedro Lind
3. Prof. Dr. Joachim Peinke

Tag der mündlichen Prüfung: 15.09.2022

Abstract

The electricity system is undergoing a fundamental transition as fossil power plants are steadily replaced by renewable energy sources. This transformation comes with several challenges for maintaining the stability and resilience of the grid. On the one hand, wind and solar power are highly intermittent and can feed potentially strong fluctuations into the grid. At the same time, the replacement of synchronous generators with inverter-interfaced generation units creates a need for implementing grid-forming inverter controls, in order to maintain resilience against short-term disruptions. Additionally, the electricity infrastructure needs to be protected against extreme weather events that are becoming both more severe and more frequent as the climate crisis progresses.

The first part of this thesis addresses the question which impact short-term renewable fluctuations have on the synchronous grid frequency. For this purpose, a linear response theory for stochastic perturbations of networked dynamical systems is derived. This theory is then used to analyze impact of short-term wind and solar fluctuations on the grid frequency. Since the power spectral density of such fluctuations is highest at low frequencies, the frequency response of the system is dominated by a single eigenmode which corresponds to a quasi-static variation of the synchronous grid frequency. While the network frequency response is mainly homogenous, it is shown that due to transmission line losses, the susceptibility to power fluctuations is increasing along the power flow. This effect was previously observed in simulations of renewable microgrids but has been unexplained so far.

The second part of the thesis is concerned with modeling grid-forming inverter controls. While various detailed control schemes have been proposed in the engineering literature, a universal model for studying the collective dynamics of such systems has been lacking so far. By utilizing the inherent symmetry of the synchronous operating state, a normal form for grid-forming actors is derived. It is shown that this model provides a useful approximation of certain inverter control dynamics but is also well-suited for a data-driven modeling approach. The latter is proven by fitting the model to measurements of a grid-forming inverter that have been taken out in a microgrid lab.

The last part of the thesis deals with analyzing the risk of hurricane-induced power outages. High wind speeds often cause damage to transmission

infrastructure which can lead to overloads of other components and thereby induce a cascade of failures spreading through the entire grid. Simulations of such scenarios are implemented by combining a meteorological wind field model with a model for cascading line failures. Wind field simulations are based on historical hurricane track data. Wind-induced transmission line damages are modeled stochastically and overload failures are based on a static power flow analysis. Using Monte Carlo simulations in a synthetic test case resembling the Texas transmission system, it is possible to identify critical lines that trigger large-scale power outages. Finally, it is shown that by protecting only a small number of lines against wind damage, the resilience of the entire grid can be significantly enhanced.

Zusammenfassung

Das Stromsystem befindet sich momentan in einem grundlegenden Transformationsprozess, bei welchem fossile Kraftwerke schrittweise durch erneuerbare Energiequellen ersetzt werden. Dieser Prozess bringt auch Herausforderungen für die Aufrechterhaltung der Stabilität und Resilienz des Netzes mit sich. Zum einen ist die Wind- und Solarenergieerzeugung sehr unregelmäßig, was zu potenziell starken Leistungsschwankungen im Netz führen kann. Gleichzeitig werden Synchronmaschinen durch Wechselrichter-basierte Erzeuger ersetzt, wodurch ein Bedarf an netzbildenden Wechselrichterregelungen entsteht, um die Widerstandsfähigkeit des Netzes gegen kurzzeitige Störungen weiterhin sicherstellen können. Darüber hinaus muss die Netzinfrastuktur vor extremen Wetterereignissen geschützt werden, welche mit dem Fortschreiten der Klimakrise sowohl schwerer als auch häufiger zu werden drohen.

Der erste Teil dieser Arbeit beschäftigt sich mit der Frage, welchen Einfluss kurzzeitige Schwankungen der erneuerbaren Energiequellen auf die synchrone Netzfrequenz haben. Zu diesem Zweck wird eine lineare Antworttheorie für stochastische Störungen von dynamischen Systemen auf Netzwerken hergeleitet. Anschließend wird diese Theorie verwendet, um den Einfluss von kurzfristigen Wind- und Sonnenschwankungen auf die Netzdynamik zu analysieren. Da die spektrale Leistungsdichte solcher Schwankungen bei niedrigen Frequenzen am höchsten ist, wird die Frequenzantwort des Systems von nur einer einzigen Eigenmode dominiert, welche einer quasi-statischen Veränderung der synchronen Netzfrequenz entspricht. Während die Frequenzantwort des Netzes weitestgehend homogen ist, kann außerdem gezeigt werden, dass aufgrund von Leitungsverlusten die Anfälligkeit für Leistungsschwankungen entlang des Leistungsflusses zunimmt. Dieser Effekt wurde bereits zuvor in Simulationen von erneuerbaren Microgrids beobachtet, konnte aber bislang nicht erklärt werden.

Der zweite Teil der Arbeit befasst sich mit der Modellierung von netzbildenden Wechselrichterregelungen. Obwohl in der Ingenieursliteratur schon eine Vielzahl detaillierter Regelungskonzepte vorgeschlagen wurden, gab es bislang kein universelles Modell zur Beschreibung der kollektiven Dynamik solcher Systeme. Um dies zu erreichen, wird unter Ausnutzung der inhärenten Symmetrie des synchronen Betriebszustandes eine Normalform für netzbildende

Akteure abgeleitet. Anschließend wird gezeigt, dass dieses Modell eine gute Annäherung an typische Wechselrichter-Dynamiken bietet, aber auch für eine datengesteuerte Modellierung gut geeignet ist. Letzteres wird durch ein Fitting des Modells an Labor-Messungen eines netzbildenden Wechselrichters gezeigt.

Der letzte Teil der Arbeit befasst sich mit der Analyse des Risikos von Stromausfällen, welche durch Hurrikans verursacht werden. Hohe Windgeschwindigkeiten verursachen häufig Schäden an der Übertragungsinfrastruktur, welche wiederum zu Überlastungen anderer Komponenten führen und damit eine Kaskade von Ausfällen im gesamten Netz auslösen können. Simulationen solcher Szenarien werden durch die Kombination eines meteorologischen Windmodells sowie eines Modells für kaskadierende Leitungsausfälle durchgeführt. Die hierbei verwendeten Windsimulationen basieren auf historischen Hurrikan-Bewegungsdaten. Durch Wind verursachte Schäden an Übertragungsleitungen werden stochastisch modelliert und Leitungsüberlastungen mit einer statischen Leistungsflussanalyse berechnet. Durch Monte-Carlo-Simulationen in einer synthetischen Nachbildung des texanischen Übertragungsnetzes können einzelne kritische Leitungen identifiziert werden, welche zu großflächigen Stromausfällen führen. Abschließend wird gezeigt, dass die Resilienz des gesamten Netzes erheblich verbessert werden kann, indem nur eine kleine Anzahl von kritischen Leitungen besser vor Windschäden geschützt wird.

Contents

Abbreviations	xv
Nomenclature	xvii
1 Motivation & Introduction	1
1.1 Climate Crisis & the Global Energy Supply	1
1.2 Electricity Infrastructure & the Energy Transition	3
1.3 Challenges for the Stability and Resilience of Power Grids . . .	5
2 Modeling Complex Power Grids	7
2.1 AC Power Systems	7
2.1.1 3-Phase Systems	8
2.1.2 Per-Unit System	9
2.1.3 Ideal Circuit Elements	10
2.1.4 Grid Structure & Nodal Admittance Matrix	11
2.1.5 AC Power Flow Equations	12
2.1.6 Grid Frequency Control	13
2.2 Component Models	13
2.2.1 Line & Transformer Models	13
2.2.2 Load Models	14
2.2.3 Synchronous Generator Models	15
2.2.4 Inverter Control Models	17
2.3 Grid Models	19
2.3.1 Benchmark Test Cases	19
2.3.2 Data-Based Synthetic Test Cases	20
2.3.3 Randomly Generated Test Cases	20
3 Linear Response Theory for Complex Systems	23
3.1 Linear Time-Invariant Systems	24
3.1.1 Linear Response Theory	24
3.1.2 Signal and System Norms	25
3.2 Stochastic Inputs	27
3.2.1 Random Perturbations	27

3.2.2	Stochastic Processes	28
3.3	Eigenmode Analysis	30
3.3.1	Eigenmode Decomposition of the Transfer Function . . .	31
3.3.2	Single Mode Response Analysis	32
3.4	Systems on Network Structures	33
3.4.1	Network Laplacians	34
3.4.2	Dynamics with Diffusive Coupling	34
4	The Impact of Renewable Power Fluctuations	39
4.1	Variations of the Grid Frequency	39
4.1.1	The Role of Renewable Power Sources	41
4.1.2	Performance Measures for Frequency Fluctuations . . .	42
4.2	Renewable Power Fluctuations	43
4.2.1	Stochastic Wind Power Model	44
4.2.2	Stochastic Solar Power Model	45
4.3	Simulations of an AC Microgrid Model	46
4.4	Transport Losses on Power Lines	48
4.5	Linear Response of the Frequency	52
4.6	Simulations in the IEEE RTS-96 Test Case	56
4.7	Outlook: Multi-Bus Fluctuations & Optimal Control Schemes .	57
5	Measuring and Modeling Grid-Forming Inverters	59
5.1	The Role of Grid-Forming Inverters in Future Power Grids . .	60
5.2	Lab Measurements of Inverter Controls	61
5.2.1	Tecalia Inverter Models	61
5.2.2	Measurement & Simulation of an AC Microgrid	62
5.3	The Normal Form for Grid-Forming Actors	63
5.3.1	Modeling Assumptions	64
5.3.2	Normal Form Derivation	66
5.3.3	Relation to other Oscillator Models	67
5.3.4	Normal Form of a Droop Controlled Inverter	69
5.4	Data-Driven Normal Form Modeling	70
5.4.1	Inverter Measurements	70
5.4.2	Model Fitting	72
5.5	Outlook: Further Normal Form Applications	74
6	Hurricane-Induced Cascades of Line Failures	77
6.1	Hurricanes & Transmission System Resilience	78
6.2	Model for Wind-Induced Cascading Failures	79
6.2.1	Texas Synthetic Grid Model	79
6.2.2	Hurricane Wind Field Model	80
6.2.3	Probabilistic Line Fragility Model	81
6.2.4	DC Power Flow Model	83
6.2.5	Line Overload Model	84

6.2.6	Active Power Balance Control Model	84
6.2.7	Connecting the Sub-Models	85
6.3	Monte Carlo Simulation Results	85
6.4	Improving the Resilience of the Texas Grid	87
6.5	Outlook: Model Improvement & Economic Analysis	88
7	Summary & Discussion	93
7.1	Renewable Power Fluctuations	93
7.2	Modeling of Grid-Forming Inverters	94
7.3	Extreme Weather Events & Grid Resilience	95
A	Simulation Software	97
A.1	NetworkDynamics.jl	97
A.2	PowerDynamics.jl	98
A.3	PowerModels.jl	99
	References	101

List of Figures

2.1	Pi-model for transmission lines	14
2.2	Schematic picture of a synchronous generator	15
2.3	Block diagram of a PLL	18
2.4	Block diagram of a VSI control	19
4.1	Measurement of the grid frequency at different locations	41
4.2	Wind velocity and solar irradiance measurements	45
4.3	Frequency response in a microgrid simulation	48
4.4	Network topology of an AC Microgrid	49
4.5	Node response pattern for the microgrid simulation	54
4.6	Effect of Ohmic losses on power flow changes	55
4.7	Renewable power fluctuations in the IEEE RTS-96 network	58
5.1	Microgrid setup in the laboratory	63
5.2	Comparison of inverter measurements and simulations	64
5.3	Normal form approximation of a droop controlled inverter	70
5.4	Laboratory setup for measuring VSI dynamics	71
5.5	VSI current and voltage measurements	72
5.6	Fitting and validation of the normal form model	75
6.1	Storm tracks of tropical cyclones	80
6.2	2000-bus synthetic grid on the footprint of Texas	81
6.3	Modeled wind field of hurricane Harvey	82
6.4	Hurricane-induced cascading failure model	86
6.5	Outage probability of grid components for hurricane Harvey	90
6.6	Outage probability of grid components for hurricane Ike	91
6.7	20 most critical lines in the Texas synthetic grid	92
6.8	Power outage and cascade size probability distributions	92

List of Tables

2.1	Ideal circuit elements	10
2.2	Algebraic bus models	12
5.1	Normal form parameters of a droop controlled inverter	69
5.2	Fitted normal form parameters	74
6.1	Information on past hurricanes in Texas	79

Abbreviations

AC alternating current.

CCM current control mode.

CIGRE International Council on Large Electric Systems.

CSI current source inverter.

DAE Differential Algebraic Equation.

DC direct current.

DDE Delay Differential Equation.

EMF electromagnetic flux.

EMT electromagnetic transients.

HV high voltage.

HVDC high voltage direct current.

IBTrACS International Best Track Archive for Climate Stewardship.

IEEE Institute of Electrical and Electronics Engineers.

IPCC Intergovernmental Panel on Climate Change.

LHS left-hand side.

LTI linear time-invariant.

LV low voltage.

MIMO multiple-input-multiple-output.

MPPT maximum power point tracking.

MV mid voltage.

PIK Potsdam Institute for Climate Impact Research.

PLL phase-locked loop.

PV photovoltaic.

PWM pulse width modulation.

RES renewable energy sources.

RHS right-hand side.

RoCoF rate of change of frequency.

SDE Stochastic Differential Equation.

TSI total system inertia.

TSO transmission system operator.

VCM voltage control mode.

VOC virtual oscillator control.

VSI voltage source inverter.

Nomenclature

$\mathbf{G}(s)$	transfer function
$\mathbf{H}(t)$	response function
\mathbf{I}	identity matrix
\mathbf{L}	Laplacian matrix of a network
\mathbf{Y}	nodal admittance matrix
\cdot^\dagger	conjugate transpose of a vector or matrix
\cdot^T	transpose of a vector or matrix
\mathbb{C}	complex numbers
$\delta x(t)$	deviation of a dynamical variable $x(t)$ from a fixpoint
$\delta(\cdot)$	Dirac delta distribution
δ_{ij}	Kronecker delta
$\text{diag}(\cdot)$	diagonal matrix with diagonal entries given by a vector
\dot{x}	time derivative of a dynamical variable $x(t)$
\Im	imaginary part
$\ \cdot\ $	norm of a vector
$ \cdot $	cardinality of a set or modulus of a real or complex number
\mathbb{E}	expectation value of a random variable
\mathcal{E}	set of graph edges
\mathcal{G}	graph or network
\mathcal{V}	set of graph vertices or nodes
∇	nabla operator

ν	frequency in Fourier space
ω	phase angle frequency
\otimes	Kronecker product
\mathbb{R}	real numbers
\Re	real part
θ	voltage phase angle
$\Theta(\cdot)$	Heaviside function
$\text{tr}(\cdot)$	trace of a matrix
B	susceptance
C	capacitance
G	conductance
i	complex current
j	imaginary unit
L	inductance
P	active power
Q	reactive power
R	Ohmic resistance
S	complex power
t	time
u	complex voltate
V	voltage amplitude
X	reactance
x°	fixpoint of a dynamical variable $x(t)$

Chapter 1

Motivation & Introduction

1.1 Climate Crisis & the Global Energy Supply

The climate crisis is undoubtedly one of the biggest threats to humanity within the 21st century and beyond. Since the pre-industrial era, anthropogenic greenhouse gas emissions have steadily increased and according to the Intergovernmental Panel on Climate Change (IPCC), it is almost sure that they have been the dominant cause of the observed warming since the mid-20th century [93]. This human-induced climate change, which is accompanied by more frequent and intense extreme events, already has a widespread and severe impact on natural ecosystems, people, settlements, and infrastructure. Only substantial cuts in greenhouse gas emissions within the next few decades can limit global warming and substantially reduce further risks for both humanity and ecosystems [103]. In 2015, the vast majority of countries negotiated and ratified the Paris Agreement which sets the long-term goal to "hold the increase in the global average temperature to well below 2°C above pre-industrial levels and to pursue efforts to limit the temperature increase to 1.5 °C above pre-industrial levels" [135]. Regardless, in 2021 the global CO₂ emissions reached their highest level in history [59].

The major share of global greenhouse gas emissions can be attributed to the energy-related sectors (73 % in 2016) [108]. The energy use in industry accounts for 24 % of the total emissions, including the rather energy intense manufacturing of iron and steel (7 %). The emissions of the transport sector (16%) are dominated by road transport which accounts for 12 %. The energy used in buildings, comprising electricity, heating, and cooking, accounts for 18 % of the total emissions. To this day, the global energy mix of all these sectors is dominated by fossil energy sources. Hence, the global primary energy consumption still heavily relies on the fossil fuels coal (27 % in 2019), oil (33 %), and gas (24 %), whereas the share of renewable energy sources is only 11 %¹ [107]. To comply with the Paris Agreement, it is necessary to drastically

¹Here, primary energy is calculated using the substitution method that only considers the

increase the share of renewable energy sources within the next decades. The basic strategy for how this could be achieved is threefold:

1. Decarbonizing electricity: Replacement of fossil fuels by renewable energy sources in the electricity sector.
2. Sector coupling: Electrifying all other energy-related sectors (heating, transport, industry).
3. Energy sufficiency: Limiting or at least decelerating the growing global energy demand.

For the complete decarbonization of the electricity sector, there is still a long way to go. In 2020 the share of renewable energy sources in global electricity production was still only 29 %, compared to a 61 % share of fossil fuels [107]. With almost one sixth of global electricity generation in 2020, hydropower is by far the largest renewable source of electricity [29]. But while there is still some potential for further growth in hydropower capacity, it is certainly not enough to cover the major share of the global energy demand. Wind and solar on the other hand, account only for 5 % and 3 % of the global electricity generation but have a huge remaining potential to grow. By now, these energy sources have become economically competitive with conventional energy sources [107]. Particularly, solar is now consistently cheaper than building new coal and gas power plants in most countries [37]. However, for speeding up the transition process, it is necessary to abolish subsidies for fossil technologies and to introduce carbon prices [97].

Concerning the sector coupling, the situation is quite similar: From a technological perspective there already exist feasible solutions for the electrification of each sector, yet additional regulatory policies are needed to accelerate the transformation process. In the transport sector, it will be necessary to shift a lot of traffic from road to rail, since rail traffic already has a high degree of electrification. Further, cars with combustion engines need to be replaced by electric cars as soon as possible. In the heating sector, oil and gas heating has to be replaced by heat pumps. Some industry and transport sectors, such as the steel and cement industry as well as shipping and aviation, cannot be electrified directly. In these sectors, fossil fuels will have to be replaced by green hydrogen or hydrogen-based synthetic fuels. Here, the term green refers to production via water electrolysis using renewable energies, in contrast to brown hydrogen, which is produced by using natural gas as a base material. However, the production of hydrogen and synthetic fuels involves conversion losses and thus increases the need for primary energy. Hence, direct electrification is always cheaper than using hydrogen and synthetic fuels [58] and should therefore be applied where possible.

amount of usable energy and omits the conversion losses of fossil fuels.

An often overlooked aspect of the energy transition is energy sufficiency. To phase out fossil fuels as fast as possible, it is however necessary to limit the growth of the global energy demand. Since the pre-industrial era, the global energy demand has been drastically increasing and is still increasing today. This is due to both a strong growth in the world population as well as an increase in the per capita energy consumption [107, 80]. Since population projections indicate a stabilization of the world population within the next century [80], it would probably be sufficient to limit the global per capita energy consumption. Given the strong disparity of primary energy consumption between the global south and industrialized countries [107], particularly the latter have to put a lot of effort into stabilizing or even reducing their per capita energy consumption. Some European countries (e.g. Sweden, Germany, Denmark, and the UK) have already managed to stabilize or slightly reduce their energy demand from economic growth within the last 25 years² [107]. However, it should be mentioned that in 2019 the per capita primary energy consumption in Germany was still more than twice the global average [107]. Certainly, there is still a huge potential for saving energy in European or North American countries, particularly in the heating sector, e.g. by improving the insulation of houses and by using heat pumps, which are much more energy efficient than their conventional predecessor technologies [124]. However, introducing more efficient technologies and using cheaper energy sources always comes with the risk of rebound effects, i.e. an increase in energy demand. Moreover, the production of hydrogen and synthetic fuels is very energy intensive and will lead to a drastic increase in electricity demand [58]. Limiting the overall energy demand thus remains a difficult task.

1.2 Electricity Infrastructure & the Energy Transition

In the previous section, I explained how the decarbonization of the global energy system can be achieved. However, the energy transition is not just a replacement of fossil fuels with renewable energy sources, it also requires fundamental shifts in the structure and organization of the underlying infrastructure. This will most notably be the case for the electricity system which is becoming the backbone of the whole energy supply. And while there is enough scientific evidence that 100 % renewable energy electricity system is indeed feasible [31], it remains a great challenge to implement such a fundamental transition within a time frame of only a few decades while maintaining the security of supply.

Since the electrification in industrialized countries in the late 19th and early 20th centuries, power generation has been provided by a comparatively

²This even holds for the consumption-based energy use, that adjusts for the energy used to produce the goods that are imported and exported.

small number of large conventional generating units, such as coal, gas, and later also nuclear power plants. Today these conventional generators are for the most part connected to the high voltage (HV) transmission grid level, whereas the consumers, both private households and industry, are typically connected to the mid voltage (MV) and low voltage (LV) distribution grids. This results in a rather hierarchical structure where not only the majority of the power producing capacities but also the system control is implemented at the highest voltage level. Conventional power sources are dispatchable, which means they have a steady output of power that can be adjusted to the demand. On the timescale of minutes and hours, power generation is regulated by the electricity market, whereas on the timescale of seconds, the balancing between power production and demand is achieved in a decentralized manner by locally adjusting the power output of each generator proportionally to the changes in the grid frequency. This so-called primary control is feasible, as the functioning of AC power systems relies on a self-organized synchronization of all generating units where the deviation of the synchronous grid frequency from its nominal value reflects the mismatch between production and demand. Imbalances on even shorter timescales are buffered by drawing power from the kinetic energy that is stored in the large rotating masses of the generator turbines and serves as a momentary reserve.

With the transition towards an electricity system with a major share of renewable energy sources, some of these structural properties are going to change drastically. Although there exist offshore wind parks with an installed capacity similar to a coal or nuclear plant, most renewable generation units are much smaller and therefore typically installed in the distribution grid levels. This means that in future grids there will most probably be a much larger number of generating units and a significant shift of the generation to the lower voltage levels. Wind and solar generation units are connected to the grid via inverters. For these power electronic devices, there is no natural relation between power and frequency and any self-synchronizing and grid-stabilizing behavior has to be imposed by implementing additional control schemes. To this day, almost all inverter systems are controlled in a so-called grid-following mode that neither contributes to the primary control nor the momentary reserve.

Another important aspect that has to be considered is that wind and solar power production depends on meteorological conditions and are characterized by a rather intermittent in-feed on all time scales from seconds to seasons. At the same time, the electrification of the transport and heating sectors can lead to higher demand peaks, e.g. due to simultaneous loading of electric vehicles at certain daytimes, or because of larger heating or cooling energy demand at certain seasons. Given the increasing variability on both the demand and production side, the challenge of maintaining the global balance between power production and power demand at all timescales becomes increasingly

difficult. Generally, there are three complementary measures to achieve this goal: integrating more storage capacities, increasing demand flexibility, and expanding long-distance transmission capacities. Storage technologies on the shorter timescales (seconds to days) are capacitors, flywheels, and batteries. Seasonal variations can be compensated by building up reserves of synthetic gas that can be used as a backup for generating electricity in periods of high demand and low wind and solar generation [31]. The need for storage capacity can be reduced by increasing the demand-side flexibility, e.g. in industry and heating [51, 123]. There are several approaches to implement such demand-side management, e.g. through direct load control by utility companies (e.g. in the heating sector) or by real-time pricing on the electricity market [86]. An expansion of transmission grid capacities is necessary to connect regions of high production with those of high demand. The investment in new transmission infrastructure does not only facilitate the balancing of power generation and demand in the grid but can also lower the overall cost as it allows the installment of renewable generation units at the most profitable locations. Long-range connections also reduce the effects of local weather phenomena thereby the risks from insufficient renewable energy generation in certain areas. Such connections between different parts of a continental grid or even separate synchronous regions can be accomplished by using high voltage direct current (HVDC) lines which have a very low rate of power losses [11]. The integration of such lines requires inverters, similar to renewable generation units. From the technical point of view, there is certainly some degree of freedom in whether to put a stronger focus on the global grid expansion or the integration of local storage. The different degrees of decentralization come with different economic costs and social constraints that have to be weighed politically [2].

1.3 Challenges for the Stability and Resilience of Power Grids

In the previous section, I explained that the transformation of the electricity infrastructure is an intricate task that therefore requires expertise from various scientific disciplines. In recent years, some aspects such as the collective behavior of inverter-based systems, the impact of renewable fluctuations, or the risk of cascades of line failures have gained interest within the theoretical physics community, as they can be approached with the methodology of nonlinear dynamics, statistical physics, and complex systems science [142]. The aim of this thesis is to continue these approaches to address some of the key challenges concerning the stability and resilience of power grids with an increasing share of renewable energy sources under changing climatic conditions. Throughout the thesis I will particularly focus on the following challenges:

1. Wind and solar power production are fluctuating even on the time scale

of seconds. Within large wind parks or solar fields, these fluctuations can be highly correlated and may potentially add up to large fluctuations that are directly fed into the grid.

2. Synchronous generators will get replaced by a very large number of inverter-interfaced generation units, which will at least be partially equipped with a grid-forming control. Due to the lack of a universal model for the large variety of proposed control schemes, it is difficult to make general statements about the collective dynamics in such inverter-dominated grids.
3. As the climate crisis progresses, extreme weather events are becoming more severe and more frequent. In some regions, this may increase the risk of large-scale power outages by either imposing conditions where the transmission system is close to its capacity limits or even by direct damage to certain grid components.

The thesis is structured as follows. In Chapter 2 I introduce some fundamental concepts and models for power grids and their components. In Chapter 3 I derive a linear response theory for dynamical systems on network structures with stochastic inputs. In Chapter 4 this theory is then used to investigate the impact of wind and solar power fluctuations on the grid frequency. Here, a special focus is placed on the role that line losses play in the spreading of these fluctuations. In Chapter 5 I present measurements and simulations of a small microgrid setup with both grid-forming and grid-following inverter controls. Subsequently, I derive a normal form model for grid-forming components from first principles and show that this is suited to capture the dynamical behavior of the detailed grid-forming inverter control by fitting the model to measurement data. Finally, in Chapter 6 I introduce a model for wind-induced cascades of line failures and present results from Monte Carlo simulations of power outages in a synthetic grid on the footprint of Texas triggered by hurricane wind fields.

Chapter 2

Modeling Complex Power Grids

In this chapter, I introduce some fundamental concepts and models for AC power grids and their components that will be used in the subsequent chapters. The overview is kept as short as possible, as most concepts are covered in the standard power system engineering textbooks (e.g. [6, 78, 84, 110]). One exception to this is the section on inverter control models, a topic that has gained more attention only recently. Finally, I will also introduce data-based and randomly generated grid models that will be used in the subsequent chapters.

2.1 AC Power Systems

Today, the majority of power grids are alternating current (AC) systems. Historically, AC power systems prevailed over direct current (DC) systems for mainly two reasons. First, in AC systems it is possible to easily step the voltage up and down with the help of transformers. This is a major advantage because power losses at high voltages are much lower and therefore AC transmission systems have been much more convenient for efficiently transporting power over long distances. The second advantage is that circuit breaking in AC systems is much easier. AC voltage inverts several times per second and thus, AC circuits can easily be disconnected at a zero crossing. DC voltage on the other hand never crosses zero and therefore sophisticated circuit breakers have to be built to avoid arcing.

Nevertheless, DC transmission has had a comeback over the last decades, mainly in the form of high voltage direct current (HVDC) transmission lines. The integration of such lines into the high voltage level of an existing AC transmission system was enabled by the development of power electronic devices that convert between AC and DC. One advantage of these links is that they can transport power between AC systems that are not synchronized, e.g. between

the continental European grid and the British grid. Another important aspect is that in DC transmission lines there is no reactive power and therefore the power losses are smaller than in AC transmission lines at the same voltage level. HVDC lines are therefore particularly suitable for power transmission over continental scales [11].

Despite these developments, I will mainly focus on AC transmission grids in this thesis.

2.1.1 3-Phase Systems

Modern power grids are typically 3-phase systems. This means that both current and voltage signals have three independent phases

$$\mathbf{u}_{abc}(t) = \begin{bmatrix} u_a(t) \\ u_b(t) \\ u_c(t) \end{bmatrix}, \quad \mathbf{i}_{abc}(t) = \begin{bmatrix} i_a(t) \\ i_b(t) \\ i_c(t) \end{bmatrix}.$$

Assumption 2.1 (Balanced Phase). *For both voltage and current, the three phases are balanced such that*

$$\begin{aligned} i_a(t) + i_b(t) + i_c(t) &= 0, \\ u_a(t) + u_b(t) + u_c(t) &= 0. \end{aligned}$$

Remark. The assumption of balanced phases is usually valid as long as no fault breaks this symmetry, e.g. a phase-to-phase short circuit.

Such a balanced system can be written in terms of a time-dependent amplitude and a time-dependent phase variable

$$\mathbf{u}_{abc}(t) = V(t) \begin{bmatrix} \cos(\omega_s t + \theta(t)) \\ \cos(\omega_s t + \theta(t) - \frac{2\pi}{3}) \\ \cos(\omega_s t + \theta(t) + \frac{2\pi}{3}) \end{bmatrix}. \quad (2.1)$$

Here, ω_s is the synchronous frequency of the grid. When the system is in the steady state, both the amplitude and the angle are constant.

Definition 2.1 (Clarke-Transformation [41]). *The coordinate transformation from the abc-reference frame to the so-called $\alpha\beta\gamma$ -reference frame is defined as*

$$\mathbf{T}_{\alpha\beta\gamma} = \frac{2}{3} \begin{bmatrix} 1 & -\frac{1}{2} & -\frac{1}{2} \\ 0 & \frac{\sqrt{3}}{2} & -\frac{\sqrt{3}}{2} \\ \frac{1}{2} & \frac{1}{2} & \frac{1}{2} \end{bmatrix}.$$

Applying the Clarke transform to the balanced system (2.1) yields

$$\mathbf{u}_{\alpha\beta\gamma}(t) = \mathbf{T}_{\alpha\beta\gamma} \mathbf{u}_{abc}(t) = V(t) \begin{bmatrix} \cos(\omega_s t + \theta(t)) \\ \sin(\omega_s t + \theta(t)) \\ 0 \end{bmatrix}. \quad (2.2)$$

We see that the third component is always zero and the two independent components α and β remain. As an alternative representation we can rewrite (2.2) as a complex signal

$$u_{\alpha\beta}(t) = u_\alpha(t) + j \cdot u_\beta(t) = V(t)e^{j(\omega_s t + \theta(t))} . \quad (2.3)$$

Definition 2.2 (Park Transformation [95]). *The transformation from the complex $\alpha\beta$ -reference frame to the so-called complex dq -reference frame is defined as*

$$T_{dq}(\vartheta) = e^{-j\vartheta} .$$

With this definition, we can easily transform the complex voltage (2.3) into a reference frame that is co-rotating with the nominal grid frequency

$$u_{dq} = u_d + j \cdot u_q = T_{dq}(\omega_s t) u_{\alpha\beta}(t) = V(t)e^{j\theta(t)} .$$

We can apply the same transformations to the balanced three-phase current and get the complex current signal

$$i_{dq} = i_d + j \cdot i_q = I(t)e^{j\phi(t)} .$$

With these complex definitions of voltage and current, it is also straightforward to calculate the complex power

$$S = P + j \cdot Q = u \cdot i^* .$$

Active and reactive power in the dq -reference frame are then given by

$$\begin{aligned} P &= u_d \cdot i_d + u_q \cdot i_q , \\ Q &= u_q \cdot i_d + u_d \cdot i_q . \end{aligned}$$

2.1.2 Per-Unit System

In electrical engineering, it is common to express the system quantities in the so-called per-unit system. In this system, all electrical quantities are scaled by base values. For this, a base voltage V_{base} and a base power S_{base} are chosen and all other base values are derived from those two.

$$\begin{aligned} I_{base} &= \frac{S_{base}}{V_{base}} \\ Z_{base} &= \frac{V_{base}}{I_{base}} = \frac{V_{base}^2}{S_{base}} \\ Y_{base} &= \frac{1}{Z_{base}} = \frac{S_{base}}{V_{base}^2} \end{aligned}$$

Base values are real values that are used to scale the magnitude of complex variables. Phase angles are not affected by the conversion to the per-unit system.

Using the per-unit system has several advantages. It makes calculations easier and can also increase the stability of numerical calculations. But the main reason for using the per unit system is, that it significantly simplifies the handling of transformers. It can easily be shown that if the base voltages on both transformer sides are chosen according to the respective voltage levels, the per-unit values of voltage, current, and power are the same on both sides.

2.1.3 Ideal Circuit Elements

The electricity grid is composed of different electrical circuit elements. The dynamical and static behavior of realistic electrical elements can be modeled by combinations of ideal circuit elements.

Circuit Element	(Dynamic) Equation	Steady State Impedance
Ideal Resistor	$u = R \cdot i$	$Z = R$
Ideal Inductor	$L \cdot \frac{di}{dt} = u$	$Z = j\omega L$
Ideal Capacitor	$C \cdot \frac{du}{dt} = i$	$Z = \frac{1}{j\omega C}$

Table 2.1: Ideal circuit elements.

Inductive and capacitive elements have a transient dynamical behavior that is described by the two differential equations in Table 2.1. These so-called electromagnetic transients (EMT) are usually very fast and settle into a steady state where both current and voltage phasors oscillate with the nominal grid frequency ω_s and are related by the simple algebraic relation

$$u = jX \cdot i ,$$

where X is the capacitive or inductive reactance. This relation is similar to Ohm's law for ideal resistors, except for the additional factor j that corresponds to a phase shift $\frac{\pi}{2}$ between voltage and current. As a result, the steady-state behavior of any electrical component that is composed of the ideal circuit elements in Table 2.1 can be parametrized by a single complex parameter, the impedance

$$Z = R + jX .$$

The inverse of the impedance is the admittance $Y = Z^{-1}$.

In a conventional grid, electromagnetic transients are much faster than the electromechanical dynamics of the generators such that a time scale separation can be assumed. For inverter-based grids, this assumption is not necessarily true and electromagnetic transients might influence the grid stability [85]. However, EMT models drastically increase the number of dynamic equations and are also much harder to evaluate analytically and will therefore not be considered in this thesis.

2.1.4 Grid Structure & Nodal Admittance Matrix

The structure of electrical grids can be represented by a graph. A graph $\mathcal{G} = (\mathcal{V}, \mathcal{E})$ is a pair consisting of a set of nodes \mathcal{V} and a set of edges \mathcal{E} . In electrical engineering, the nodes are typically called buses and the edges are called branches. The state of each bus in an AC grid is defined by a voltage phasor. Components such as generators or loads are connected to one of the buses in the network. Additionally, each bus can have a connection to the ground which is commonly called the shunt. Branches on the other hand are connections between two buses in the grid. Such a connection can either be a power line or a transformer.

Definition 2.3 (Incidence Matrix). *The graph structure of the electrical grid can be represented by the so-called incidence matrix $B \in \mathbb{R}^{|\mathcal{V}| \times |\mathcal{E}|}$ which is defined as*

$$C_{ij} := \begin{cases} +1 & \text{if } j \text{ is an outgoing branch from bus } i \\ -1 & \text{if } j \text{ is an incoming branch to bus } i \\ 0 & \text{else .} \end{cases}$$

The particular definition of this matrix also introduced an orientation of the branches. The choice of these orientations is arbitrary and corresponds to a reference frame that defines a flow direction for every branch. Using the incidence matrix, we can write Kirchhoff's current law as

$$\mathbf{i} = \mathbf{i}^{sh} + \mathbf{C} \cdot \mathbf{i}^{br} , \quad (2.4)$$

where $\mathbf{i} \in \mathbb{R}^{|\mathcal{V}|}$ is the vector of current injections at the buses, $\mathbf{i}^{sh} \in \mathbb{R}^{|\mathcal{V}|}$ is the vector of shunt currents and $\mathbf{i}^{br} \in \mathbb{R}^{|\mathcal{E}|}$ is the vector of branch currents.

In the previous sections, I explained that all branch (and shunt) components that are composed of ideal resistors, inductances, capacitors, and transformers can in the steady state and in the per-unit system be described by an admittance Y . Introducing the diagonal matrices $\mathbf{Y}^{sh} = \text{diag}(\mathbf{y}^{sh})$ and $\mathbf{Y}^{br} = \text{diag}(\mathbf{y}^{br})$, the shunt and branch currents can be written as

$$\begin{aligned} \mathbf{i}^{sh} &= \mathbf{Y}^{sh} \cdot \mathbf{u}^{sh} , \\ \mathbf{i}^{br} &= \mathbf{Y}^{br} \cdot \mathbf{C}^T \cdot \mathbf{u} . \end{aligned} \quad (2.5)$$

Definition 2.4 (Nodal Admittance Matrix). *The nodal admittance matrix of the electrical grid is defined as*

$$\mathbf{Y} = \mathbf{Y}^{sh} + \mathbf{C} \cdot \mathbf{Y}^{br} \cdot \mathbf{C}^T . \quad (2.6)$$

Inserting (2.5) into (2.4) and using the definition of the nodal admittance matrix (2.6) yields the following relation between the nodal current injections and the bus voltages

$$\mathbf{i} = \mathbf{Y} \cdot \mathbf{u} .$$

2.1.5 AC Power Flow Equations

Using the results of the previous section, the complex power at a bus i is given by

$$S_i = P_i + jQ_i = u_i \cdot i_i^* = \sum_l u_i Y_{il}^* u_l^* . \quad (2.7)$$

The nodal conductance matrix \mathbf{G} and the nodal susceptance matrix \mathbf{B} are defined as the real and imaginary part of the nodal admittance matrix \mathbf{Y}

$$\mathbf{Y} = \mathbf{G} + j\mathbf{B} . \quad (2.8)$$

Inserting (2.8) into (2.7) and separating into real and imaginary parts yields the AC power flow equations

$$\begin{aligned} P_i &= \sum_j V_i V_j [G_{ij} \cos(\theta_{ij}) + B_{ij} \sin(\theta_{ij})] , \\ Q_i &= \sum_l V_i V_l [G_{il} \sin(\theta_{il}) - B_{il} \cos(\theta_{il})] . \end{aligned} \quad (2.9)$$

The state of each bus is determined by the four quantities active power P , reactive power Q , voltage magnitude V , and voltage angle θ . To solve the AC power flow equations, we have to determine which quantities are fixed and which are free variables for each bus in the grid. There are three different bus models:

Bus Model	Bus Type	Fixed Parameters	Free Variables
PQ -Bus	Load Bus	P, Q	V, θ
PV -Bus	Generator Bus	P, V	Q, θ
$V\theta$ -Bus	Slack Bus	V, θ	P, Q

Table 2.2: Algebraic bus models for solving the AC power flow equations.

Generally, generators are assumed to control their active power infeed into the grid, as well as the voltage amplitude hence they are modeled as PV -buses. However, in a grid with nonzero Ohmic line losses, at least one generator bus has to be modeled as a slack bus. The AC power flow equations only have a solution if the active power generation by all generators equals the total active power demand by all loads and the transport losses on the lines

$$\sum_{i \in \mathcal{V}_G} P_i = \sum_{i \in \mathcal{V}_L} P_i + \sum_{i \in \mathcal{E}} P_i^{loss} .$$

For both PQ and PV buses, the active power P is a fixed parameter. However, the transmission line losses P_i^{loss} depend on the voltage angles which are the

solutions to the power flow equations. Hence, there has to be at least one slack bus in the system that has the active power P as a free variable and which can therefore balance the uncertainty of the total line losses in the system. Often the generator with the largest power capacity is chosen to be modeled as a slack.

2.1.6 Grid Frequency Control

In real power systems, production has to be constantly adjusted to changes in demand. Due to the electromechanical design of synchronous generators, any global power imbalance leads to a change in the synchronous grid frequency. This fundamental property is utilized to control the grid frequency on the timescale of seconds to minutes in a completely decentralized manner. For this so-called primary frequency control, each generator adjusts its power linearly to the change in the global frequency

$$\Delta P_i = -D_i \cdot \Delta \omega_{global} .$$

This control scheme is implemented as a droop speed control of the generator turbine governors with a droop coefficient D_i . The ability of generators to adjust their power is limited by their capacity which is denoted as the *spinning reserve* [78].

2.2 Component Models

In this section, I will introduce the models for transmission lines, transformers, loads, generators, and inverters that will be used throughout this thesis.

2.2.1 Line & Transformer Models

Short transmission lines are typically modeled by the so-called π -model, which is depicted in Figure 2.1. Here, the term short line means that the line length is much shorter than the wavelength

$$\lambda = \frac{2\pi}{\omega_s \sqrt{L \cdot C}} ,$$

where ω_s is the nominal grid frequency and L, C are the per unit length inductance and capacitance of the line. For typical line parameters, the wavelength is $\lambda \approx 6000$ km, thus the majority of transmission lines fulfill this condition [84].

Defining the line admittance Y_{ij} and the line shunt admittance Y_{ij}^{sh} as

$$\begin{aligned} Y_{ij} &= (R_{ij} + j \cdot X_{ij})^{-1} , \\ Y_{ij}^{sh} &= G_{ij}^{sh} + j \cdot B_{ij}^{sh} , \end{aligned}$$

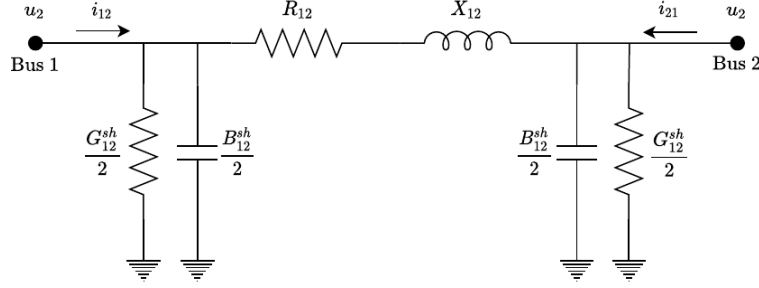


Figure 2.1: Pi-model for transmission lines. The parameters R_{12} and X_{12} are the line resistance and reactance, G_{12}^{sh} and B_{12}^{sh} are the line shunt conductance and susceptance.

the currents injected into the line at the buses can be calculated from the bus voltages as

$$\begin{bmatrix} i_{ij} \\ i_{ji} \end{bmatrix} = \begin{bmatrix} \frac{Y_{ij}^{sh}}{2} + Y_{ij} & -Y_{ij} \\ -Y_{ij} & \frac{Y_{ij}^{sh}}{2} + Y_{ij} \end{bmatrix} \begin{bmatrix} u_i \\ u_j \end{bmatrix}.$$

The power injected into the line at both sides is then given by

$$\begin{aligned} S_{ij} &= u_i \cdot i_{ij}^*, \\ S_{ji} &= u_j \cdot i_{ji}^*. \end{aligned}$$

Typically, in transmission lines, we have $R \ll X$ and therefore it is often assumed that the lines are lossless, i.e. $R \approx 0$. In that case, the lines are purely inductive and no active power is lost. Hence, for lossless lines the active power injections at both sides fulfill the condition $P_{ij} = -P_{ji}$.

For transformers, we have already seen in Section 2.1.2 that in the per-unit system the currents and voltages on both sides are the same. As a result, all transformers can be represented as normal lines and modeled with the π -model.

2.2.2 Load Models

The voltage-dependent load model is defined by an algebraic constraint

$$0 = (P_0 + j \cdot Q_0) \left(\frac{u}{u_0} \right)^\alpha - u \cdot i^*,$$

where u_0 is the nominal bus voltage, u is the actual bus voltage, i is the current withdrawn by the load, P_0, Q_0 are power consumption parameters and α determines the voltage dependency. For $\alpha = 0$ there is no voltage dependence and the power consumption of the load is constant. For $\alpha = 1$ the current withdrawn by the load is constant and $\alpha = 2$ corresponds to a constant impedance model. The latter is mathematically equivalent to the bus shunts

introduced in Section 2.1.4. In the engineering literature, a combination of the three mentioned models is frequently used and known as the *ZIP*-load model.

In reality, loads are not entirely static and may have a frequency dependence [55, 78, 84]. However, in this thesis, I will only consider purely algebraic loads without any frequency dependence.

2.2.3 Synchronous Generator Models

For the dynamics of synchronous machines, there exist a variety of dynamical models that mainly differ in how much detail of the electromagnetic dynamics is covered. In this section, I will introduce a fourth-order model show which simplifying assumptions have to be made to derive the second-order classical model.

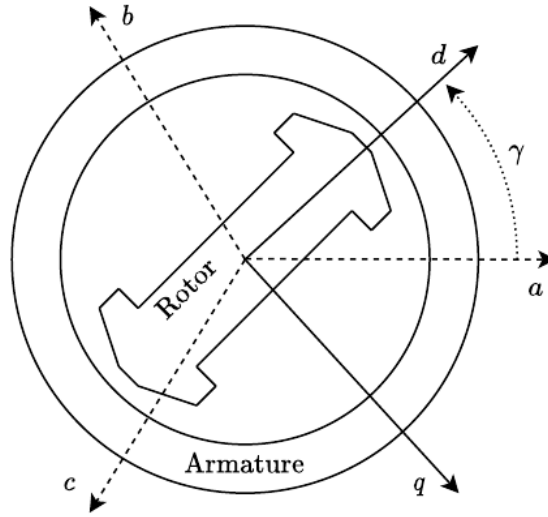


Figure 2.2: Schematic picture of a synchronous generator and its axes.

The position of the rotor d -axis relative to the stator a -axis is given by

$$\gamma = \omega_s t + \delta ,$$

where ω_s is the nominal synchronous frequency. I denote the rotor speed deviation as $\omega := \dot{\gamma} - \omega_s$. The mechanical equation of the rotor speed dynamics in the co-rotating frame is given by the so-called swing equation

$$\begin{aligned} \dot{\delta} &= \omega , \\ M\dot{\omega} &= P_m - P_e - D\omega . \end{aligned} \tag{2.10}$$

Here, P_m is the mechanical turbine power, P_e is the so-called air-gap power [78], D is the damping coefficient and M is the inertia constant.

I denote the complex voltage of grid point to which the synchronous machine is connected as $u_g = v_g e^{j\theta_g}$. Following the convention of most textbooks (e.g. [84, 110]), the transformation between the armature voltage and the bus voltage is given by

$$\begin{aligned} u_{dq} e^{j(\delta - \frac{\pi}{2})} &= v_g e^{j\theta_g} , \\ i_{dq} e^{j(\delta - \frac{\pi}{2})} &= i_g e^{j\phi_g} . \end{aligned}$$

The active and reactive power injected into the grid are

$$\begin{aligned} P_g &= v_d i_d + v_q i_q , \\ Q_g &= v_q i_d - v_d i_q . \end{aligned}$$

The armature voltage is given by the algebraic relation[78]

$$\begin{bmatrix} v_d \\ v_q \end{bmatrix} = \begin{bmatrix} E'_d \\ E'_q \end{bmatrix} - \begin{bmatrix} R_a & X'_q \\ -X'_d & R_a \end{bmatrix} \begin{bmatrix} i_d \\ i_q \end{bmatrix} .$$

Here, R_a is the armature resistance, X'_d, X'_q are the transient reactances and E'_d, E'_q are the transient electromagnetic fluxes (EMFs). The dynamical equations for the EMFs is [78]

$$\begin{aligned} T'_{d0} \dot{E}'_d &= -E'_d - i_q(X_q - X'_q) , \\ T'_{q0} \dot{E}'_q &= E_f - E'_q + i_d(X_d - X'_d) , \end{aligned} \tag{2.11}$$

where E_f is the field voltage [78]. The air gap power is given by

$$P_e = v_d i_d + v_q i_q + R_a(i_d^2 + i_q^2) ,$$

and thus, if the armature resistance is small $R_a \approx 0$, we get $P_g = P_e$.

Fourth-Order Model Combining the differential equations of the swing equation (2.10) and the transient EMFs (2.11) yields the model

$$\begin{aligned} \dot{\delta} &= \omega , \\ M\dot{\omega} &= P_m - P_e - D\omega , \\ T'_{d0} \dot{E}'_d &= -E'_d - i_q(X_q - X'_q) , \\ T'_{q0} \dot{E}'_q &= E_f - E'_q + i_d(X_d - X'_d) . \end{aligned} \tag{2.12}$$

Third-Order Model Assuming the d -axis transient EMF to be constant reduces the model by one order such that

$$\begin{aligned} \dot{\delta} &= \omega , \\ M\dot{\omega} &= P_m - P_e - D\omega , \\ T'_{q0} \dot{E}'_q &= E_f - E'_q + i_d(X_d - X'_d) . \end{aligned}$$

Second-Order Model Neglecting all electromagnetic dynamics yields the so-called classical model which is simply given by the swing equation dynamics (2.10).

2.2.4 Inverter Control Models

To connect DC power sources such as photovoltaic (PV) units or batteries to an AC grid, the DC signal has to be converted to an AC signal using power electronic devices called inverters. In these devices, the generation of a sinusoidal waveform is achieved by a very fast switching using pulse width modulation (PWM) and an additional low pass filter. The magnitude, frequency, and phase shift of the sinusoidal signals can be controlled by certain control schemes. Generally, three classes of control modes for inverters can be distinguished: the grid-feeding, grid-forming, and the grid-supporting control schemes [109, 26]. In this thesis, I will focus on grid-feeding and grid-forming modes. Grid-feeding inverters are controlled such that they inject a specific amount of power into the grid. This is also called current control mode (CCM). On the other hand, grid-forming inverters are operated in voltage control mode (VCM) that controls voltage magnitude and frequency. Additionally to these inner control loops that determine the inverter mode, there is an outer control loop that typically is an order of magnitude slower to decouple the dynamics [26]. Depending on the inverter type, outer control schemes can for example be a maximum power point tracking (MPPT) control or a droop control.

To this day, the vast majority of inverter-interfaced units in the grid are still controlled in grid feeding mode. However, with increasing grid stability problems due to the ongoing reduction in the number of large conventional units this is likely to change in a foreseeable future.

Grid-Feeding Inverter For the CCM it can be assumed that the inner control loop is instantaneous and can thus be viewed as an ideal current source. With the reference values P_r , Q_r for active and reactive power the current is then given by

$$i_{dq} = \frac{P_r - jQ_r}{u_{dq}^*}.$$

The transformation between the synchronous reference system of the grid and the dq -system of the inverter is given by

$$\begin{aligned} (u_d + ju_q) e^{j\delta} &= |u_g| e^{j\theta_g}, \\ (i_d + ji_q) e^{j\delta} &= |i_g| e^{j\phi_g}. \end{aligned}$$

To synchronize the inverter with the grid, the phase angle δ is determined by a so-called phase-locked loop (PLL) control which is depicted in Figure 2.3 and

has the dynamics

$$\begin{aligned}\dot{\delta} &= \omega , \\ \omega &= K_p \cdot u_q + K_i \cdot I_{u_q} , \\ \dot{I}_{u_q} &= u_q .\end{aligned}$$

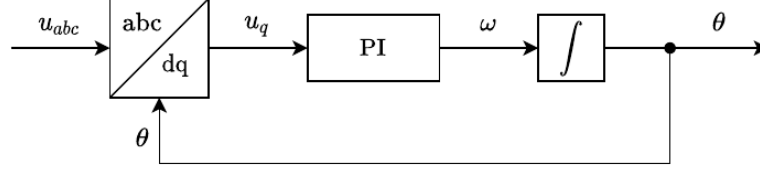


Figure 2.3: Block diagram of a phase-locked loop (PLL).

When the dynamics of the PLL is very fast, the inverter can be assumed to always be in phase with the grid and can be modeled as a simple algebraic constraint that feeds a certain active and reactive power P_r, Q_r into the grid. These powers are controlled by an outer control loop, e.g. by an MPPT such that the maximum available power of the DC energy source (e.g. a PV plant) is fed into the grid.

Grid-Forming Inverter For the VCM it can be assumed that the frequency regulation is instantaneous, but the voltage magnitude control has a delay that is modeled by a PT1-controller [114]

$$\begin{aligned}\dot{\delta} &= \omega , \\ \tau_v \dot{v} &= -v + V .\end{aligned}\tag{2.13}$$

For the outer control loop, it is assumed that a droop control regulates the frequency ω and voltage magnitude V proportionally to the changes of measured active and reactive power P_m and Q_m in the grid

$$\begin{aligned}\omega &= -K_p(P_m - P_d) , \\ V &= V_d - K_q(Q_m - Q_d) .\end{aligned}\tag{2.14}$$

The measured powers are filtered with a low pass filter [114]

$$\begin{aligned}\tau_p \dot{P}_m &= -P_m + P_e , \\ \tau_p \dot{Q}_m &= -Q_m + Q_e .\end{aligned}\tag{2.15}$$

The inner control loop is much faster, i.e. $\tau_v \ll \tau_P$, and therefore $\tau_v \approx 0$. Combining (2.13), (2.14) and (2.15) then yields the third order equation system

$$\begin{aligned}\dot{\delta} &= \omega , \\ \tau_p \dot{\omega} &= -\omega + K_p(P_d - P_e) , \\ \tau_p \dot{v} &= V_d - V + K_q(Q_d - Q_e) .\end{aligned}$$

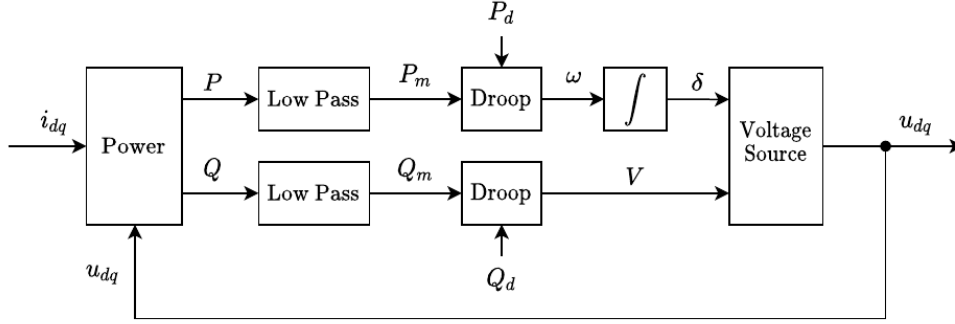


Figure 2.4: Block diagram of the outer control loop of a grid-forming inverter.

Neglecting the voltage dynamics reduces the system to a second-order model

$$\begin{aligned}\dot{\delta} &= \omega, \\ \tau_p \dot{\omega} &= -\omega + K_p(P_d - P_e).\end{aligned}$$

Defining the parameters $M = \frac{\tau_p}{K_p}$ and $D = \frac{1}{K_p}$, we see that this dynamics is equivalent to the swing equation (2.10) [113].

If we further assume that the measured power is not filtered, i.e. $\tau_p = 0$, reduces the system to a first-order model. For a microgrid with several of such droop controlled grid-forming inverters [122] inserting the AC power flow equations (2.9) and for a purely inductive grid $G_{kl} \approx 0$ yields

$$D_k \dot{\delta}_k = P_{d,k} - \sum_l V_l V_k B_{kl} \sin(\delta_{kl}),$$

which is the dynamics of the famous Kuramoto-oscillator model [70, 71].

2.3 Grid Models

Due to security concerns, the data of real power grid infrastructure is usually not publicly available. As a result, most scientific studies rely on synthetic grid data. In the following, I present three different types of synthetic test cases, that are suited to perform different kinds of studies: Benchmark test cases consist of a relatively small number of buses but contain very detailed parametrization. Data-based synthetic grid models come with more realistic size and grid topology but contain less detail on component parameters. Finally, randomly generated synthetic grids are well suited for studying the role of the network topology as well as scaling properties.

2.3.1 Benchmark Test Cases

In the electrical engineering literature, it is very common to use benchmark test cases. These benchmarks are typically defined by engineering associations

such as the Institute of Electrical and Electronics Engineers (IEEE) or the International Council on Large Electric Systems (CIGRE).

Most of the IEEE test cases have been defined decades ago and therefore they typically only cover HV transmission grids with purely conventional generation. However, for researching the energy transition and future power grids, test cases with detailed data on distributed and renewable generation are urgently needed. One rare example of such a test case is the CIGRE MV distribution network that includes distributed energy resources such as PV, wind, batteries, and fuel cells [125].

2.3.2 Data-Based Synthetic Test Cases

The second type of test cases is designed to resemble the structure of a specific existing power grid by using only publicly available data. The most notable examples are the European transmission grid models of the SciGRID¹ project, which are built from OpenStreetMap data [81] and the US transmission grid models provided by the Texas A&M University² generated from U.S. census data [24]. Although the grid topology and parametrization do not exactly match the reality, these test cases can still capture some basic properties and give informative results, especially for static analyses.

One major problem with these test cases is that their purpose is to resemble an existing power grid but often come with no or only very limited information on dynamic parameters such as the inertia or droop control parameter of generators. Since these parameters have a huge impact on the linear and nonlinear dynamics, stability, and eigenmodes of the system, the validity of dynamic simulation results in these grids is quite limited.

2.3.3 Randomly Generated Test Cases

The last type of test cases are randomly generated grid topologies. In complex network science, there exists a multitude of models for generating random networks that resemble certain properties of certain real-world networks. Famous examples are networks with scale-free degree distributions [19] or with the 'small-world' property, i.e. a small average shortest path length [140]. A random growth model that resembles the properties of infrastructure networks in general and power grids, in particular, was introduced in [117]. The model generates spatially embedded networks in a two-stage process: In the initialization phase, a minimum spanning tree for a set of randomly distributed nodes. In the growth phase, single nodes are added and connected to the grid by maximizing a function that gives a trade-off between minimizing the spatial distance and the average shortest path lengths. This model has been shown to generate networks with topological properties similar to existing transmission

¹<https://www.power.scigrid.de/>

²<https://electricgrids.engr.tamu.edu/>

grids, i.e. a low mean degree and a degree distribution with an exponential tail [94]. Random grids are particularly suited for analyzing the impact of the grid topology on the resilience or stability of the system by generating large ensembles of networks with similar properties [101, 91, 89]. The downside of this model is, however, that it only generates realistic network structures but does not give any information on the power production and demand or the dynamical parameters at the nodes. Nevertheless, for analyzing the role of the grid topology, it is sufficient to randomly distribute consumers and producers in the grid and to use homogeneous dynamical parameters.

Chapter 3

A Linear Response Theory for Complex Systems

For complex nonlinear dynamical systems it is usually impossible to perform any detailed analytical calculations for the entire nonlinear model. However, many engineered systems are typically controlled such that the system stays close to a desired operating state. Assuming that the overall system control performs well enough to keep the system sufficiently close to the operating state, the system dynamics can be linearized around this state. For the linearized system, the performance of the system control can then be analyzed with the help of the well-established theory of linear multiple-input-multiple-output (MIMO) systems.

A very similar approach is taken in the field of statistical physics, where nonlinear physical systems are linearized around a stable equilibrium state to analyze the system's response to external (often stochastic) perturbations. Here, special emphasis is placed on the analysis of potential resonances of the system eigenmodes to the perturbation. In fact, the approaches of linear response theory and the theory of linear MIMO systems are mathematically equivalent, albeit complementary in some of their assumptions and in their typical applications.

For complex systems that have a large number of components and various interactions with their environment, the space of potential faults and disturbances is potentially very large and high dimensional. In control theory, a typical approach is therefore to perform a rather general and abstract theoretical analysis of the system without making any further assumptions on the detailed nature of the perturbations and instead focus on a worst-case analysis. Contrary to this, the approach in statistical physics is to reduce the complexity of the system's interaction with its environment by developing stochastic models that capture the main features of typical system perturbations.

In this chapter, I develop a linear response theory for complex dynamical systems on network structures. This theory will be used in the subsequent

chapter to analyze the impact of renewable fluctuations on the grid frequency. Some of the results presented in this chapter have been published in [99].

3.1 Linear Time-Invariant Systems

First of all, I derive the linear response of a complex dynamical system to a multi-dimensional perturbation. Subsequently, I introduce the concepts of signal and system norms that can be used to quantify the response of the system.

3.1.1 Linear Response Theory

Consider a nonlinear dynamical system of the form

$$\dot{\mathbf{x}}(t) = \mathbf{f}(\mathbf{x}(t), \mathbf{u}(t)) , \quad (3.1)$$

where $\mathbf{x}(t) : \mathbb{R} \rightarrow \mathbb{R}^N$ is the system state, and $\mathbf{u}(t) : \mathbb{R} \rightarrow \mathbb{R}^M$ is a perturbation signal. In many physical systems, we additionally have an observable or output $\mathbf{y}(t) : \mathbb{R} \rightarrow \mathbb{R}^L$

$$\mathbf{y}(t) = \mathbf{g}(\mathbf{x}(t)) ,$$

that is used to measure the state of the dynamical system.

Assumption 3.1. *The unperturbed system has a linearly stable equilibrium state \mathbf{x}° such that $\mathbf{0} = \mathbf{f}(\mathbf{x}^\circ, \mathbf{0})$, and the eigenvalues of the Jacobian $\frac{\partial \mathbf{f}}{\partial \mathbf{x}}(\mathbf{x}^\circ, \mathbf{0})$ have negative real parts.*

Without loss of generality, we can choose a coordinate system relative to this equilibrium such that $\mathbf{x}^\circ = \mathbf{0}$ and $\mathbf{y}^\circ = \mathbf{0}$. When the system (3.1) is perturbed by a sufficiently small signal \mathbf{u} the state \mathbf{x} and the observable \mathbf{y} will show a dynamic response to the perturbation but stay in the vicinity of the stable equilibrium. Defining the matrices $\mathbf{A} \in \mathbb{R}^{N \times N}$, $\mathbf{B} \in \mathbb{R}^{N \times M}$ and $\mathbf{C} \in \mathbb{R}^{L \times N}$ as

$$\mathbf{A} := \frac{\partial \mathbf{f}}{\partial \mathbf{x}}(\mathbf{0}, \mathbf{0}) , \quad \mathbf{B} := \frac{\partial \mathbf{f}}{\partial \mathbf{u}}(\mathbf{0}, \mathbf{0}) , \quad \mathbf{C} := \frac{\partial \mathbf{g}}{\partial \mathbf{x}}(\mathbf{0}) ,$$

we can conduct a Taylor expansion of the functions \mathbf{f} and \mathbf{g} up to linear order and get the linearized dynamics around the equilibrium state

$$\begin{aligned} \dot{\mathbf{x}} &= \mathbf{A}\mathbf{x} + \mathbf{B}\mathbf{u} , \\ \mathbf{y} &= \mathbf{C}\mathbf{x} . \end{aligned} \quad (3.2)$$

In control theory, such a system is called a linear time-invariant (LTI) multiple-input-multiple-output (MIMO) system with input \mathbf{u} , state \mathbf{x} and output \mathbf{y} .

Definition 3.1 (Response Function). *The response function of (3.2) is defined as*

$$\mathbf{H}(t) = \Theta(t) \mathbf{C} e^{\mathbf{A}t} \mathbf{B} , \quad (3.3)$$

where $e^{\mathbf{A}t}$ is a matrix exponential and $\Theta(t)$ is the Heaviside function.

Using this definition and integrating (3.2) yields the linear response of \mathbf{y} to a perturbation \mathbf{u}

$$\mathbf{y}(t) = \int_{-\infty}^{\infty} \mathbf{H}(t - t') \mathbf{u}(t') dt' . \quad (3.4)$$

Definition 3.2 (Transfer Function). *The transfer function of (3.2) is defined as*

$$\mathbf{G}(s) = \mathbf{C}(s\mathbf{I} - \mathbf{A})^{-1} \mathbf{B} . \quad (3.5)$$

It can easily be shown, that $\mathbf{G}(s)$ is the Laplace Transform and $\mathbf{G}(j\nu)$ is the Fourier Transform of the response function (3.3). Applying the convolution theorem to the response equation (3.4) yields the linear response in Fourier space

$$\hat{\mathbf{y}}(\nu) = \mathbf{G}(j\nu) \hat{\mathbf{u}}(\nu) .$$

3.1.2 Signal and System Norms

In this section I will introduce the concepts of signal and system norms, that will later be used to quantify the linear response of dynamical systems. I will particularly focus on quadratic norms since these are often easy to evaluate analytically and therefore also the most commonly used norms in the control theory literature. For a vector-valued signal $\mathbf{y}(t)$ the L_2 norm is defined as

$$\|\mathbf{y}\|_2 := \sqrt{\int_0^{\infty} \mathbf{y}^T(t) \mathbf{y}(t) dt} . \quad (3.6)$$

Similarly, the L_2 norm can also be defined in Fourier space as

$$\|\hat{\mathbf{y}}\|_2 := \sqrt{\frac{1}{2\pi} \int_{-\infty}^{\infty} \hat{\mathbf{y}}^\dagger(\nu) \hat{\mathbf{y}}(\nu) d\nu} . \quad (3.7)$$

From Plancherel's theorem it follows, that (3.6) and (3.7) are in fact equal, i.e. $\|\mathbf{y}\|_2 = \|\hat{\mathbf{y}}\|_2$. Signal norms can be used to quantify the output signal of a MIMO system for a particular input signal. In contrast to this, system norms are defined as norms of the response or transfer function and hence give more general information on the systems response properties. The H_2 system norm is defined as

$$\|\mathbf{H}\|_2 := \sqrt{\sum_{ij} \|\mathbf{H}_{ij}\|_2^2} = \sqrt{\int_0^{\infty} \text{tr}[\mathbf{H}^T(t) \mathbf{H}(t) dt]} . \quad (3.8)$$

Inserting the definition of the response function (3.3) yields

$$\|H\|_2 = \text{tr} \left[\mathbf{C} \int_0^\infty e^{\mathbf{A}t} \mathbf{B} \mathbf{B}^T e^{\mathbf{A}^T t} dt \mathbf{C}^T \right] .$$

By defining the matrix $\mathbf{X} = \int_0^\infty e^{\mathbf{A}t} \mathbf{B} \mathbf{B}^T e^{\mathbf{A}^T t} dt$, the H_2 system norm can be written as

$$\|H\|_2 = \text{tr} [\mathbf{C} \mathbf{X} \mathbf{C}^T] .$$

Using integration by parts, it can be shown that \mathbf{X} is the solution to the linear matrix equation

$$\mathbf{A} \mathbf{X} + \mathbf{X} \mathbf{A}^T + \mathbf{B} \mathbf{B}^T = 0 , \quad (3.9)$$

which is known as the Lyapunov equation [146]. Hence, calculating the H_2 norm (3.8) of a linear time-invariant system (3.2) can be achieved by simply solving the linear algebraic equation (3.9). As for the signal norms, the system norms in time and in frequency domain are equal, $\|\mathbf{H}\|_2 = \|\mathbf{G}\|_2$, where

$$\|\mathbf{G}\|_2 := \sqrt{\frac{1}{2\pi} \int_{-\infty}^\infty \text{tr}[\mathbf{G}^\dagger(j\nu) \mathbf{G}(j\nu) d\nu]} .$$

This equation illustrates that the H_2 norm can be interpreted as the average system gain over all frequencies.

Besides the H_2 norm, the other important system norm that is frequently used in control theory literature is the H_∞ norm

$$\|\mathbf{G}\|_\infty := \sup_\nu \|\mathbf{G}(j\nu)\|_2 .$$

This norm can be expressed in terms of the maximum singular value $\bar{\sigma}$ [146]

$$\|\mathbf{G}\|_\infty := \sup_\nu \bar{\sigma}(\mathbf{G}(j\nu)) . \quad (3.10)$$

The singular value decomposition of \mathbf{G} is given by $\mathbf{G} = \mathbf{V} \mathbf{\Sigma} \mathbf{U}^\dagger$, with $\mathbf{U} \in \mathbb{C}^{L \times L}$, $\mathbf{V} \in \mathbb{C}^{M \times M}$ and $\mathbf{\Sigma} \in \mathbb{R}^{L \times M}$. The diagonal entries of $\mathbf{\Sigma}$ are the singular values

$$\sigma_i = \sqrt{\lambda_i(\mathbf{G}^\dagger \mathbf{G})} ,$$

where λ_i are the eigenvalues of $\mathbf{G}^\dagger \mathbf{G}$. The singular values correspond to the gain in a certain input and output direction. Consequently, the maximum singular value defines an upper bound for the L_2 norm ratio of input and output

$$\frac{\|\mathbf{G}(j\nu) \hat{\mathbf{u}}(j\nu)\|}{\|\hat{\mathbf{u}}(j\nu)\|} \leq \bar{\sigma}(\mathbf{G}(j\nu)) .$$

Hence, the H_∞ norm is induced by the L_2 norm and can be interpreted as the worst system gain. However, it should be emphasized that the singular value decomposition of $\mathbf{G}(j\nu)$ depends on the frequency ν and it is, therefore, a highly non-trivial task to analytically evaluate the supremum in (3.10) for a given system.

3.2 Stochastic Inputs

In the previous section, I discussed two different edge cases concerning the inputs of a system. On the one hand, for an exactly known input signal, it is directly possible to calculate the system output and quantify it in terms of a signal norm. On the other hand, if there is no given knowledge about the possible inputs, the system norms can be used to determine either the worst case or the average frequency gain of the system.

Now let us assume that the exact input signal is not known, yet there exists some knowledge about its physical nature and statistical properties. This is typically the case, when the interaction of the system with its environment is very complex, but still follows certain basic physical laws. In that case, it is often possible to develop a stochastic model for the interaction of the system with its environment. In this section I will show that if the correlation or the spectral density of the input is known, it is in fact possible to calculate L_2 norm of the expected system output.

3.2.1 Random Perturbations

Assume that the input function of an LTI system (3.2) is parametrized by a random variable. Mathematically, such a random variable X is a measurable function $X : \Omega \rightarrow E$ from the set of possible outcomes Ω called the sample space to a measurable space E called the state space [120]. In simplified terms, this can be interpreted as an ensemble of random input signals. For such an ensemble, the signal norm of a system can be defined as the expectation value of the L_2 signal norm

$$\|\mathbf{y}\|_2^2 := \mathbb{E} \left\{ \int_0^\infty \mathbf{y}^T(t) \mathbf{y}(t) dt \right\} . \quad (3.11)$$

In the following, we will consider the specific case that the input is a random perturbation of the form

$$\mathbf{u}(t) = \mathbf{u}_0 \cdot \delta(t - t_0) , \quad t_0 \geq 0 , \quad (3.12)$$

where δ is the Dirac delta function and \mathbf{u}_0 is a random vector, i.e. a vector whose components are scalar random variables. The output response to such a perturbation is given by

$$\begin{aligned} \mathbf{y}(t) &= \int_0^\infty \mathbf{H}(t - t') \cdot \mathbf{u}(t') dt \\ &= \int_0^\infty \mathbf{H}(t - t') \cdot \mathbf{u}_0 \delta(t' - t_0) dt \\ &= \mathbf{H}(t - t_0) \cdot \mathbf{u}_0 \\ &= \Theta(t - t_0) \mathbf{C} e^{\mathbf{A}(t - t_0)} \mathbf{B} \cdot \mathbf{u}_0 . \end{aligned}$$

Thus, the random perturbation (3.12) can be interpreted as setting the state $\mathbf{x}(t)$ of the system to a random initial condition $\mathbf{x}(t_0) = \mathbf{B} \cdot \mathbf{u}_0$.

Proposition 3.1 (Signal Norm for Random Perturbations). *The signal norm (3.11) of an LTI system (3.2) with a random input (3.12) is given by*

$$\|y\|_2^2 = \int_0^\infty \text{tr}(\mathbf{H}(t) \mathbb{E}\{\mathbf{u}_0 \mathbf{u}_0^T\} \mathbf{H}^T(t)) dt. \quad (3.13)$$

Proof.

$$\begin{aligned} \|y\|_2^2 &= \mathbb{E} \left\{ \int_0^\infty \mathbf{y}^T(t) \mathbf{y}(t) dt \right\} \\ &= \mathbb{E} \left\{ \int_0^\infty \mathbf{u}_0^T \mathbf{H}^T(t - t_0) \mathbf{H}(t - t_0) \mathbf{u}_0 dt \right\} \\ &= \mathbb{E} \left\{ \int_0^\infty \mathbf{u}_0^T \mathbf{H}^T(t) \mathbf{H}(t) \mathbf{u}_0 dt \right\} \\ &= \mathbb{E} \left\{ \int_0^\infty \text{tr}(\mathbf{H}(t) \mathbf{u}_0 \mathbf{u}_0^T \mathbf{H}^T(t)) dt \right\} \\ &= \int_0^\infty \text{tr}(\mathbf{H}(t) \mathbb{E}\{\mathbf{u}_0 \mathbf{u}_0^T\} \mathbf{H}^T(t)) dt. \end{aligned}$$

□

Example 3.1 (Gaussian Random Initial Conditions). *Assume that each entry of \mathbf{u}_0 is a Gaussian random variable with mean zero and variance σ^2 . Further, the variables are uncorrelated, i.e. the covariance between different values is zero. Then we have $\mathbb{E}\{\mathbf{u}_0 \mathbf{u}_0^T\} = \sigma^2 \mathbf{I}$ and therefore the signal norm is given by*

$$\|y\|_2 = \sigma \|\mathbf{G}\|_2.$$

Example 3.2 (Random Variable Perturbation). *Assume k is a random variable with sample space $\Omega = \{1, \dots, m\}$ and the elements of the vector \mathbf{u}_0 are defined such that*

$$u_{0,i} = \begin{cases} 1 & \text{if } i = k, \\ 0 & \text{else.} \end{cases}$$

Then we have $\mathbb{E}\{\mathbf{u}_0 \mathbf{u}_0^T\} = \frac{1}{m} \mathbf{I}$ and therefore the signal norm is given by

$$\|y\|_2 = \frac{1}{m} \|\mathbf{G}\|_2.$$

3.2.2 Stochastic Processes

In this section we analyze the case that the input of the LTI system (3.2) is a stochastic process. In the mathematical definition, stochastic processes are indexed collections of random variables

$$\{x(t) : t \in \mathbb{R}\}.$$

In our case, the index t corresponds to the time and we can therefore loosely interpret this as a time-dependent random variable [47]. We define the signal norm for the output as

$$\|\mathbf{y}\|_2 := \sqrt{\lim_{T \rightarrow \infty} \frac{1}{T} \int_0^T \mathbf{y}^T(t) \mathbf{y}(t) dt} . \quad (3.14)$$

In the following, I will use the following notation:

$$\mathbf{x}_T(t) = \begin{cases} \mathbf{x}(t) & \text{for } 0 < t < T , \\ \mathbf{0} & \text{otherwise.} \end{cases}$$

Definition 3.3 (Cross-Correlation Matrix). *Given a vector of stochastic process $\mathbf{x}(t)$, the cross-correlation matrix is given by*

$$\mathbf{C}_{xx}(t) = \lim_{T \rightarrow \infty} \frac{1}{T} \int_0^T \mathbf{x}_T(t') \mathbf{x}_T^T(t' + t) dt . \quad (3.15)$$

The diagonal elements of this matrix are auto-correlation functions of the scalar stochastic processes $x_i(t)$. The off-diagonal terms are the cross-correlation functions.

Definition 3.4 (Spectral Density Matrix). *Given a vector of stochastic processes $\mathbf{x}(t)$, the power spectral density matrix is given by*

$$\mathbf{S}_{xx}(\nu) = \lim_{T \rightarrow \infty} \frac{1}{T} \hat{\mathbf{x}}_T(\nu) \hat{\mathbf{x}}_T^\dagger(\nu) . \quad (3.16)$$

The diagonal elements of this matrix are the power spectral densities of the scalar stochastic processes $x_i(t)$ and the off-diagonal terms are the cross-spectral densities.

From the cross-correlation theorem it follows that the cross-spectral densities are the Fourier transforms of the cross-correlation functions. A special case is the Wiener-Khinchin theorem which states that the auto-correlation function is the Fourier transform of the power spectral density [47].

Proposition 3.2 (Signal Norm for Stochastic Processes). *The L_2 norm (3.14) of a linear system (3.2) with a stochastic process as the input is given by*

$$\|\mathbf{y}\|_2 = \sqrt{\frac{1}{2\pi} \int_{-\infty}^{\infty} \text{tr}(\mathbf{G}(j\nu) \mathbf{S}_{uu}(\nu) \mathbf{G}^\dagger(j\nu)) d\nu} . \quad (3.17)$$

Proof. The system output to an input \mathbf{u}_T is given by

$$\mathbf{y}(t) = \int_{-\infty}^{\infty} \mathbf{H}(t - t') \mathbf{u}_T(t') dt' .$$

For $t > T$ we have $\mathbf{u}_T(t) = 0$ and therefore $\mathbf{y}(t) = \mathbf{H}(t-T)\mathbf{u}(T)$. If the system is linearly stable, i.e. all Jacobian eigenvalues have negative real parts, the output is exponentially declining. The L_2 norm for $t > T$ is therefore finite and hence

$$\lim_{T \rightarrow \infty} \frac{1}{T} \int_T^\infty \mathbf{y}^T(t) \mathbf{y}(t) dt = 0 .$$

Using this, we can calculate the L_2 norm (3.14) as

$$\begin{aligned} \|\mathbf{y}\|_2^2 &= \lim_{T \rightarrow \infty} \frac{1}{T} \int_0^T \mathbf{y}^T(t) \mathbf{y}(t) dt \\ &= \lim_{T \rightarrow \infty} \frac{1}{T} \int_0^\infty \mathbf{y}^T(t) \mathbf{y}(t) dt \\ &= \lim_{T \rightarrow \infty} \frac{1}{2\pi T} \int_{-\infty}^\infty \hat{\mathbf{y}}^\dagger(\nu) \hat{\mathbf{y}}(\nu) d\nu \\ &= \lim_{T \rightarrow \infty} \frac{1}{2\pi T} \int_{-\infty}^\infty \mathbf{u}_T^\dagger(\nu) \mathbf{G}^\dagger(j\nu) \mathbf{G}(j\nu) \mathbf{u}_T(\nu) d\nu \\ &= \lim_{T \rightarrow \infty} \frac{1}{2\pi T} \int_{-\infty}^\infty \text{tr} \left(\mathbf{G}(j\nu) \mathbf{u}_T(\nu) \mathbf{u}_T^\dagger(\nu) \mathbf{G}^\dagger(j\nu) \right) d\nu \\ &= \frac{1}{2\pi} \int_{-\infty}^\infty \text{tr} \left(\mathbf{G}(j\nu) \mathbf{S}_{\mathbf{u}\mathbf{u}}(\nu) \mathbf{G}^\dagger(j\nu) \right) d\nu . \end{aligned}$$

□

Example 3.3 (White Gaussian Noise). Assume that each entry of the input \mathbf{u} is a Gaussian white noise process with variance σ^2 . The cross-correlation matrix is then given by $\mathbf{C}_{\mathbf{u}\mathbf{u}}(t) = \sigma^2 \delta(t) \mathbf{I}$. Applying the Wiener-Khinchin-Theorem gives the power spectral density matrix $\mathbf{S}_{\mathbf{u}\mathbf{u}}(\nu) = \sigma^2 \mathbf{I}$. Then, the signal norm is given by

$$\|\mathbf{y}\|_2 = \sigma \|\mathbf{G}\|_2 .$$

Again, this example clearly illustrates that the H_2 norm corresponds to the signal norm in case of an equal excitation off all frequencies. For auto-correlated stochastic processes, the power spectral density is not flat and consequently, some frequencies will be stronger excited than others. Hence, $\mathbf{S}_{\mathbf{u}\mathbf{u}}(\nu)$ is not a constant and solving (3.17) will become difficult and in most cases analytically impossible. Nevertheless, spectral analysis can be very useful to understand how a system responds to a certain stochastic input. In the next section, I will introduce the decomposition of the dynamical system into its eigenmodes and show that the overlap of the eigenfrequencies with the power spectral densities of the input determines how strong certain modes will be excited.

3.3 Eigenmode Analysis

In Section 3.1.2 it was shown that the transfer function of a linear MIMO system can be decomposed with a singular value decomposition and that the

maximum singular value defines an upper bound for the system output. In this section, I will introduce an alternative decomposition of the transfer function into the eigenmodes of the system Jacobian. An advantage of this approach is that this decomposition does not depend on the frequency and therefore it is possible to separate the spatial and frequency dependency of each mode. With additional knowledge about the spectral properties of the system input, this approach also allows us to derive additional bounds and estimates for the system output.

3.3.1 Eigenmode Decomposition of the Transfer Function

Proposition 3.3. *The expansion of the transfer function $G(s)$ into the eigenmodes of the system Jacobian A is given by*

$$G(s) = \sum_{n=1}^N G^{(n)}(s) = \sum_{n=1}^N \frac{C \mathbf{v}_r^{(n)} \mathbf{v}_l^{(n)} B}{s - \lambda_n},$$

where λ_n are the eigenvalues of the matrix A and $\mathbf{v}_r^{(n)} \mathbf{v}_l^{(n)}$ is the outer product of the corresponding right and left eigenvectors.

Proof. The matrix A can be factorized as

$$A = Q \Lambda Q^{-1},$$

where Q and Q^{-1} are given by the left and right eigenvectors

$$Q = \begin{bmatrix} \mathbf{v}_r^{(1)} & \dots & \mathbf{v}_r^{(n)} \end{bmatrix}, \quad Q^{-1} = \begin{bmatrix} \mathbf{v}_l^{(1)} \\ \vdots \\ \mathbf{v}_l^{(n)} \end{bmatrix},$$

and Λ is a diagonal matrix whose diagonal elements are the eigenvalues $\Lambda_{nn} = \lambda_n$. Using this, we can show that

$$\begin{aligned} (j\nu I - A)^{-1} &= Q Q^{-1} (j\nu I - A)^{-1} Q Q^{-1} \\ &= Q (j\nu I - Q^{-1} A Q)^{-1} Q^{-1} \\ &= Q (j\nu I - \Lambda)^{-1} Q^{-1}. \end{aligned}$$

An element of this matrix is given by

$$[Q (j\nu I - \Lambda)^{-1} Q^{-1}]_{ij} = \sum_{n=1}^N \frac{Q_{in} Q_{nj}^{-1}}{j\nu - \lambda_n} = \sum_{n=1}^N \frac{\mathbf{v}_{r,i}^{(n)} \mathbf{v}_{l,j}^{(n)}}{j\nu - \lambda_n},$$

and therefore

$$(j\nu I - A)^{-1} = \sum_{n=1}^N \frac{\mathbf{v}_r^{(n)} \mathbf{v}_l^{(n)}}{j\nu - \lambda_n}.$$

□

Corollary 3.3.1. *For the response function the eigenmode expansion yields*

$$\mathbf{H}(t) = \sum_{n=1}^N \Theta(t) e^{\lambda_n t} \mathbf{C} \mathbf{v}_r^{(n)} \mathbf{v}_l^{(n)} \mathbf{B}.$$

The imaginary part of the eigenvalues corresponds to the frequency of the eigenmodes, whereas the real part corresponds to the damping.

Example 3.4 (Symmetric System with Homogeneous Inputs & Outputs). *For a symmetric dynamical system $\mathbf{A} = \mathbf{A}^T$, the eigenvalues are real $\lambda_n \in \mathbb{R}$ and the eigenvectors are orthonormal $\mathbf{v}_l^{(n)} \cdot \mathbf{v}_r^{(m)} = \delta_{nm}$. For homogeneous inputs and outputs $\mathbf{B} = \mathbf{I}$, $\mathbf{C} = \mathbf{I}$ we then have*

$$\begin{aligned} \|\mathbf{G}\|_2^2 &= \int_{-\infty}^{\infty} \text{tr} \left(\mathbf{G}(i\nu) \mathbf{G}^\dagger(i\nu) \right) d\nu = \sum_{n,m} \int_{-\infty}^{\infty} \text{tr} \left(\frac{\mathbf{v}_r^{(n)} \mathbf{v}_l^{(n)}}{\lambda_n - j\nu} \cdot \frac{\mathbf{v}_r^{(m)} \mathbf{v}_l^{(m)}}{\lambda_m + j\nu} \right) d\nu \\ &= \sum_n \text{tr} \left(\int_{-\infty}^{\infty} \frac{\mathbf{v}_r^{(n)} \mathbf{v}_l^{(n)}}{\lambda_n^2 + \nu^2} d\nu \right) = \sum_n \text{tr} \left(\frac{\mathbf{v}_r^{(n)} \mathbf{v}_l^{(n)}}{\lambda_n} \right) = \sum_n \frac{1}{\lambda_n}. \end{aligned}$$

We see that in this example, all cross-mode terms vanish. In general, this is not the case. The evaluation of all single terms can therefore be quite cumbersome. However, in the following, I will show that the mode expansion is still useful for deriving bounds or approximations for the signal norm of the output.

3.3.2 Single Mode Response Analysis

With the eigenmode decomposition of the transfer function, we can define the output of a specific mode as

$$\hat{\mathbf{y}}^{(n)}(\nu) = \mathbf{G}^{(n)}(j\nu) \hat{\mathbf{u}}(\nu) = \mathbf{V}^{(n)} \frac{\hat{\mathbf{u}}(\nu)}{j\nu - \lambda_n}, \quad (3.18)$$

where I introduced the matrix $\mathbf{V}^{(n)} = \mathbf{C} \mathbf{v}_r^{(n)} \mathbf{v}_l^{(n)} \mathbf{B}$.

Definition 3.5 (Spectral Excitation Matrix). *The spectral excitation matrix of a mode n is given by the integral*

$$\mathbf{S}^{(n)} = \frac{1}{2\gamma_n} \int_{-\infty}^{\infty} k^{(n)}(\nu) \mathbf{S}_{\mathbf{u}\mathbf{u}}(\nu) d\nu, \quad (3.19)$$

where $\mathbf{S}_{\mathbf{u}\mathbf{u}}(\nu)$ is the spectral density matrix of the input \mathbf{u} and

$$k^{(n)}(\nu) = \frac{1}{\pi} \frac{\gamma_n}{\gamma_n^2 + (\nu - \nu_n)^2} \quad (3.20)$$

is a normalized Lorentz function with its peak at the mode eigenfrequency $\nu_n = \Im(\mu_n)$ and the width equal to the mode damping $\gamma_n = |\Re(\mu_n)|$.

Using this definition, we can write L_2 norm (3.17) of the single mode output (3.18) as

$$\|\mathbf{y}^{(n)}\|_2 = \sqrt{\text{tr}(\mathbf{V}^{(n)} \mathbf{S}^{(n)} \mathbf{V}^{(n)\dagger})} . \quad (3.21)$$

The spectral excitation matrix defines how strongly a certain mode is excited by an input with spectral density \mathbf{S}_{uu} . The Lorentz function $k^{(n)}(\nu)$ is maximal at the eigenfrequency ν_n of the mode. Hence, the entries of the spectral excitation matrix will be large when the spectral densities are strong at that specific frequency.

In general, the integral (3.19) is hard to compute. For specific functions $\mathbf{S}_{uu}(\nu)$ it can be solved with the help of the residue theorem. However, in many applications the spectral density might not be known analytically. In that case, we could determine the power spectral density from measurements and compute the L_2 -norm semi-analytically. Another possibility is to approximate the integral by assuming that the spectral density is "locally flat", i.e. it does not increase significantly over the spectral width of the single eigenmodes. Taking the limit of a spectral width going towards zero, we can approximate the Lorentz functions as delta functions

$$\lim_{\gamma_n \rightarrow 0} k^{(n)}(\nu) = \delta(\nu - \nu_n) .$$

Inserting this into (3.19) yields the "peak approximation" of the spectral excitation matrix

$$\mathbf{S}^{(n)} \approx \frac{1}{2\gamma_n} \mathbf{S}_{uu}(\nu_n) . \quad (3.22)$$

Example 3.5 (Single input single output system). *Assume a scalar input $u(t)$ with power spectral density S_{uu} that enters the system at the dynamics of variable $x_k(t)$ and the output is given by the single variable $y(t) = x_j(t)$. Then, (3.21) reduces to*

$$\|y^{(n)}\|_2 = |v_{r,j}^{(n)}| |v_{l,k}^{(n)}| \sqrt{S^{(n)}} .$$

Inserting the peak approximation yields

$$\|y^{(n)}\|_2 \approx |v_{r,j}^{(n)}| |v_{l,k}^{(n)}| \sqrt{\frac{S_{uu}(\nu_n)}{2\gamma_n}} .$$

3.4 Systems on Network Structures

Many complex dynamical systems are characterized by an underlying network structure. Mathematically, such networks can be represented by a graph $\mathcal{G} = (\mathcal{V}, \mathcal{E})$, with a set of vertices \mathcal{V} corresponding to the dynamical subsystems and a set of edges \mathcal{E} corresponding to the coupling of these systems. As shown

in Section 2.1.4, the topological structure of such a graph can be represented by an oriented incidence matrix $\mathbf{C} \in \mathbb{R}^{|\mathcal{V}| \times |\mathcal{E}|}$ that is defined as

$$C_{ij} := \begin{cases} +1 & \text{if } j \text{ is an outgoing edge from node } i \\ -1 & \text{if } j \text{ is an incoming edge to node } i \\ 0 & \text{else .} \end{cases}$$

Here, the terms *incoming* and *outgoing* denote the orientation of each edge. The choice of these orientations is arbitrary and corresponds to a reference frame which will become important for indicating flow directions on the edges.

3.4.1 Network Laplacians

Another matrix, that is particularly important for describing the dynamics of diffusively coupled networks, is the Laplacian matrix which is defined as

$$\mathbf{L} := \mathbf{C}\mathbf{C}^T .$$

By definition the Laplacian is a symmetric matrix and therefore all its eigenvalues $\lambda_i \in \mathbb{R}$. Moreover, it can easily be proven that the Laplacian is a positive semidefinite matrix and therefore all eigenvalues $\lambda_i \geq 0$. In fact, there is always one eigenvalue $\lambda_1 = 0$. This directly follows from the fact that the sum of every row and column is zero and therefore the vector $\mathbf{v}_1 = (1, \dots, 1)^T$ always satisfies $\mathbf{L}\mathbf{v}_1 = 0$. It can further be shown, that if the network is connected (i.e. there exists a path connecting every pair of nodes), λ_1 is the only zero eigenvalue. For connected networks we then have

$$0 = \lambda_1 < \lambda_2 \leq \dots \leq \lambda_{|\mathcal{V}|} .$$

The second smallest eigenvalue is called the Fiedler eigenvalue or algebraic connectivity and is a measure of how well connected the network is.

In many real-world applications the edges of the graph have weights, that represent the flow capacities of the edges in a flow network. Denoting $\mathbf{w} \in \mathbb{R}_{>0}^{|\mathcal{E}|}$ as the vector of edge weights, we can define a weighted Laplacian matrix as

$$\mathbf{L} = \mathbf{C} \cdot \text{diag}(\mathbf{w}) \cdot \mathbf{C}^T .$$

All properties of ordinary Laplacians that have been discussed above, also hold for weighted Laplacians.

3.4.2 Dynamics with Diffusive Coupling

Consider a complex dynamical system that consists of a large number of subsystems. The dynamics of a subsystem i depends on its internal state variables \mathbf{x}^i and an interaction $p^i(\mathbf{x})$ with the rest of the system

$$\dot{\mathbf{x}}^i = \mathbf{f}^i(\mathbf{x}^i, p^i(\mathbf{x})) . \quad (3.23)$$

In many practical applications, the interaction $p^i(\mathbf{x})$ has the following two properties:

1. The interaction of the subsystem with the rest of the system can be decomposed into a sum of scalar bilateral couplings.
2. The bilateral coupling depends only on the state difference of a single internal variable.

The first property allows us to represent the system structure as a network. The second property describes a system with diffusive coupling. The interaction of subsystem i with the other subsystems can then be written as

$$p^i(\mathbf{x}) = \sum_{j \in \mathcal{N}_i} p^{ij}(x_q^i - x_q^j). \quad (3.24)$$

Here, x_q^i is the q th state variable at the i th node and $\mathcal{N}(i)$ is the set of its neighbors. The scalar coupling functions p^{ij} can be interpreted as a physical flow between i and j .

Assumption 3.2 (Homogeneous Node Dynamics). *All dynamical subsystems have the same dynamics*

$$\mathbf{f}^i = \mathbf{f}^j \quad \text{for all } i, j.$$

This is a strong assumption and often not true for realistic systems. However, only with this assumption we are able to analytically disentangle the local dynamics of each subsystem and impact of the network structure on the global dynamics. Investigating the properties of such homogenous systems will also help us to interpret the numerical results of more realistic heterogeneous network systems.

Proposition 3.4 (Diffusive Network Jacobian). *Given Assumption 3.2, the Jacobian of the networked system with node dynamics (3.23) and coupling (3.24) can be written in the form*

$$\mathbf{A} = \mathbf{M}_1 \otimes \mathbf{I} + \mathbf{M}_L \otimes \mathbf{L}, \quad (3.25)$$

where $\mathbf{L} \in \mathbb{R}^{|\mathcal{V}| \times |\mathcal{V}|}$ is the weighted Laplacian with weights $w_{ij} = \frac{\partial p^{ij}}{\partial x_q^i}$ (q is the index of the coupling variable) and \otimes denotes the Kronecker product. The eigenvalues μ of \mathbf{A} are given by the eigenvalues of the matrix

$$\mathbf{M}_\lambda = \mathbf{M}_1 + \lambda_n \mathbf{M}_L,$$

where λ_n are the eigenvalues of \mathbf{L} . The Jacobian eigenvectors \mathbf{v} are given by the Kronecker product of the Laplacian eigenvectors \mathbf{v} and the eigenvectors of \mathbf{M}_L .

Proof. Taking the total derivative of the k th component of the right-hand-side function at the i th node with respect to the l th variable at the j th node yields

$$\frac{df_k^i}{dx_l^j} = \frac{\partial f_k^i}{x_l^i} \delta_{ij} + \frac{\partial f_k^i}{\partial p^i} \delta_{lq} \left(\delta_{ij} \sum_n \frac{\partial p^{in}}{\partial x_q^i} - \frac{\partial p^{ij}}{\partial x_q^i} \right) .$$

Define the matrices

$$[\mathbf{M}_1]_{kl} = \frac{\partial f_k}{x_l} , \quad [\mathbf{M}_L]_{kl} = \frac{\partial f_k}{\partial p} \delta_{lq} ,$$

and using the fact that the Laplacian can be written as

$$L_{ij} = \delta_{ij} \sum_n w_{in} - w_{ij} ,$$

yields (3.25). For a right eigenvector of the Jacobian we have:

$$\begin{aligned} \mathbf{A} \mathbf{v}^{n,m} &= (\mathbf{M}_1 \otimes I + \mathbf{M}_L \otimes \mathbf{L}) \mathbf{u}^n(\lambda_m) \otimes \mathbf{v}^m \\ &= \mathbf{M}_1 \mathbf{u}^n(\lambda_m) \otimes \mathbf{v}^m + \mathbf{M}_L \mathbf{u}^n(\lambda_m) \otimes \mathbf{L} \mathbf{v}^m \\ &= \mathbf{M}_1 \mathbf{u}^n(\lambda_m) \otimes \mathbf{v}^m + \lambda_m \mathbf{M}_L \mathbf{u}^n(\lambda_b) \otimes \mathbf{v}^m \\ &= (\mathbf{M}_1 + \lambda_m \mathbf{M}_L) \mathbf{u}^n(\lambda_m) \otimes \mathbf{v}^m \\ &= \mu_{n,m} \mathbf{v}^{n,m} \end{aligned}$$

The proof for the left Jacobian eigenvectors can be done similarly. \square

Example 3.6 (Swing Equation). *The dynamics of the swing equation is given by*

$$\begin{aligned} \dot{\theta}_i &= \omega_i \\ M_i \dot{\omega}_i &= P_i - D_i \omega_i - \sum_j V_i V_j B_{ij} \sin(\theta_i - \theta_j) \end{aligned}$$

for every node i in the network. For small angle differences, we can linearize the sine function and get

$$M_i \dot{\omega}_i = -D_i \omega_i - \sum_j L_{ij} \theta_j ,$$

where \mathbf{L} is a weighted Laplacian with weights $w_{ij} = V_i V_j B_{ij}$ on a line between i and j . If we assume homogeneity of the parameters $D_i = D$ and $M_i = M$, we can write the Jacobian of the swing equation in the form (3.25) by defining the matrices

$$\mathbf{M}_1 = \begin{bmatrix} 0 & 1 \\ 0 & -\frac{D}{M} \end{bmatrix} , \quad \mathbf{M}_L = \begin{bmatrix} 0 & 0 \\ -\frac{1}{M} & 0 \end{bmatrix} .$$

The Jacobian eigenvalues are given by the eigenvalues of

$$\mathbf{M}_1 + \lambda_i \mathbf{M}_L = \begin{bmatrix} 0 & 1 \\ -\frac{\lambda_i}{M} & -\frac{D}{M} \end{bmatrix},$$

and hence

$$\mu_{\pm,i} = \frac{-D \pm \sqrt{D^2 - 4M\lambda_i}}{2M}.$$

For the zero eigenvalue of the Laplacian $\lambda_1 = 0$ we have $\mu_{+,1} = 0$ and $\mu_{-,1} = -\frac{D}{M}$. The eigenvalue $\mu_{+,1}$ is due to the rotational symmetry in the swing equation and corresponds to a homogeneous phase shift in all phase angles θ_i that does not affect the dynamics of the system. The eigenvalue $\mu_{-,1}$ corresponds to a homogeneous exponential decay of all frequencies ω_i . This is the only overdamped eigenmode of the system if the Fiedler eigenvalue of the weighted Laplacian fulfills the condition

$$\lambda_2 > \frac{D^2}{4M}.$$

A linear response theory for the swing equation has been derived for the first time in [145]. By perturbing the system at different frequencies, the authors identify three distinct frequency regimes in the response. For low frequencies, the angular velocities behave as a homogeneous bulk. In the resonant regime, the frequency of the perturbation overlaps with the eigenmodes of the system and the response strength of each node is determined by the entries of the corresponding Laplacian eigenvectors. Finally, for high frequencies, the response is suppressed and localized, as the response strengths decay as a power law in frequency and exponentially over the topological distance.

In the course of this chapter, I have shown that the results found in [145] can to some extent be generalized to other dynamical models with diffusive coupling. However, some of the observed phenomena are also specific to the swing equation model and a certain choice of parameters. The bulk regime is always existent as the bulk mode that corresponds to the zero eigenvalue of the Laplacian is always overdamped. However, as shown in Example 3.6, this is not necessarily the only overdamped mode in the system. For $\lambda_2 < \frac{D^2}{4M}$ there is more than one overdamped mode in the system and the low frequency response of the nodes will no longer be homogeneous but is rather determined by a superposition of the eigenvectors of all overdamped modes. Further, the resonant regime only exists, if the Jacobian of the network system has complex eigenvalues. This is not necessarily the case for all diffusively coupled models, e.g. for networks of classical Kuramoto oscillators [70, 71], where the system Jacobian is equal to the network Laplacian, which is a symmetric matrix and therefore always has real eigenvalues (this is also mentioned in the supplemental material of [145]). But also for the swing equation there exists a parameter regime where all modes are overdamped. This is the case for $\lambda_{max} < \frac{D^2}{4M}$,

so either for large damping or for low inertia. Finally, the direct relation of the node response strengths to the Laplacian eigenvectors is only given in the case of a homogeneous parametrization in the network. In general, the response strength of the nodes is determined Jacobian eigenvectors. As shown in Proposition 3.4, these are only directly related to the Laplacian eigenvectors for homogeneous parametrization. Hence, for heterogeneous systems, the response dynamics becomes more complex as it is no longer only determined by network topology but also by the dynamical parameters at the individual nodes.

Chapter 4

The Impact of Renewable Power Fluctuations on the Grid Frequency

In the previous chapter I developed a linear response theory for complex systems on network structures with stochastic perturbations. In this chapter I will apply this theory to analyse the impact of renewable power infeed on the grid frequency stability using stochastic models for short-term wind and solar power fluctuations. The intermittent nature of these fluctuations stems from atmospheric turbulence which are therefore characterized by a strong autocorrelation and a power-lawed spectral density. It will be explained how this property results in a much stronger excitation of the low frequency eigenmodes of the system. Moreover, I will show that the response of the system is dominated by a single eigenmode that corresponds to a global frequency fluctuation of the synchronous bulk.

In the analysis, I will place a special focus on the role of Ohmic losses in the transmission lines, as these have been shown to fundamentally alter the frequency response pattern in microgrid simulations [14]. In particular, I will give an analytical explanation for the observation that power fluctuations are amplified in the opposite direction of the power flow. The existence of this phenomenon in more realistic systems is confirmed by simulations of wind and solar fluctuations in the IEEE RTS-96 test case. The results presented in this chapter have been published in [99].

4.1 Variations of the Grid Frequency

One of the fundamental challenges for the stable operation of power grids is to maintain the balance between power production and power demand. In AC power grids, the occurrence of power imbalances leads to changes of the

grid frequency. This relationship stems from the electromechanical design of synchronous machines which can in its simplest form be described by the swing equation

$$M_i \cdot \Delta \dot{\omega}_i = P_i^m - P_i^e - D_i \cdot \Delta \omega_i .$$

Here, $\Delta \omega_i$ is the frequency deviation from the nominal grid frequency that is caused by an imbalance of the mechanical and electrical power P_i^m and the P_i^e . The dynamical transient is determined by the inertia parameter M_i and the droop control parameter D_i . When several synchronous machines are connected via an electrical grid they can synchronize their frequency in a self-organizing process. In a synchronous steady state we have $\Delta \dot{\omega}_i = 0$ and $\Delta \omega_i = \Delta \omega_{global}$. Assuming the system to be in such a state and summing over all generators yields

$$\Delta \omega_{global} = \frac{\sum_{i \in \mathcal{V}_G} (P_i^m - P_i^e)}{\sum_{i \in \mathcal{V}_G} D_i} .$$

The sum over all electrical powers in the system is determined by total load demand P_{load} and the total amount of Ohmic transport losses on the branches P_{loss}

$$\sum_{i \in \mathcal{V}_G} P_i^e = P_{load} + P_{loss} .$$

By denoting the total amount of mechanical powers as $P_{Gen} = \sum_{i \in \mathcal{V}_G} P_i^m$ we finally get

$$\Delta \omega_{global} = \frac{P_{Gen} - P_{load} - P_{loss}}{\sum_{i \in \mathcal{V}_G} D_i} .$$

Hence, any persistent global imbalance between power generation, power demand and transport losses leads to an offset of the global synchronous frequency. The size of the offset is determined by the sum of all droop coefficients. In contrast, the inertia parameter determines the rate of change of frequency (RoCoF) for a sudden change in the power balance. Abrupt changes of either power demand or generation can induce oscillations around the synchronous frequency.

In real power grids the grid frequency is fluctuating all the time. These fluctuations are a result of constantly varying power demand, fluctuations of renewable energy sources (RES), as well as so-called re-dispatches of the power in-feed of conventional generators in accordance with trading intervals of the energy marked [111]. Figure 4.1 depicts a GPS synchronized measurement of the grid frequency at four different locations in the continental European grid. Here, it can clearly be seen that this is a synchronized system at continental scale and that local frequencies only slightly deviate from the (varying) synchronous frequency.

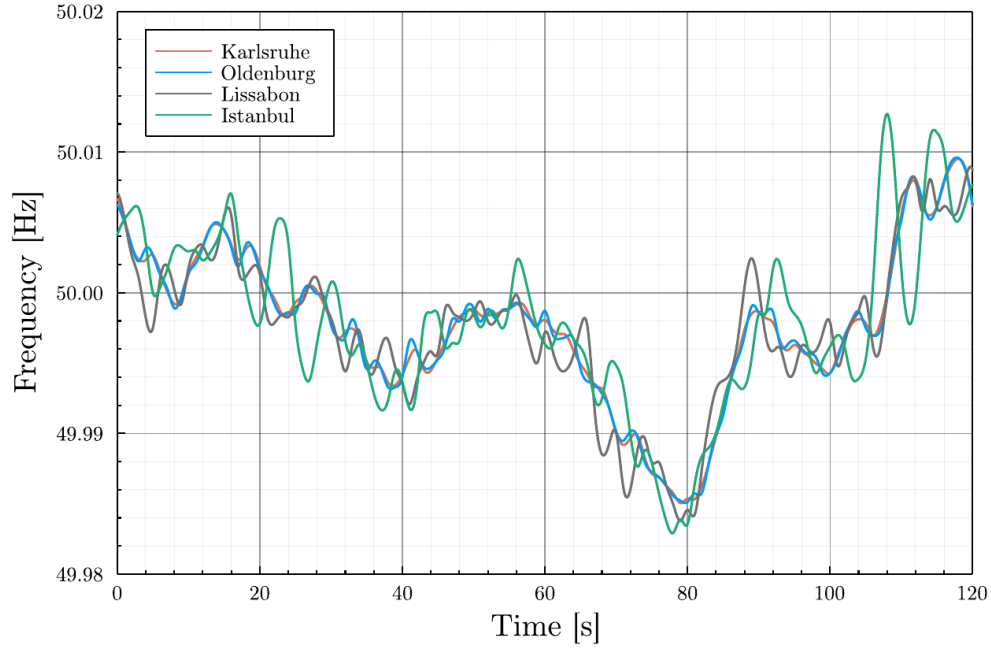


Figure 4.1: Data snippet from a GPS synchronized measurement of the grid frequency at different locations in the continental European grid. The frequency data is taken from the *Power grid frequency database* [62, 48]. It has a temporal resolution of 0.1s and is interpolated with cubic splines.

4.1.1 The Role of Renewable Power Sources

Solar and wind power plants are interfaced with the AC power grid through DC-AC inverters and AC-DC-AC converters, respectively. For wind turbines this means that although they are basically electrical generators, the rotors are non-synchronous with the grid frequency. For such power electronic interfaced power sources there exists no natural relation between frequency as in the case of synchronous machines. Any such relation has to be imposed by applying additional control schemes, such as a droop control. However, to this day most wind and solar power plants are connected to the grid in a grid-feeding mode and do not contribute to either the momentary reserve or the primary frequency control in the grid.

Furthermore, solar and wind power are non-dispatchable, i.e. they cannot be adjusted to the demand and fluctuate in accordance with the current wind speed and solar irradiance, respectively. Due to atmospheric turbulence, these fluctuations are not only present on timescales of hours and days, but also on the timescale of seconds [8, 83]. A major difference between demand fluctuations and renewable fluctuations is that as long as there are no such effects as demand synchronization, e.g. due to real-time pricing in the electricity market [69, 86],

demand fluctuations are typically uncorrelated. According to the law of large numbers we can therefore expect them to balance out. For wind power on the other hand, the correlation of fluctuations at different turbines or panels within a single wind or solar park are typically quite high and hence, these fluctuations add up [8]. For offshore wind parks with up to 1 GW of installed capacity, this implies potentially large power fluctuations at a single bus in the transmission grid. Moreover, these fluctuations can be spatially correlated over very long distances, given the long-range correlations of wind velocity and cloud size distributions of ~ 600 km and ~ 2100 km, respectively [18, 144]. The most extreme example for a large spatially correlated change solar radiation is probably the case of a solar eclipse [106].

Replacing conventional power sources by wind and solar power has therefore two destabilizing effects: First, reducing the number of synchronous machines in the grid also decreases the number of units that stabilize the grid by contributing to the momentary reserve and primary control. Second, increasing the number of intermittent power sources may also increase the level of power fluctuations that are strongly correlated in space and time.

4.1.2 Performance Measures for Frequency Fluctuations

In many theoretical studies on the dynamics and control of swing equation networks [133, 134] and the impact of renewable fluctuations on power grids [131] the frequency dynamics has been quantified in terms of a quadratic measure of the deviation from the average frequency. Following [7], I denote this measure as the *Synchronization Norm*.

Definition 4.1 (Synchronization Norm).

$$\|\mathcal{S}\|_{sync}^2 = \lim_{T \rightarrow \infty} \frac{1}{T} \int_0^T \frac{1}{N} \sum_{k=1}^N \left(\omega_k(t) - \frac{1}{N} \sum_{l=1}^N \omega_l \right)^2 dt. \quad (4.1)$$

Remark. The synchronization norm is a special case of the L_2 signal norm for stochastic systems (3.14) with output defined as

$$\mathbf{y}(t) = \frac{1}{\sqrt{N}} \left(\mathbf{I}_{N \times N} - \frac{1}{N} \mathbf{1}_{N \times N} \right) \boldsymbol{\omega}(t).$$

The synchronization norm has shown to be convenient since it simplifies some analytical calculations. However, from the point of view of the application it is not only necessary that the system remains in a synchronized state, but also should the deviation of the synchronous (average) frequency from the operating state with a certain nominal grid frequency be as small as possible. In Figure 4.1 it can be seen that this deviation is in fact typically larger than the spread between the individual frequency signals. For this reason I introduce an alternative measure that quantifies the deviation of the system from its operation point and which I therefore denote as the *System Deviation Norm*.

Definition 4.2 (System Deviation Norm).

$$\|\mathcal{S}\|_{dev}^2 = \lim_{T \rightarrow \infty} \frac{1}{T} \int_0^T \frac{1}{N} \sum_{k=1}^N (\omega_k(t) - \omega_s)^2 dt . \quad (4.2)$$

Remark. In the co-rotating reference frame of the nominal synchronous frequency ω_s , the system deviation norm is a special case of the L_2 signal norm for stochastic systems (3.14) with output defined as

$$\mathbf{y}(t) = \frac{1}{\sqrt{N}} \boldsymbol{\omega}(t) .$$

In some cases it might also be interesting not to quantify the deviation for the whole system but only for a single bus or node in the network. For that I also introduce the *Single Node Deviation Norm*.

Definition 4.3 (Single Node Deviation Norm).

$$\|\mathcal{S}_j\|_{dev}^2 = \lim_{T \rightarrow \infty} \frac{1}{T} \int_0^T (\omega_j(t) - \omega_s)^2 dt . \quad (4.3)$$

Remark. In the co-rotating reference frame of the nominal synchronous frequency ω_s , the single node deviation norm is a special case of the L_2 signal norm for stochastic systems (3.14) with output defined as $y(t) = \omega_j(t)$.

4.2 Renewable Power Fluctuations

The properties of wind and solar power are determined by the turbulent processes of the atmosphere dynamics. As a consequence, they are strongly non-Gaussian and highly intermittent [83, 8]. In the context of turbulent flows, intermittency means a repeated transition between steady states and rapid gust. It can be quantified by analyzing the statistics of the increments $\Delta_\tau x(t) := x(t + \tau) - x(t)$, where $x(t)$ is an observable, e.g. the wind speed v . For wind power, the relation between wind speed and wind power is given by $P \propto v^3$ and thus, the intermittent behavior can also be seen in the power P . It has been shown for both wind and solar power, that the probability distribution functions of the power increments $\Delta_\tau P$ posses exponential-like heavy tails for different timescales τ . Extreme events up to $20\sigma_t$ have been recorded in wind and solar power data, which emphasizes their strongly non-Gaussian behavior [83, 8]. As previously mentioned, renewable energy sources are primarily controlled in a grid-feeding mode and therefore intermittent power fluctuations are fed directly into the grid. In [50] it was shown that at the subsecond timescale, large frequency increments $\Delta_\tau f > 2$ mHz can be linked to a large in-feed of onshore wind power. A high share of renewable power sources can therefore have a significant impact on the power quality.

However, in [116] it was shown, that intermittency plays only a minor role when assessing the impact of power fluctuations on the grid stability, whereas auto-correlation was found to be much more important.

In the previous chapter, I introduced Wiener-Khinchin theorem, which relates the auto-correlation of a time series or a stochastic process to the power spectral density. The power spectral density of wind and solar power fluctuations is directly affected by turbulent processes in the atmosphere. For the relevant atmospheric quantities, such as the wind speed or the solar irradiance, the power spectrum follows a power law behavior $S(f) \sim f^\alpha$ with the Kolmogorov exponent $\alpha = -5/3$ [8]. Further, it can be shown that if the spectral density of a self-similar signal x scales with a certain exponent α , the spectral density of x^3 will also scale with the same exponent α [83]. Therefore, the spectral density of wind power fluctuations exposes the same power law behavior as for the wind speed and therefore also scales with the Kolmogorov exponent. Similarly, the solar irradiance linearly transforms into solar power [76] and thus, the spectral density of the solar power fluctuations also exposes a Kolmogorov scaling. In time series analyses for wind and solar power data, this behavior has in fact been found for the frequency range $0.001 \text{ Hz} < f < 0.1 \text{ Hz}$ [87, 83, 8].

For wind and solar power plants that are located close to each other are exposed to similar meteorological conditions and therefore the power fluctuations of these plants can be strongly correlated, as can be seen in Figure 4.2. Consequently, the small fluctuations of each plant can potentially add up to fluctuations with larger magnitude. Moreover, in [8] it was shown that the aggregated power fluctuations in wind parks and solar fields retain a high degree of intermittency and autocorrelation.

4.2.1 Stochastic Wind Power Model

A non-Markovian for wind power fluctuations was introduced in [116]. In this model, correlation and intermittency are introduced by coupling two Langevin-type models as

$$\begin{aligned} dx &= x \left(g - \frac{x}{x_0} \right) dt + \sqrt{Dx^2} y dt, \\ dy &= -\gamma y dt + dw(t). \end{aligned}$$

Here, $w(t)$ is a scalar Wiener process and the coupling parameter D controls the intermittency and correlation of the process $x(t)$. The wind power fluctuation is then given by multiplying the stochastic process $x(t)$ with a magnitude parameter p_w

$$\delta P_w(t) = p_w \cdot x(t).$$

All parameters are determined by fitting the process to measured wind power data.

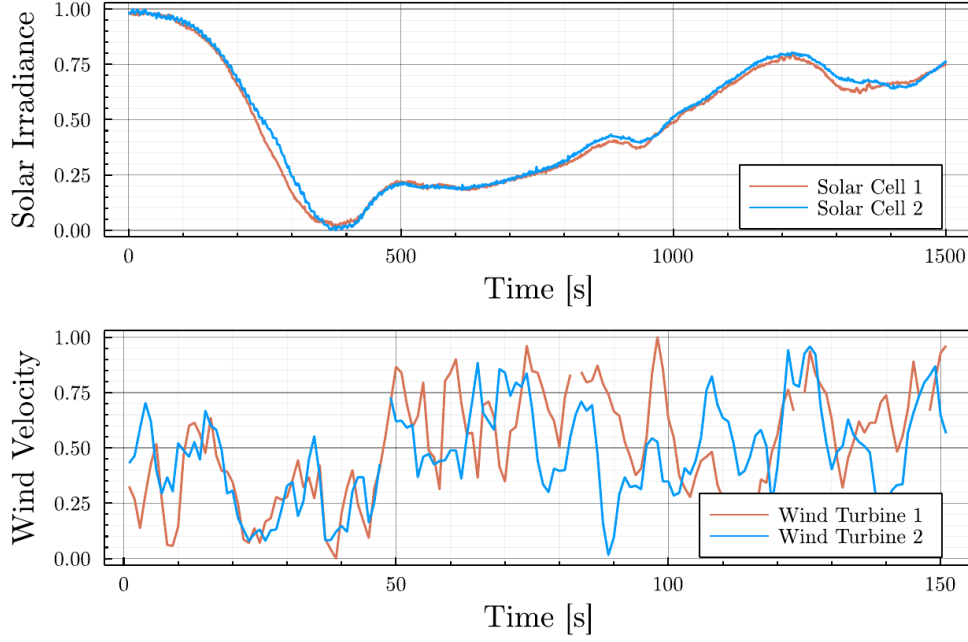


Figure 4.2: Normalized data samples for wind velocity and solar irradiance. The wind velocity data was recorded in a wind park near Bremen in July 2009. The plot depicts data samples for two of overall 12 wind turbines. The solar irradiance data was recorded in June 1993 on the rooftop of the University of Oldenburg. The plot shows data samples for two of overall 11 sensors. The sampling frequency for all measurements is 1 Hz. The data sets were published as supplemental material for the publication [8].

4.2.2 Stochastic Solar Power Model

Solar fluctuations are typically even more jumpy than wind fluctuations. This is mainly due to clouds covering the sun and thereby leading to sudden changes in the solar irradiance. For modeling solar fluctuations we can therefore use a jump-diffusion model [9, 10]

$$dx(t) = D^{(1)}(x, t)dt + \sqrt{D^{(2)}}dw(t) + \xi dJ .$$

Here, $D^{(1)}$ and $D^{(2)}$ are the drift and diffusion constants and $w(t)$ is a scalar Wiener process. $J(t)$ is a time-homogeneous Poisson jump process, that is characterized by the jump rate $\lambda(x, t)$ and the jump size ξ , which is assumed to be normally distributed $\xi \sim \mathcal{N}(0, \sigma_\xi)$. Similar to the case of wind power model, the solar fluctuation is then given by multiplying the stochastic process $x(t)$ with a magnitude parameter p_s

$$\delta P_s(t) = p_s \cdot x(t) .$$

The parameters are determined by fitting the process to measured solar power data.

4.3 Simulations of an AC Microgrid Model

In this section, I will use the the solar and wind power models that were introduced in the previous section to simulate renewable power fluctuations in a conceptual mid voltage (MV) microgrid model. The MV level is a good testing case for modelling power grids with a high renewable energy share, since most PV power plants are connected to LV or MV levels. Assuming the microgrid to be in islanded mode, i.e. there is no connection to a higher grid level, and consequently it has to be must be internally power-balanced.

I use a synthetic grid model of 100 nodes to represent an average German grid at medium-voltage (MV) level [13]. The network topology is generated by the random growth model for power grids [117] that was introduced in Section 2.3.3. Here, the parametrization is chosen to generate tree-shaped grids which is a typical structure for distribution grids. The line impedance for typical MV grids with 20 kV base voltage equals $Z = R + jX \approx (0.4 + 0.3j) \Omega/\text{km}$ [15]. For simplicity all power, voltage and impedance values are transformed into per unit with a base voltage of 20 kV and a base power of 1 MW, which are typical values for MV grids [15, 118]. The absolute impedance of each line scales with the geographic distance between linked nodes and consequently differs per link. Following [15], the average line length is assumed to be 23.7 km.

The nodes in the grid represent an aggregation of all components connected to a bus at the MV level, including all components in a potentially underlying low voltage (LV) network. Whether a node is a net consumer or a net producer depends on the ratio between the overall power demand of the load components and the overall power production of the generating units at that node.

The microgrid is assumed to be dominated by inverters to analyze a scenario with high RES penetration. As previously explained, wind and solar power plants are connected to the grid via inverters. In an islanded scenario, some of these inverters have to be in a grid-forming mode to ensure grid stability. Following [113], I assume that the frequency dynamics of the grid-forming inverters is regulated with a droop control and that they provide synthetic inertia. As shown in Section 2.2.4 the dynamics is then equivalent to the swing equation

$$\begin{aligned} \dot{\delta}_i &= \omega_i, \\ M_i \dot{\omega}_i &= -D_i \omega_i + P_i - P_i^e, \\ P_i^e &= \sum_j V_i V_j [G_{ij} \cos(\delta_i - \delta_j) + B_{ij} \sin(\delta_i - \delta_j)]. \end{aligned} \tag{4.4}$$

The virtual inertia and damping for the network model are determined by the low-pass filter constant $\tau_{p,i}$ and the droop control parameter $k_{p,i}$ as $M_i =$

$\tau_{p,i}/k_{p,i}$ and $D_i = 1/k_{p,i}$. Typical parameters for the droop and time constants of grid-forming inverters are in the range $k_p = [0.1 \text{ s}^{-1} \dots 10 \text{ s}^{-1}]$ and $\tau_p = [0.1 \text{ s} \dots 10 \text{ s}]$ [13, 35, 113]. I assume that there are several grid-forming inverters located at each node and that their collective node dynamics can be aggregated to a dynamics of the form (4.4).

For the grid-feeding inverters and loads I assume that they can be modeled as algebraic constraints that simply inject or withdraw a certain amount of active power into the grid. Therefore, these components do not alter the dynamics (4.4) but simply the amount of injected power. Since grid-feeding inverters (and nodes) do not contribute any (synthetic) inertia, the effective nodes have inertia much lower than nodes fully consisting of grid-forming inverters would have. For the simulations I therefore use $M = 0.1 \text{ s}^2$ and $D = 0.01 \text{ s}$.

The net power injected by all loads and grid-forming inverters at a node is assumed to be constant on the considered time scale and can thus be aggregated into the parameter P_i . I assume that there are 50 net producers and 50 net consumers with $P_i = \pm 0.2 \text{ MW}$ power in-feed. As there is no connection to upper grid levels, losses have to be compensated locally at each node. Therefore, the power in-feeds are homogeneously adjusted to balance the line losses in the operating state $\tilde{P}_i = (P_i + P_{\text{loss}}/N)$.

For the grid-feeding inverters, the renewable power fluctuations are directly fed into the grid and hence, the aggregated power injection at each node consists of a constant and a fluctuating part

$$P_i(t) = \tilde{P}_i + \delta P_i(t) .$$

The power fluctuation $\delta P_i(t)$ is a combination of fluctuations signals generated with the models for wind and solar power fluctuations, that were introduced in the previous section

$$\delta P_i(t) = 0.5\delta P_{w,i}(t) + 0.5\delta P_{s,i}(t). \quad (4.5)$$

For the sake of simplicity I only consider single bus fluctuations. A simulation of multi-node fluctuation would require certain assumptions on the cross-correlation of renewable power fluctuations at different nodes.

Figure 4.3 depicts an example simulation of the frequency response. It can clearly be seen that although some node frequencies tend to have a larger resonances, the frequency dynamics seems to remain remarkably well synchronized. The largest deviation from the nominal grid frequency results from an overall fluctuation of the average synchronous frequency itself and therefore the magnitude of the deviation is about the same order for all nodes.

However, the magnitude of the frequency responses strongly depends on where the power fluctuations are fed into the network. As depicted in Figure 4.4, renewable power fluctuations in the consumer-heavy branches of the network

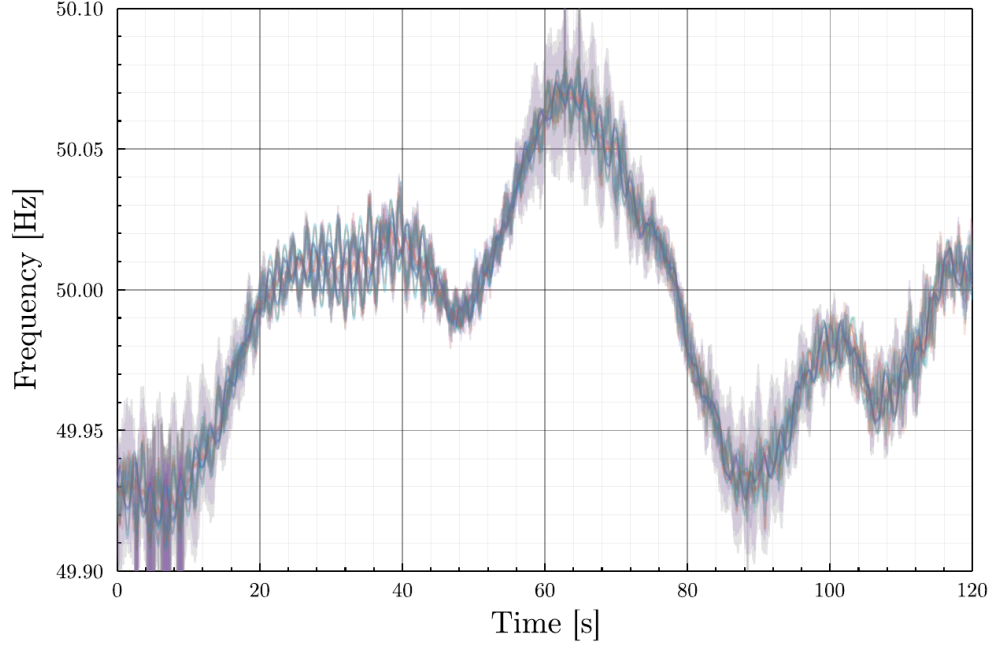


Figure 4.3: Simulation example for the frequency responses of 25 randomly chosen nodes to a renewable power fluctuation (4.5) at a single node in the AC microgrid model.

tend to cause larger frequency responses in the grid. Moreover, the vulnerability of nodes to renewable power fluctuations increases along the direction of the power flow in the network. In [14] it was observed that this effect only occurs if the grid has nonzero resistances.

With the simulation results we can make two substantial observations:

1. The fluctuation of the average frequency is larger than the spread between the individual frequency signals.
2. Renewable power fluctuations at net power sinks seem to cause larger frequency responses in the rest of the grid.

In the remainder of this chapter, I will give analytical explanations for these observations. It will be shown, that the first observation is linked to the highly auto-correlated nature of wind and solar fluctuations and that the second observation is a direct consequence of the resistive line losses.

4.4 Transport Losses on Power Lines

In most theoretical studies on the frequency dynamics in power grids the electrical network is assumed to be purely inductive, i.e. the Ohmic resistance

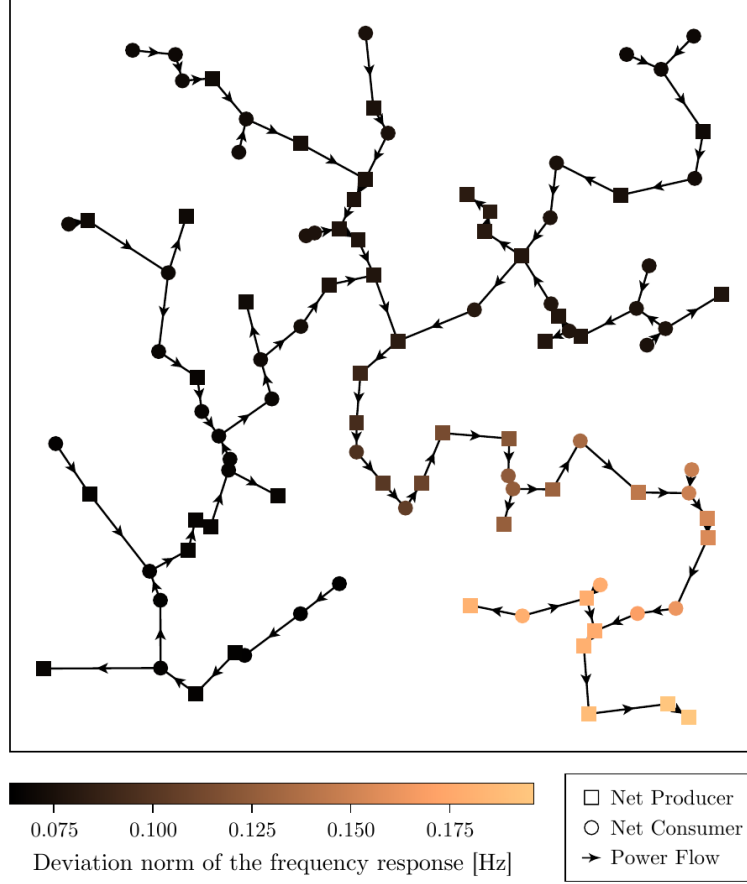


Figure 4.4: Network topology of the AC microgrid model. Each node is colored according to the average frequency deviation that a renewable power fluctuation at this node causes in the grid. The arrows on the lines indicate the direction of the power flow.

is $R_{ij} \approx 0$. The usual justification for this is that on the high voltage level the resistance is typically much smaller than the inductance $R_{ij} \ll X_{ij}$. However, in [53] it was shown that even small line losses can fundamentally alter the nonlinear dynamical behavior of the system and in [14] it was observed that line losses have a major influence on the response pattern to renewable fluctuations in AC microgrids. In this chapter, I will give an analytical explanation for these patterns and show that they originate from the asymmetry that is caused by the line losses.

The active power flow on a line between two buses i and j is given by

$$P_{ij}(\theta_i, \theta_j) = V_i V_j [G_{ij} \cos(\theta_i - \theta_j) + B_{ij} \sin(\theta_i - \theta_j)] . \quad (4.6)$$

Neglecting the voltage dynamics, the power flow on the line is a nonlinear

diffusive function. By the term *diffusive* I mean that the function depends only on the state difference of the bus voltage angles $P_{ij} = P_{ij}(\theta_i - \theta_j)$. In Section 3.4.2 I have shown that for diffusive network systems we can define a Laplacian matrix that describes the linearized dynamical interaction between the network nodes. Usually, Laplacians are defined to be symmetric matrices, with the underlying assumption that the flow on the network branches is conserved. However, if we consider Ohmic losses, i.e. $R_{ij} > 0$ the Laplacian matrix describing the diffusion dynamics on the linear level becomes asymmetric.

Definition 4.4 (Asymmetric Weighted Laplacian). *A weighted Laplacian matrix with elements*

$$L_{ij} = \delta_{ij} \sum_l w_{il} - w_{ij} , \quad (4.7)$$

and weights $w_{ij} > 0$, is called asymmetric, if $\mathbf{L}^T \neq \mathbf{L}$.

Compared to the symmetric weighted Laplacian, the asymmetric weighted Laplacian maintains the properties that the weights are positive and that all row sums equal zero. From the latter it follows also that they always have an eigenvalue $\lambda_1 = 0$ and that the corresponding right eigenvector is homogeneous $\mathbf{v}_{r,i}^{(1)} = \mathbf{v}_{r,j}^{(1)}$. However, the column sums are generally not equal to zero and thus, the corresponding left eigenvector is heterogeneous.

Lemma 4.1. *For neighboring nodes in tree networks the entries of the left eigenvector corresponding to $\lambda_1 = 0$ of the asymmetric Laplacian (4.7) are related by*

$$\frac{\mathbf{v}_{l,i}^{(1)}}{\mathbf{v}_{l,j}^{(1)}} = \frac{w_{ji}}{w_{ij}} . \quad (4.8)$$

Proof. For the left Laplacian eigenvector corresponding to $\lambda_1 = 0$ we have the condition

$$0 = \sum_i \mathbf{v}_{l,i}^{(1)} L_{ij} = \sum_i (\mathbf{v}_{l,i}^{(1)} w_{ij} - \mathbf{v}_{l,j}^{(1)} w_{ji}) =: \sum_i F_{ij} .$$

For a node j the number of summands is equal to its degree d . In a tree graph \mathcal{G} with size $N \geq 2$ there are always at least two nodes with degree $d = 1$. At these nodes there is only one summand F_{ij} which therefore has to be zero. Given the fact that the summands are antisymmetric $F_{ij} = -F_{ji}$, it follows that the corresponding summands F_{ji} in the conditions for the neighboring nodes also have to be zero. This implies that the existence of nodes with $d = 1$ does not have an impact on the condition at all other nodes in the graph and we can therefore also analyze the conditions for the reduced graph \mathcal{G}' where all nodes with $d = 1$ have been removed. This graph is again a tree that has nodes with degree $d' = 1$. Again, for these nodes the summand F_{ij} and the antisymmetric counterpart F_{ji} in the condition of their neighbors have to be

zero. Continuing this procedure, we can step by step reduce the graph and thereby show that in fact every single summand F_{ij} has to be zero, which implies (4.8). \square

For dynamics in AC power grids, the weights w_{ij} describe the rate at which the power flow changes to a certain change in the voltage angle difference

$$w_{ij} = \frac{\partial p_{ij}}{\partial \theta_{ij}}.$$

Inserting the line flow (4.6) yields

$$w_{ij} = |V_i||V_j|[B_{ij} \cos(\theta_{ij}) - G_{ij} \sin(\theta_{ij})]. \quad (4.9)$$

Assumption 4.1 (Voltage Angle Difference). *For all power lines in the electrical network the voltage angle difference fulfills the following conditions:*

1. $|\theta_i - \theta_j| \leq \frac{\pi}{2}$.
2. $X_{ij}/R_{ij} > \tan(\theta_k - \theta_l)$

In reality these assumptions are almost always fulfilled. The first condition is necessary to have a stable operation point [40]. Concerning the ratio of line inductance and resistance, we typically have $X_{ij} \gg R_{ij}$ in high voltage (HV) grids and $X_{ij} \sim R_{ij}$ in MV grids [109]. In the case of $X_{ij} = R_{ij}$, both conditions are fulfilled if $|\theta_i - \theta_j| < \frac{\pi}{4}$. This upper threshold corresponds to a line load of $\sim 70\%$ of its physical capacity and it usually not exceeded during normal operation.

Given Assumption 4.1, the weights (4.9) are always positive and we can define an asymmetric Laplacian matrix (4.7) that describes the dynamical interaction in the electric grid.

Proposition 4.1. *In tree-shaped grids with Ohmic losses $R_{ij} > 0$, the entries of the left Laplacian eigenvector corresponding to the zero eigenvalue $\lambda_1 = 0$ are increasing along the direction of the power flow in the network.*

Proof. The Laplacian weights for the active power flow on on a line (4.6) are given by

$$\begin{aligned} w_{ij} &= |V_i||V_j|[B_{ij} \cos(\theta_{ij}) - G_{ij} \sin(\theta_{ij})], \\ w_{ji} &= |V_i||V_j|[B_{ij} \cos(\theta_{ij}) + G_{ij} \sin(\theta_{ij})]. \end{aligned}$$

From the definition of the nodal conductance and susceptance matrix it follows that

$$G_{ij} = -\frac{R_{ij}^2}{R_{ij}^2 + X_{ij}^2}, \quad B_{ij} = -\frac{X_{ij}^2}{R_{ij}^2 + X_{ij}^2}.$$

Assuming that the power flows from i to j , i.e. $\theta_i > \theta_j$, it follows that $G_{ij} \sin(\theta_{ij}) < 0$ and therefore $w_{ij} > w_{ji}$. Using the result of Lemma 4.1 finally yields

$$v_{l,i}^{(1)} > v_{l,j}^{(1)} .$$

□

4.5 Linear Response of the Frequency

In this section I will assume that all node dynamics in the power network are described by the swing equation and a coupling by an active power flow, as described in Equation (4.4). Generally, the derivations can also be generalized to more complex node dynamics (see [99]) but here I will focus on the simple case of swing equations that captures the essential properties of the frequency dynamics in power systems.

Defining the parameter vectors $\mathbf{d} \in \mathbb{R}^n$ and $\mathbf{m} \in \mathbb{R}^n$ for the damping and inertia parameters, the Jacobian of the swing equation can be written as

$$\mathbf{A} = \begin{bmatrix} \mathbf{0}_{n \times n} & \mathbf{I}_{n \times n} \\ -\mathbf{M}^{-1}\mathbf{L} & -\mathbf{M}^{-1}\mathbf{D} \end{bmatrix} , \quad (4.10)$$

with the diagonal parameter matrices $\mathbf{D} = \text{diag}(\mathbf{d})$ and $\mathbf{M} = \text{diag}(\mathbf{m})$ and the weighted network Laplacian \mathbf{L} . When considering finite Ohmic losses on the lines $R_{ij} > 0$ the Laplacian will be asymmetric, as explained in the previous section.

When the dynamics is given in the co-rotating reference frame, the synchronous operating state $\mathbf{x}^\circ = [\boldsymbol{\theta}^{\circ T}, \boldsymbol{\omega}^{\circ T}]^T \in \mathbb{R}^{2n}$ is given by $\omega_i^\circ = 0$ and the solution of the AC power flow equations

$$P_i = V_i V_j [G_{ij} \cos(\theta_i^\circ - \theta_j^\circ) + B_{ij} \sin(\theta_i^\circ - \theta_j^\circ)] .$$

Now I assume that there is a power fluctuation δP at a single bus in the system. In order to analyze the frequency response to that perturbation we can linearize the system around the operating state as $\mathbf{x} = \mathbf{x}^\circ + \delta \mathbf{x}$ which yields the linear time-invariant (LTI) system

$$\begin{aligned} \delta \dot{\mathbf{x}} &= \mathbf{A} \cdot \delta \mathbf{x} + \mathbf{B} \cdot \delta \mathbf{P} , \\ \mathbf{y} &= \mathbf{C} \cdot \delta \mathbf{x} , \end{aligned} \quad (4.11)$$

where \mathbf{A} is the Jacobian (4.10) and $\delta \mathbf{P}$ is the vector of power fluctuations. For a single bus fluctuation at bus k , the fluctuation is a scalar $\delta \mathbf{P} = \delta P$ and the matrix $\mathbf{B} \in \mathbb{R}^{2n \times 1}$ is given by

$$\mathbf{B} = \begin{bmatrix} 0 \\ \mathbf{e}^{(k)} \end{bmatrix} , \quad \mathbf{e}_i^{(k)} = \begin{cases} 1 & \text{if } i = k , \\ 0 & \text{else .} \end{cases}$$

For quantifying the frequency response in terms of the single node deviation norm (4.3), the matrix $C \in \mathbb{R}^{n \times 2n}$ has to be defined as

$$C = \begin{bmatrix} 0 & e^{(j)^T} \end{bmatrix}, \quad e_i^{(j)} = \begin{cases} 1 & \text{if } i = j, \\ 0 & \text{else.} \end{cases}$$

For the LTI system (4.11) we can apply the linear response theory that was derived in the previous chapter. From Corollary 3.3.1 it follows that the response function of the system can be written as

$$H(t) = \sum_{n=1}^N v_{r,j}^{(n)} v_{l,k}^{(n)} e^{\mu_n t} \Theta(t),$$

where μ_n are the eigenvalues of the Jacobian (4.10) and $v_l^{(n)}, v_r^{(n)}$ the corresponding left and right eigenvectors. We see that the left eigenvector determines how strong a mode gets excited for a perturbation at a certain bus, whereas the right eigenvector determines how strong the response to that mode is at each bus. The superposition of all modes gives a particular network response pattern in the system (see Figure 4.5). In Section 3.3.2 I have shown that the contribution of each mode to that response pattern can be quantified in terms of a spectral excitation factor

$$S^{(n)} = \frac{1}{2\gamma_n} \int_{-\infty}^{\infty} k^{(n)}(\nu) S_{pp}(\nu) d\nu. \quad (4.12)$$

Here, S_{pp} is the power spectral density of the power fluctuation δP and

$$k^{(n)}(\nu) = \frac{1}{\pi} \frac{\gamma_n}{\gamma_n^2 + (\nu - \nu_n)^2}$$

are normalized Lorentz functions with the mode damping $\gamma_n = \Re(\mu_n)$ and eigenfrequency $\nu_n = \Im(\mu_n)$. The power spectral density of solar and wind power fluctuations are following a power law behavior, i.e. the fluctuations are much stronger at lower frequencies. Consequently, the spectral excitation factor (4.12) is then much larger for eigenmodes with lower eigenfrequencies and those will therefore have a stronger contribution to the response.

For a more detailed analysis I will now make the assumption that the damping and inertia parameters are homogeneous in the network. In Example 3.6 I have shown that in this case the Jacobian eigenvalues are given by

$$\mu_{\pm,i} = \frac{-D \pm \sqrt{D^2 - 4M\lambda_i}}{2M},$$

where λ_i are the eigenvalues of the network Laplacian. The mode with eigenvalue $\mu_{-,1} = -\frac{D}{M}$ (corresponding to the Laplacian eigenvalue $\lambda_1 = 0$) is always

real and therefore has the eigenfrequency $\nu_{-,1} = \Im(\mu_{-,1}) = 0$. As a consequence, this eigenmode will always be one of the strongest excited modes in the network. In fact, if the Fiedler eigenvalue of the weighted Laplacian fulfills the condition

$$\lambda_2 > \frac{D^2}{2M},$$

this mode is the only system eigenmode with zero eigenfrequency. For the microgrid system in Section 4.3 this condition is fulfilled and we even have $\lambda_2 \gg \frac{D^2}{4M}$, which means that all other eigenmodes will be suppressed compared to the single overdamped mode, as the power spectral density at their eigenfrequencies is much lower.

In Proposition 3.3 I have shown that for homogeneous node parameters the Jacobian eigenvectors can be separated into the eigenvectors of the Laplacian and the eigenvectors of the internal dynamics. Hence, the spatial response pattern of the network to a certain mode is fully determined by the corresponding left and right eigenvectors of the Laplacian. The right eigenvector that corresponding to $\lambda_1 = 0$ has homogeneous entries and therefore all nodes exhibit an equal response to the single overdamped eigenmode. The fact that this mode dominates the system response explains the bulk behavior of the frequency signals that has been observed in the microgrid simulations (See Figure 4.3). In the following, I will therefore refer to this mode as the *bulk mode*.

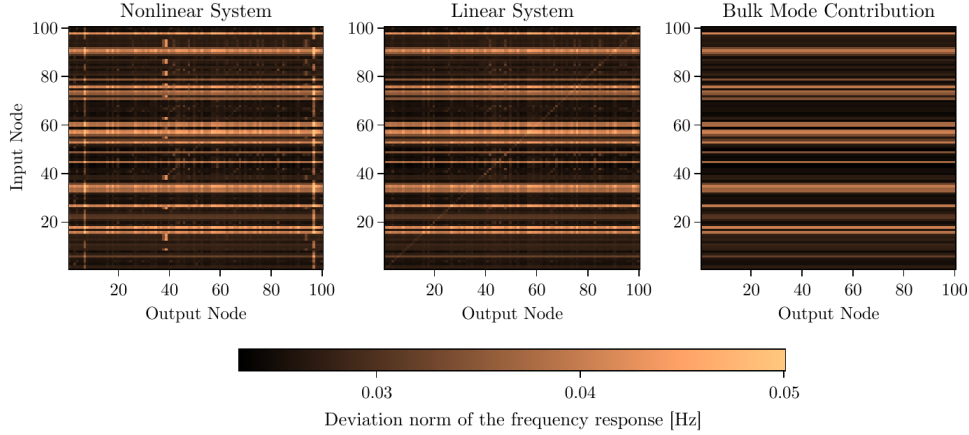


Figure 4.5: Node response pattern for the microgrid simulation described in Section 4.3. The fluctuation (4.5) is applied at the input nodes and the response is measured at the output nodes in terms of the single node deviation norm (4.3). The system deviation norm (4.2) is obtained by averaging over the output nodes. The ordering of the nodes in this plot is arbitrary.

As shown in the previous section, when there are Ohmic losses on the lines,

the network Laplacian is asymmetric and its left eigenvectors are heterogeneous. Consequently, the excitation strength of the bulk mode depends on which node in the network is perturbed. Since the bulk mode is dominating the system responds, there is a strong asymmetry between the heterogeneity of the input and the homogeneity of the output. Figure 4.5 depicts this asymmetry in the response pattern for the full nonlinear system, the linearized system and the contribution of the bulk mode. Except for some nonlinear effects at a few output nodes, the linearized system description is able to capture the response pattern of the full nonlinear system. Further, it can clearly be seen that the linear response is dominated by the bulk mode pattern which is in fact homogeneous in the outputs and strongly heterogeneous in the inputs.

In Proposition 4.1 it was shown that in tree-shaped networks the entries of the left Laplacian eigenvector corresponding to the zero eigenvalue are increasing along the power flow. From this, it directly follows that the bulk mode excitation is stronger at the sinks of the power flow which is exactly what we have observed in the simulations of the microgrid example (see Figure 4.4). In the remainder of this section I will try to give an explanation why this is the case. Suppose there is a single line with Ohmic losses that connects two buses, one of which is a source and one of which is a sink (see Figure 4.6). The dissipation on the line has the property that it is monotonously increasing with the magnitude of the flow, i.e. a larger flow results in higher losses and vice versa. This means that a change in injected power at the source bus will partially be compensated by the adjusted amount of dissipation. Conversely, a change in power drawn at the sink bus requires a larger adjustment at the source bus to account for the additional adjustment of the dissipated power. In summary, we can conclude that changes of power are weakened in direction of the power flow and get amplified in the opposite direction.

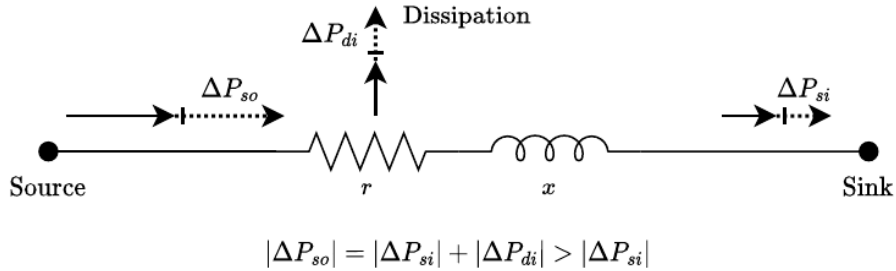


Figure 4.6: Effect of Ohmic losses on power flow changes. The sketch shows an admittance line model composed of a resistive and an inductive element. Any change of the power flow also causes a change of power dissipation in the resistive element. The changes on the source side are therefore always larger than on the sink side of the line.

It should be mentioned that the described effect does neither necessarily depends on the tree-like topology nor the details of the node dynamics. It can therefore be assumed that the observations made in the microgrid simulations and the linear response calculations are more general. This will be verified in the subsequent section.

4.6 Simulations in the IEEE RTS-96 Test Case

In the previous sections I had to make some basic assumptions to maintain the feasibility of the analytical derivations. On the one hand, I assumed that the dynamics of all buses in the network can be described by the swing equation, i.e. there are no plain load buses. Moreover, the analytical separation of internal node dynamics and network interaction necessitated a homogeneous parametrization of the node dynamics. These are admittedly rather strong assumptions. In this section it will be shown that the described phenomena can in fact also be observed in a more realistic grid model. Instead of the simple microgrid model in Section 4.3 I now apply the single node power fluctuations (4.5) to the IEEE RTS-96 test case [49]. This HV transmission grid model consists of 108 branches, including both transmission lines and transformers, as well as 73 buses of which 30 are generator buses and the rest are plain load buses.

With its relatively small number of large generating units this test case resembles a rather conventional power system compared to the renewable microgrid in Section 4.3. I assume that renewable generation units are located at the load buses and that these are all in a grid-feeding mode. The loads are modeled as algebraic constraints that draw a certain amount of power from the grid. I apply renewable power fluctuations to a single load bus at a time and measure the frequency response at the generators. The generators are again modeled by swing equations.

Figure 4.7 depicts the network topology of the IEEE RTS-96 test case. The color of the load buses indicates how much the generator frequencies deviate from the nominal frequency when a single bus fluctuation is applied to that load bus. In contrast to the microgrid model (Figure 4.4) this test case represents a transmission grid and therefore has a highly meshed grid topology. Nevertheless, it can clearly be seen that there are significant differences in the response depending on where the fluctuation is applied. Fluctuations at load buses in generator dominated regions have much less impact as fluctuations in load dominated regions. Within these regions, it can further be seen that the vulnerability to power fluctuations increases along the direction of the power flow. We can therefore conclude that the observation that power fluctuations are amplified in the opposite direction of the flow still seems to hold for realistic power system test cases with meshed topology and heterogeneous dynamical parameters.

4.7 Outlook: Multi-Bus Fluctuations & Optimal Control Schemes

In this chapter, I have only considered single bus fluctuations. For completely uncorrelated multi-bus fluctuations, the linear response is simply given by the superposition of the single bus fluctuations. In large grids with many buses, it follows from the law that such fluctuations would balance out. However, as previously mentioned, renewable fluctuations can potentially be spatially correlated over large distances. To my knowledge there exists no detailed models for the spatial correlation of wind and solar power fluctuations. Certainly, it is also a difficult task to develop such models as spatial correlations can depend on specific meteorological conditions such as cloud sizes or wind directions. What is known from data analyses on the spatial correlation of wind power fluctuations [138], is that for large spatial distances of 200 km, the power fluctuations can still be correlated on the time-scale of hours, but are uncorrelated for smaller timescales. This indicates that in synchronous areas of continental scale, the renewable fluctuations on short-timescales can be assumed to be uncorrelated and hence, if the transport capacity of the grid is large enough they will probably balance out. However, for smaller synchronous areas such as microgrids or electrical grids on smaller islands, it is to be expected that there can be significant spatial correlations and thus, power fluctuations might add up rather than balance out. Certainly, further research on multi-bus fluctuations is needed to evaluate the impact of renewable fluctuations and the effect of spatial correlation in such systems more precisely. The theoretical findings of this chapter already indicate, that a high degree of spatial correlation in power fluctuations will probably lead to an even stronger domination of the bulk mode that basically corresponds to a fluctuating global power imbalance.

Another important implication of this chapter's results is concerning the role of primary (and secondary) control. The literature debate is often focused on the aspect that inverter interfaced power sources decrease system inertia and the momentary reserve. However, for renewable fluctuations I found that the system response is dominated by the overdamped eigenmode that corresponds to quasistatic shifts of the synchronous frequency as a result of global power imbalances. For such quasistatic behavior, the system inertia is actually of less relevance than primary and secondary control, which are the central control schemes for minimizing power imbalances and keeping the system close to the nominal frequency. Future research should therefore investigate the optimal design and placement of primary and secondary controllers in the grid. Although there already exist some studies on that topic [129, 130, 7], they are always based on using the synchronization norm (4.1) instead of the deviation norm (4.2) and therefore omit the most dominant mode for the response to renewable power fluctuations.

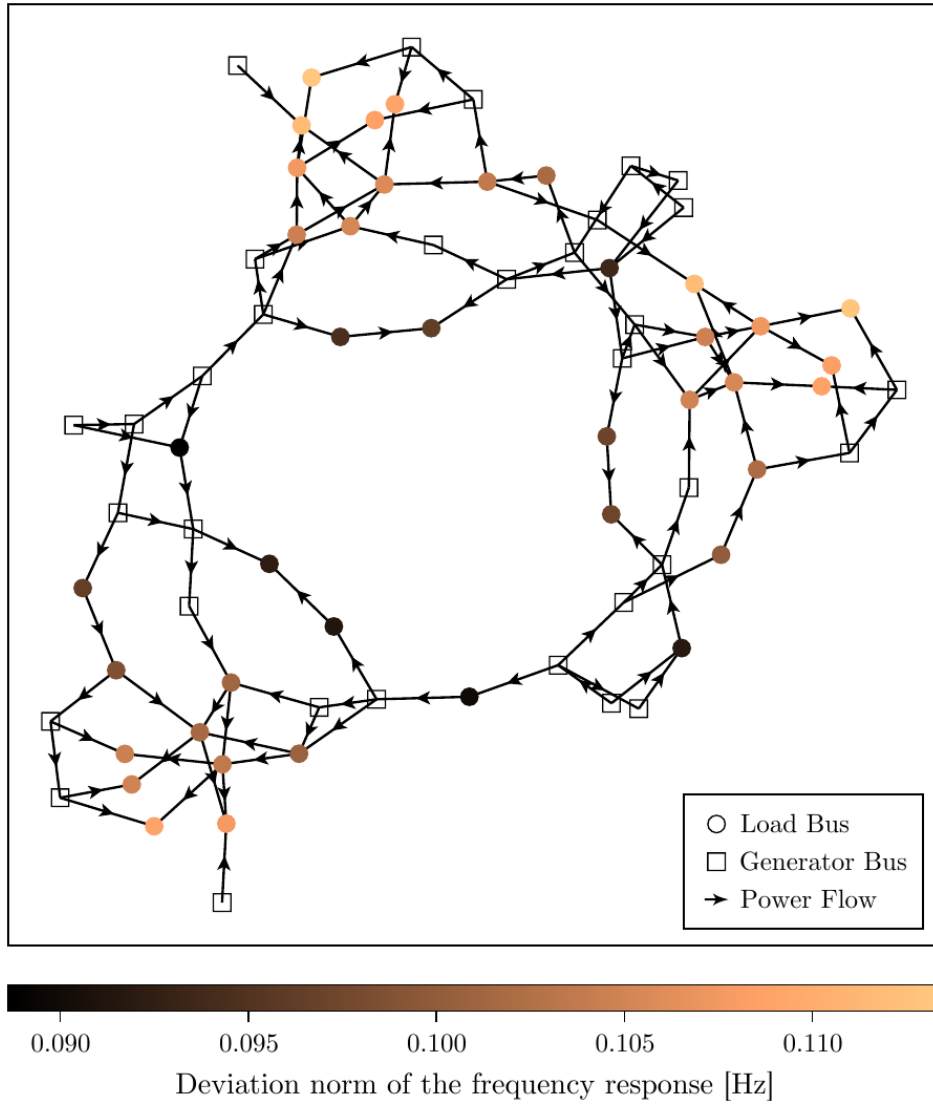


Figure 4.7: Renewable power fluctuations in the IEEE RTS-96 network. The fluctuations (4.5) are applied at each load bus individually. The load buses are colored according to the deviation norm of frequency response of the generators that a fluctuation at that particular bus causes. The arrows on the branches indicate the direction of the power flow.

Chapter 5

Measuring and Modeling Grid-Forming Inverters

In the previous chapter, it was assumed that the collective dynamics of the grid is dominated by dynamical actors that can be described by the swing equation and that fluctuations of RES are directly fed into the grid due to a grid-feeding inverter control mode. The analysis was based on a linearization of the most fundamental nonlinearity in the system, the power flow. Also, the role of reactive power and voltage dynamics have been completely neglected.

The goal of this chapter is to go beyond these assumptions, both contentwise and methodologically. In future power grids, the collective dynamics will not (only) be determined by synchronous machines but also by decentralized grid-forming inverter control schemes.

Given a decreasing share of synchronous machines, the integration of inverter controls that are able to regulate voltage and frequency is absolutely necessary for maintaining grid stability. However, so far grid-forming control schemes have barely been implemented into the real systems and mainly been tested in the context of small microgrids.

In this chapter, I introduce detailed models for the outer control loops of a grid-forming and a grid-following inverter, that have been built at the TecNALIA research center¹. A software implementation of these models is validated with measurements of a small inverter-based microgrid that have been taken out in the TecNALIA laboratory.

Modeling the detailed dynamics of inverter controls can be a quite intricate subject. Contrary to the case of synchronous machines, where a hierarchy of generator models of different order can be found in any standard power engineering textbook, the question of which modeling detail is actually needed to describe the dynamical properties of inverters is an open research question. Moreover, there exists a large variety of different grid-forming control schemes

¹<https://www.tecnalia.com>

that have been proposed in the literature.

In order to address these problems, I derive a normal form model from first principles that is capable of describing the dynamical behavior of any grid-forming actor. Making use of the fundamental symmetry in the synchronous operating state and expanding the dynamics in invariant coordinates of that symmetry preserves the fundamental nonlinearities, including the power flow.

In the last part, it will be shown that the normal form method is also well-suited for a data-driven modeling approach. Using machine learning methods, the normal form model can be fitted to a laboratory measurement of a grid-forming inverter.

All microgrid measurements were carried out with the help of Julia Merino Fernández and Asier Gil-de-Muro. The comparison of measurements and simulations has been published in [100]. The normal form approach presented in this chapter was to a large part developed by Raphael Kogler, while I carried out the fitting of the model to the measurement data. The results have been published in [68].

5.1 The Role of Grid-Forming Inverters in Future Power Grids

To this day the vast majority of wind and solar power plants are connected to the grid in a grid-feeding control mode and do not contribute to the momentary reserve of the system. Consequently, the ongoing replacement of large conventional generators by RES reduces the system stability on the seconds timescale. This problem is more urgent in smaller synchronous areas, such as the Irish and the British power grid. In Ireland there has for several years been an upper limit of 50 % (and later 55 %) for the operation of power electronic interfaced power sources [42]. In the continental European grid the share of conventional generation is still comparatively high as there are several countries with large number of either coal power plants (e.g. Poland) or nuclear power plants (e.g. France). However, increasing CO₂ prices push coal power generation out of the market [97] and many European countries plan to end coal-fired power generation by 2030 [28]. Thus, a significant decrease in total system inertia (TSI) is to be expected during the next decade.

A major concern is that this may lead to severe problems during system splits in the continental grid [32]. A system split occurs when the synchronous region is separated due to a failure of all connections between two or more regions. In 2021 alone, there have been two system splits in the continental European grid [43, 44]. In these cases, the activation of automatic and manual countermeasures by the transmission system operators (TSOs) prevented further spreading of failures and large scale outages. In order to preserve the ability to control such system splits in the future, the amount of momentary reserve has to be increased substantially over the next years. TSOs therefore

claim that it is therefore necessary that as soon as possible all newly installed inverters should be provided with grid-forming control schemes in order to get a sufficient share of grid-forming inverters by 2030 [1].

However, so far there has only been little research on the collective dynamical behavior of such large number of such grid-forming actors. One major problem is, that the control schemes thus also the dynamics behavior of these inverter systems might vary a lot. Contrary to synchronous generators, where the dynamics of the momentary reserve is to a large extent determined by the mechanics of large rotating masses and electromagnetic induction, inverters are power electronic devices with control schemes that can in theory be programmed arbitrarily. In principle, there are at least three methods, that are commonly discussed in the literature:

1. Droop Control, a control scheme that imposes a linear relation between frequency and active power as well as voltage and reactive power [34, 114].
2. Virtual Synchronous Machines, control schemes that emulate the dynamics of synchronous machines [4, 20].
3. Virtual Oscillator Controls, control schemes that emulate the dynamics of nonlinear oscillators [61, 119].

In the subsequent section, I will exemplarily introduce a particular droop control scheme that was designed and build at the Tecnia laboratories.

5.2 Lab Measurements of Inverter Controls

In this section, I will present measurements and simulations of a small AC microgrid with grid-forming and grid-following inverters. The measurements were taken out in January 2020 as part of the VALERIA² project at the microgrid laboratory of Tecnia located in Bilbao. The aim of this project was to experimentally validate the power system simulation software `PowerDynamics.jl`. More details on the software package are given in Appendix A.2. An overview of the simulation and measurement results can be found in the technical report [136] and the paper [100].

5.2.1 Tecnia Inverter Models

Two inverters were available in the microgrid laboratory. The detailed inverter controls were designed and self-built by the laboratory staff at Tecnia [98]. Both inverters can be controlled in either grid-forming mode as a voltage source inverter (VSI) or grid-following mode as a current source inverter (CSI). The

²Validation of low-voltage energy and renewables integration analysis.

control designs are very similar to those described in Section 2.2.4 but come with some additional filters and components.

Due to the high noise level in the microgrid, the current and voltage signals are filtered by a low pass filter

$$\begin{aligned}\frac{1}{\omega_{ci}} \cdot \frac{di_{dq,fil}}{dt} &= -i_{dq,fil} + i_{dq} , \\ \frac{1}{\omega_{cu}} \cdot \frac{du_{dq,fil}}{dt} &= -u_{dq,fil} + u_{dq} ,\end{aligned}$$

where ω_{ci}, ω_{cu} are the cutoff frequencies. The outer control loop for both control modes is a droop control as given in (2.14). The CSI is synchronized with the grid by a PLL control as depicted in Figure 2.3.

The VSI slightly differs from the model depicted in Figure 2.4. The low pass filters for active and reactive power (2.15) are replaced by similar filters with a transfer function given by [98]

$$G(s) = \frac{1 + \frac{s}{n \cdot \omega_{cp}}}{1 + \frac{s}{\omega_{cp}}} .$$

For $n \rightarrow 1$ this filter does not modify the signal, for $n \rightarrow \infty$ it behaves like a normal low pass filter. Additionally, a so-called fictitious impedance is added to the droop control, to ensure a decoupling between active and reactive power. The impedance is built such that it has an inductive behavior for low frequencies and a resistive behavior for high frequencies [98]

$$u_{d,fic} = jX_{fic} \cdot i_{dq,fil} + R_{fic}(i_{dq} - i_{iq,fil}) .$$

Both inverter models have been implemented in `PowerDynamics.jl`³. Details on the single parameters can be found in the technical report [136].

5.2.2 Measurement & Simulation of an AC Microgrid

Consider a small microgrid with a grid-forming inverter, a grid-following inverter and a load. The setup is depicted in Figure 5.1.

As an example, we consider a test case in grid-connected mode (switch in Figure 5.1 is closed) where the active power set point of the VSI is suddenly changed to a different value and then changed back after a couple of seconds. The comparison of the measurements and the simulation results is depicted in Figure 5.2. The system has a transient dynamics and does a little overshoot before settling into the new steady state. This behavior is similarly captured in both the simulation and the measurement. The main difference is merely the strong noise on the measurements.

³<https://github.com/JuliaEnergy/PowerDynamics.jl/tree/tecnalia>

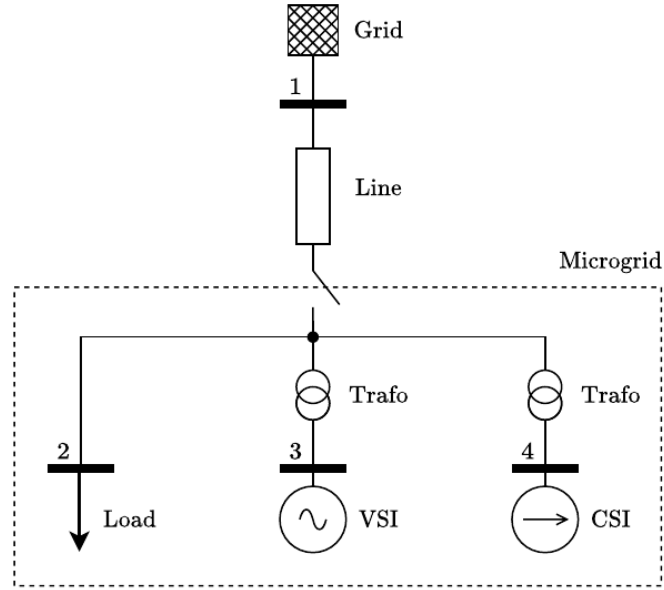


Figure 5.1: Microgrid setup in the laboratory. By opening and closing the switch, the system can either be in grid-connected or in off-grid mode. The line is emulated by a series of resistances and impedances. The inverters are connected to the rest of the microgrid by transformers. Details on the parametrization can be found in the technical report [136]. Measurements of voltage and current are taken at each bus. Due to a limited number of measurement units, only two phases were measured. A balanced system is assumed to calculate the third phase.

5.3 The Normal Form for Grid-Forming Actors

The realistic modeling of inverter controls can be a quite intricate subject and requires detailed knowledge on all underlying control schemes and parameters. As the field of research is still relatively young and there exists a large variety of proposed control schemes, it is often difficult to make general statements on stability and the collective dynamical behavior of a large number of grid-forming inverters.

In this section, I will therefore introduce a more abstract view on grid-forming actors in the system. Instead of focussing on specific details of certain control schemes, I derive a normal form for grid-forming components from first principles. This approach should serve as a starting point for more generalized stability analyses of inverter-based grids, as well as for applying model reduction techniques and data-driven modeling approaches.

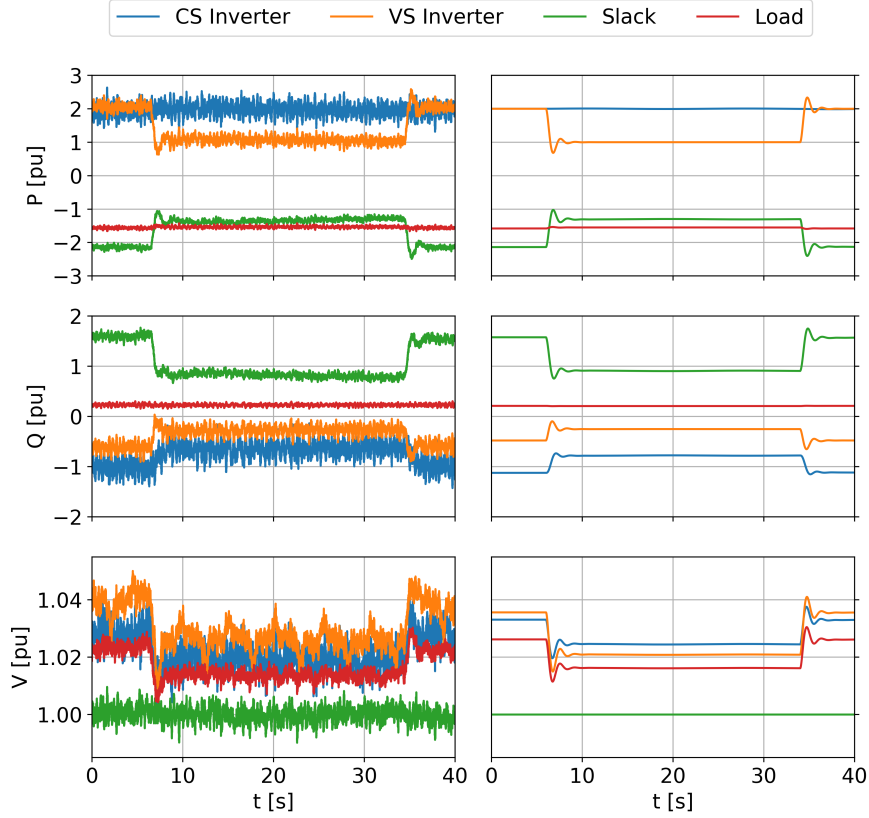


Figure 5.2: Comparison of inverter measurements and simulations. The scenario is a set point dispatch for the active power at the grid-forming inverter in the test grid setup shown in Figure 5.1. Voltage and power signals are calculated from the measured current and voltage signals. The dynamic models for grid-forming and grid-following inverter have been implemented and simulated in *PowerDynamics.jl*. This Figure was first published in [100].

5.3.1 Modeling Assumptions

First of all, we assume that Assumption 2.1 holds, i.e. all 3-phase variables are balanced. Hence, as already shown in Section 2.1.1, 3-phase voltage and current have only two independent variables and can be represented as complex variables

$$u(t) = v(t)e^{j\theta(t)}, \quad i(t) = |i(t)|e^{j\phi(t)}.$$

In Section 2.2.4 it was explained that grid-forming inverters regulate the terminal voltage and is therefore also denoted as voltage control mode (VCM). Hence, in this mode the complex voltage $u(t)$ is a state variable whereas the complex current $i(t)$ is an external input variable. In the following, we will make

additional assumptions on the control and dynamical behavior of grid-forming components that will allow us to derive a generalized model.

Assumption 5.1 (Decentralized Control). *The dynamics of grid-forming components is coupled only by the complex currents $i(t)$ in the electric network.*

This assumption basically means that there exists no additional communication layer that could transfer information the dynamical states of single components.

Assumption 5.2 (Internal State Variables). *Additionally to the complex voltage variable $u(t)$, the grid-forming components may have an arbitrary number N of internal scalar state variables denoted by $\mathbf{x}(t) : \mathbb{R} \rightarrow \mathbb{R}^N$.*

For any internal balanced 3-phase variable z we can define the two scalar variables $\psi := (uz^* + u^*z)/2$ and $\chi := (uz^* - u^*z)/(2i)$ and append these to the vector \mathbf{x} without violating any other assumptions [68].

Assumption 5.3 (Smooth Dynamics). *The dynamics of the grid-forming components is smooth and can be formulated as a system of ordinary differential equations in terms of the internal states $u(t)$, $\mathbf{x}(t)$ and the external inputs $i(t)$.*

It is common practice to model an inverter in network studies with continuous dynamics since the switching frequencies of inverter are typically at very high (2-20 kHz) compared to the network frequency of 50 Hz [115]. With these assumptions we can get the following set of equations for the dynamics of a grid-forming component

$$\begin{aligned}\dot{u} &= f^u(\mathbf{x}, u, u^*, i, i^*) , \\ \dot{\mathbf{x}} &= f^x(\mathbf{x}, u, u^*, i, i^*) .\end{aligned}\tag{5.1}$$

Assumption 5.4 (Symmetry). *The dynamics of the grid-forming components is homogeneous with respect to the phase angles θ .*

Mathematically, this means that the right-hand side (RHS) functions in (5.1) transform as

$$\begin{aligned}f^u(\mathbf{x}, e^{j\theta}u, e^{-j\theta}u^*, e^{j\theta}i, e^{-j\theta}i^*) &= e^{j\theta}f^u(\mathbf{x}, u, u^*, i, i^*) , \\ f^x(\mathbf{x}, e^{j\theta}u, e^{-j\theta}u^*, e^{j\theta}i, e^{-j\theta}i^*) &= f^x(\mathbf{x}, u, u^*, i, i^*) .\end{aligned}\tag{5.2}$$

In the steady operating state, where $u(t)$ is sinusoidal phasor with a constant amplitude, this symmetry is obviously fulfilled. However, this may not necessarily be the case for the transient dynamics of the system. For higher order machine models, such as the fourth-order model (2.12) the dynamics in the d and q -axis might differ, which is typically the case for salient rotor machines. However, for grid-forming inverters there is no reason to design a control that artificially breaks the symmetry between the different phases and consequently, the relevant control schemes discussed in the literature fulfill Assumption 5.4.

5.3.2 Normal Form Derivation

For the derivation of the normal form, we will change coordinates to quadratic invariants of the symmetry (5.2). For this we choose the following set of physical meaningful quantities

$$\begin{aligned} p &= \frac{1}{2}(ui^* + u^*i) , \\ q &= \frac{1}{2j}(ui^* - u^*i) , \\ v^2 &= uu^* , \end{aligned}$$

which are the active and reactive power as well as the squared voltage amplitude. With these, the dynamics (5.1) can be written as

$$\begin{aligned} \dot{u} &= \tilde{f}^u(\mathbf{x}, u, v^2, p, q) , \\ \dot{\mathbf{x}} &= \tilde{f}^x(\mathbf{x}, u, v^2, p, q) . \end{aligned}$$

The explicit transformation is given in the appendix of [68]. We see that u is the only variable left that still depends on the phase angle and therefore, it follows from the symmetry (5.4) that the dependency from u has to take the form

$$\begin{aligned} \dot{u} &= u \cdot g^u(\mathbf{x}, v^2, p, q) , \\ \dot{\mathbf{x}} &= g^x(\mathbf{x}, v^2, p, q) . \end{aligned} \tag{5.3}$$

In the operating state, active and reactive power as well as the voltage amplitude are determined by the solutions of the AC power flow equation (2.9) p° , q° and v° . The state \mathbf{x}° of the internal variable is determined by an initialization process [84]. The deviations of the invariants from the operating state are given by

$$\begin{aligned} \delta p + j\delta q &= uj^* - (p^\circ + jq^\circ) , \\ \delta v^2 &= uu^* - (v^\circ)^2 , \\ \delta \mathbf{x} &= \mathbf{x} - \mathbf{x}^\circ . \end{aligned}$$

In order to simplify the notation, we can introduce a vector of invariants as $\mathbf{y}(t) := (\mathbf{x}^T(t), v^2(t), p(t), q(t))^T$. Assuming that the dynamical transients of the system will not deviate too far from the operational state, we can expand (5.3) up to linear order

$$\begin{aligned} \frac{\dot{u}}{u} &= g^u(\mathbf{y}^\circ) + (\delta \mathbf{y} \cdot \nabla) g^u(\mathbf{y}^\circ) + \mathcal{O}(\|\delta \mathbf{y}\|^2) , \\ \delta \dot{\mathbf{x}} &= g^x(\mathbf{y}^\circ) + (\delta \mathbf{y} \cdot \nabla) g^x(\mathbf{y}^\circ) + \mathcal{O}(\|\delta \mathbf{y}\|^2) . \end{aligned}$$

The left-hand side (LHS) of the voltage equation can be separated into real and imaginary part as

$$\frac{\dot{u}}{u} = \frac{\dot{v}}{v} + j\dot{\theta}.$$

Introducing the constant coefficients $A^{u,x}$, $B^{u,x}$, $C^{u,x}$, $G^{u,x}$, $H^{u,x}$ finally yields the normal form model

$$\begin{aligned} \frac{\dot{u}}{u} &= A^u + B^u \delta \mathbf{x} + C^u \delta v^2 + G^u \delta p + H^u \delta q, \\ \delta \dot{\mathbf{x}} &= A^x + B^x \delta \mathbf{x} + C^x \delta v^2 + G^x \delta p + H^x \delta q. \end{aligned} \quad (5.4)$$

With the assumption that the operating state is a steady state ($\dot{\mathbf{x}} = 0$), we can generally assume that $A^x = 0$. In the co-rotating reference frame where $\dot{\theta} = 0$ we further have $\Im(A^u) = 0$.

The dynamics of any grid-forming actor that fulfils the assumptions in the previous section can be described by this model, as long as the system is sufficiently close to the operating state. It should be mentioned that although we expanded the system dynamics to linear order in the invariant coordinates, it is nonlinear in terms of the complex voltage and current. Instead of a linearized power flow approximation it rather preserves the essential nonlinearities of the dynamical system.

The exact dynamics of a grid-forming component is determined by the parameters. Due to the generality of the normal form, the number of parameters is actually quite large: A^u , B^u , C^u , G^u , H^u are complex coefficients and $B^{u,x}$, C^x , G^x , H^x are matrices with N independent entries each. In fact, for most component models the majority of parameters in normal form representation will be zero. By determining which parameters are non-zero we can identify and distinguish certain classes of models that behave similarly or differently.

5.3.3 Relation to other Oscillator Models

In complex system science there exist several fundamental oscillator models that are frequently used to study general properties of synchronization processes in networked systems [12]. In this section I will show that these models are in fact special cases of the normal form (5.4).

Kuramoto Model For pure phase oscillators the amplitude is constant $v_i = V_i$ and therefore the dynamics is given by $\frac{\dot{u}_i}{u_i} = j\dot{\theta}_i$. Further, there are no internal state variables $\mathbf{x}(t)$ and hence, the remaining equation of the normal form reads as

$$\frac{\dot{u}_i}{u_i} = A_i^u + G_i^u \delta p_i + H_i^u \delta q_i.$$

In the co-rotating frame of the synchronous frequency we have $A_i^u = 0$. Further, we can assume that the dynamics of single oscillators is coupled only by active power ($H_i^u = 0$) in a purely inductive network. Inserting the AC power flow

equations (2.9) and setting $G_i^u = -jD_i^{-1}$ yields the Kuramoto model with heterogenous coupling

$$\dot{\theta}_i = \omega_i - \sum_j K_{ij} \sin(\theta_i - \theta_j) ,$$

where $\omega_i = \frac{p_i^\circ}{D_i}$ is the eigenfrequency of oscillator i and $K_{ij} = \frac{V_i V_j B_{ij}}{D_i}$ is the coupling strength to oscillator j . In Section 2.2.4 I have shown that this model describes the dynamics of simple droop controlled inverters in a purely inductive microgrids [122].

Inertial Kuramoto Model Phase-frequency oscillators also have a constant amplitude $v_i = V_i$, but the frequency $\omega_i(t)$ is an additional internal state variable. The normal form representation reads as

$$\begin{aligned} \frac{\dot{u}_i}{u_i} &= A_i^u + j\delta\omega_i , \\ \delta\dot{\omega} &= B_i^\omega \delta\omega + G_i^\omega \delta p_i + H_i^\omega \delta q_i . \end{aligned}$$

In the co-rotating frame of the synchronous frequency we have $A_i^u = 0$. Again, we can assume that the dynamics of single oscillators is coupled only by active power ($H_i^u = 0$) in a purely inductive network. Inserting the AC power flow equations (2.9) and setting $B_i^\omega = -\frac{D_i}{M_i}$, $G_i^u = -M_i^{-1}$ yields the Kuramoto model with inertia and heterogenous coupling

$$\begin{aligned} \dot{\theta}_i &= \delta\omega_i , \\ M_i \delta\dot{\omega}_i &= p_i^\circ - D_i \delta\omega_i - \sum_j K_{ij} \sin(\theta_i - \theta_j) . \end{aligned}$$

Here, I defined the coupling strength as $K_{ij} = V_i V_j B_{ij}$. The Kuramoto model with inertia is mathematically equivalent to a system of swing equations coupled by a purely inductive network [46]. In Section 2.2.4 I have shown that an AC microgrid with droop controlled inverters and virtual inertia can be described by this model [113].

Stuart-Landau Model For phase-amplitude oscillators without any internal state variable, the normal form representation is given by

$$\frac{\dot{u}}{u} = A^u + C^u \delta v^2 + G^u \delta p + H^u \delta q . \quad (5.5)$$

For $A^u = 1 + j\omega_i$ and $C^u = 1$ we get the dynamics of the Stuart-Landau model [3, 121, 79]. It should be mentioned though, that the coupling of the oscillators that is represented by δp , δq is multiplicative, whereas in most studies on phase-amplitude oscillators the coupling is chosen to be diffusive.

With the additional assumption that the phase dynamics is coupled by the active power ($G^u \in j\mathbb{R}$) and that voltage dynamics is coupled by reactive power ($H^u \in \mathbb{R}$), (5.5) describes the dynamics of a virtual oscillator control (VOC), which is an alternative control scheme for grid-forming inverters [61, 60, 119].

5.3.4 Normal Form of a Droop Controlled Inverter

In Section 2.2.4 I derived the following model for a droop controlled VSI with virtual inertia

$$\begin{aligned}\dot{\delta} &= \omega - \omega_d, \\ \tau_p \dot{\omega} &= \omega_d - \omega + K_p(P_d - p), \\ \tau_p \dot{v} &= V_d - v + K_q(Q_d - q).\end{aligned}\tag{5.6}$$

The equations for phase δ and frequency ω are equivalent to the swing equation and can directly be represented in the normal form (5.4) as described in the previous section. For the amplitude dynamics we have

$$\begin{aligned}\Re\left(\frac{\dot{u}}{u}\right) &= \frac{\dot{v}}{v} = \frac{1}{\tau_p v} [V_d - v + K_q(Q_d - q)] \\ &= \frac{V_d}{\tau_p v} - \frac{1}{\tau_p} - \frac{K_q}{\tau_p v} (Q_d - q).\end{aligned}$$

Expanding this equation in the invariants $v^2(t)$ and $q(t)$ at around $(v^\circ)^2 = V_d^2$ and $q^\circ = Q_d$ yields

$$\frac{\dot{v}}{v} \approx -\frac{1}{2\tau_p V_d^2} \delta v^2 - \frac{K_q}{\tau_p V_d} \delta q,$$

and hence, we get the following normal form parameters for the amplitude dynamics

$$C^u = -\frac{1}{2\tau_p V_d^2}, \quad H^u = \frac{K_q}{\tau_p V_d}.$$

An overview of all normal form parameters for the inverter model (5.6) are shown in Table 5.1. Figure 5.3 depicts a comparison of the voltage amplitude, voltage angle and frequency trajectories for the full model and the normal form approximation.

	A	B	C	G	H
u	$j\omega_d$	j	$-(2\tau_p V_d^2)^{-1}$	0	$-(\tau_p V_d)^{-1} K_q$
ω	0	$-\tau_p^{-1}$	0	$-\tau_p^{-1} K_p$	0

Table 5.1: Normal form parameters of a droop controlled inverter with virtual inertia. In the co-rotating frame $A^u = 0$.

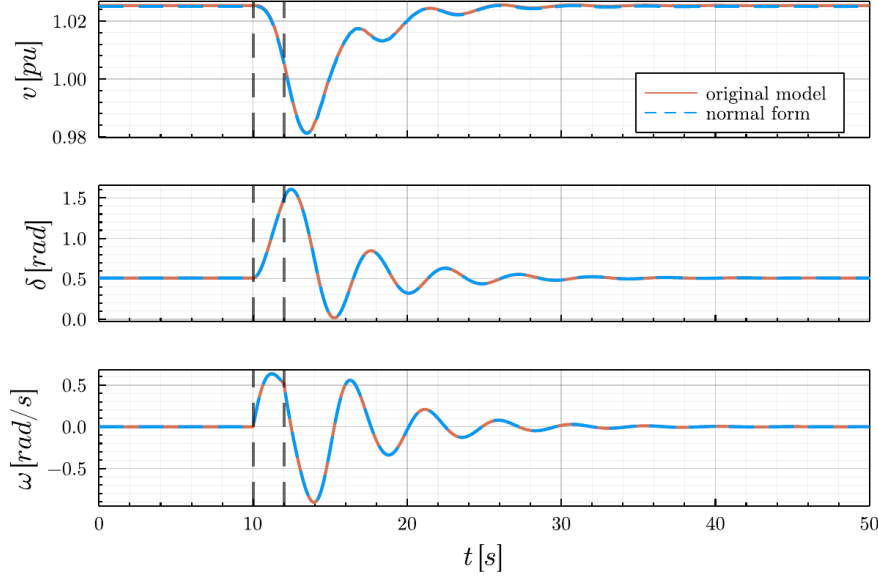


Figure 5.3: Transient of a droop controlled inverter and its normal form approximation. The inverter is connected to a slack node. In the time frame between the vertical dashed line the power setpoint of the inverter is changed to a much smaller value.⁴

5.4 Data-Driven Normal Form Modeling

In the previous section, I exemplarily derived the normal form representation of a droop-controlled voltage source inverter (VSI). However, in practical applications the exact parametrization or even the details of the control loops might be unknown, e.g. for commercial inverter systems. In that case, the dynamical properties can only be obtained through measurements.

In this section I will show that the normal form is in fact very well suited for a grey box modeling approach, by determining model parameters through data. I demonstrate this by using tools of scientific machine learning to fit the normal form model to measurement data of the Tecnalia VSI that was introduced in Section 5.2.1.

5.4.1 Inverter Measurements

The test system setup for the measurements slightly differs from the microgrid test case in Section 5.2. Now, I consider only a single inverter in grid-forming mode. Instead of a grid connection, the system is now connected an AC power source. The source behaves like a slack bus as long as the power output is

⁴The implementation can be found at: <https://zenodo.org/record/4881898>

positive. The power consumption of the load is chosen large enough such that this is always guaranteed. The advantage of the power source is that it provides a power supply for the test system at a much lower noise level than the grid connection. Additionally, it is possible to directly control the voltage level and the frequency of this AC source. The setup is depicted in Figure 5.4.

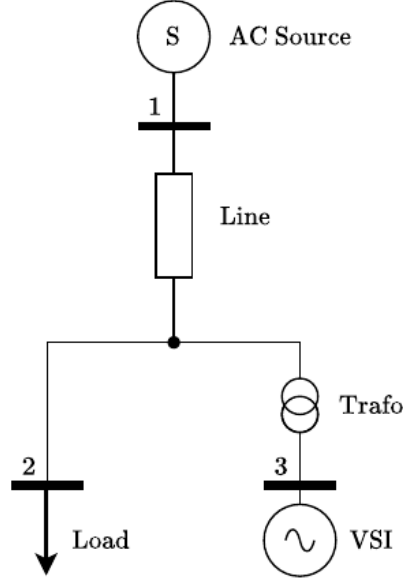


Figure 5.4: Laboratory setup for measuring VSI dynamics. The AC power source at bus 1 is controlled such that it provides a constant AC voltage signal at a certain voltage level and frequency. The line is emulated by a series of resistances and impedances. Details on the parametrization can be found in the technical report [136]. Measurements of voltage and current are taken at bus 3.

I consider a test scenario, where the frequency at the power source is stepped down and back up again several times with ramps of decreasing slope. Measurements are taken directly at the inverter terminal. I calculate the complex current and power in the co-rotating frame of the initial frequency $\omega_s = 2\pi \cdot 50$ Hz as described in Section 2.1.1. As long as the frequency is equal to ω_s the voltage and current signals will be constant. When the frequency is stepped down the signals will start to oscillate. The measured signals for complex current and voltage as well as the calculated active power are depicted in Figure 5.5.

As explained earlier, grid-forming inverters are in a so-called voltage control mode (VCM), which means that the complex voltage is a internal state variable

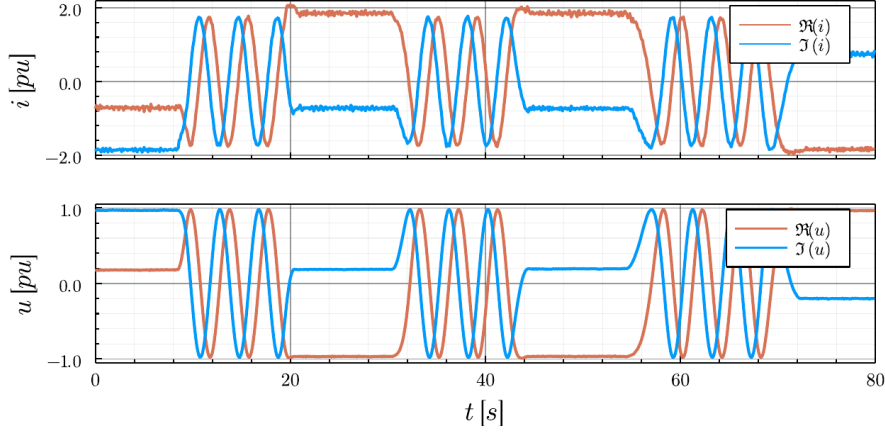


Figure 5.5: Measured time series for complex current and voltage at the grid-forming inverter in the Tecnalia laboratory. The oscillations correspond to shifts in the frequency of the power source. (See Figure 5.4.) The base voltage is $V_{base} = 4$ kV and the base power is $S_{base} = 10$ kW.

wheres the complex current is an external input variable. Consequently, we can consider the inverter in our test system as a black box input-output-system with the complex current signal as the input data and the complex voltage signal as the output data. In the subsequent section, it will be explained how the normal form model (5.4) can be fitted to this data by using machine learning methods.

5.4.2 Model Fitting

I assume that the inverter provides some kind of virtual inertia and choose a normal form model with a single internal variable, the frequency ω . This yields a third order model which reads as

$$\begin{aligned} \frac{\dot{u}}{u} &= A^u + B^u \delta\omega + C^u \delta v^2 + G^u \delta p + H^u \delta q, \\ \delta\dot{\omega} &= A^\omega + B^\omega \delta\omega + C^\omega \delta v^2 + G^\omega \delta p + H^\omega \delta q. \end{aligned} \quad (5.7)$$

For Tecnalia inverter we know that it contains additional dynamic filters and thus, it actually has a higher order dynamics. However, we will see that the third order normal form is good enough to sufficiently capture the measured dynamic behavior.

For the fitting of the normal for model to the measurement data I use a two-step procedure: First, a linear regression is performed to obtain a rough parameter estimate. In the second step, a fine-tuning of the parameters is achieved by using more sophisticated scientific machine learning tools.

For the linear regression, I first calculate the invariant quantities active power $p(t)$, reactive power $q(t)$, and the squared voltage amplitude from the

measured current and voltage signals. The frequency ω can be obtained by a numerical differentiation of the voltage phase angle. The measurements have a temporal resolution of $\Delta t = 1$ ms and a length of $T \sim 80$ s so that each measured signal consist of $T/\Delta t \sim 80,000$ data points. For each time step the LHS and RHS of equation (5.7) have to be equal. The differentials on the LHS of the equation can again be determined by numeric differentiation. We can separate the complex voltage equation into its real and imaginary parts and get the linear matrix equation

$$\begin{bmatrix} \Re\left(\frac{\dot{u}(0)}{u(0)}\right) & \dots & \Re\left(\frac{\dot{u}(T)}{u(T)}\right) \\ \Im\left(\frac{\dot{u}(0)}{u(0)}\right) & \dots & \Im\left(\frac{\dot{u}(T)}{u(T)}\right) \\ \delta\dot{\omega}(0) & \dots & \delta\dot{\omega}(T) \end{bmatrix} = \begin{bmatrix} \Re(A^u) & \Re(B^u) & \Re(C^u) & \Re(G^u) & \Re(H^u) \\ \Im(A^u) & \Im(B^u) & \Im(C^u) & \Im(G^u) & \Im(H^u) \\ A^\omega & B^\omega & C^\omega & G^\omega & H^\omega \end{bmatrix} \begin{bmatrix} 1 & \dots & 1 \\ \delta\omega(0) & \dots & \delta\omega(T) \\ \delta v^2(0) & \dots & \delta v^2(T) \\ \delta p(0) & \dots & \delta p(T) \\ \delta q(0) & \dots & \delta q(T) \end{bmatrix}$$

I solve this equation for the parameter matrix by using Julia's [23] backslash operator⁵ that gives a minimum-norm least squares solution computed by a pivoted QR factorization and a rank estimate of based on the R factor.

For the parameter fine tuning I make use of Julia's differentiable programming capabilities that allow to compute gradients of differential equation solutions with respect to the equation parameters. The normal form model (5.7) is numerically integrated with Tsitouras' 5th order (`Tsit5`) method [132] using the `DifferentialEquations.jl` package [105]. Here, the current signal is interpolated with linear splines to get a continuous input function. I define a loss function that quantifies the distance between the simulation model and the measurements as

$$\begin{aligned} \text{Loss} = \sum_i & w_r |\Re(\Delta u(t_i))|^\eta + w_i |\Im(\Delta u(t_i))|^\eta \\ & + w_\omega |\Delta\omega(t_i)|^\eta + w_v |\Delta v(t_i)|^\eta. \end{aligned}$$

Here, the Δ denotes the difference between measured and simulated quantities and w, η are tuning parameters. The loss function is minimized in a stochastic gradient descent using the `DiffEqFlux.jl` [104] package and the the `ADAM` solver [64]. I tried different tuning parameters for the loss function and finally chose $\eta = 1$, $w_\omega = w_r = w_i = 1$ and $w_v = 10$ which yield a visually good fit of the model to the measured data. The results are depicted in Figure 5.6, that shows the fit to measurement data and a validation with data of a different test run. The fitted parameters are given in Table 5.2.

⁵<https://docs.julialang.org/en/v1/stdlib/LinearAlgebra/>

	A	B	C	G	H
u_{\Re}	3.97	-0.01	-4.42	-0.17	0.01
u_{\Im}	-0.10	0.88	-0.42	-0.36	0.53
ω	1.00	-0.96	-5.46	-3.08	4.73

Table 5.2: Fitted parameters for the normal form representation of the Tecnalia inverter.

5.5 Outlook: Further Normal Form Applications

I have shown that this normal form model is capable of capturing dynamic behavior of a single realistic grid-forming inverter. However, the approach is based on rather general assumptions and it might also be used to model the dynamics at a bus with several dynamic components or even an entire sub-grid that is dominated by grid-forming actors.

In [54] the concept of probabilistic behavioral tuning was introduced. The basic idea is to define a distance measure between the dynamics of a complex system and those of a much simpler specification. It has been shown that this theoretical concept can, with the help of Julia’s scientific machine learning tools, be used to tune the control of distributed generating units such that the collective dynamics fulfills some specification [33]. This approach might also be used to apply it to a sub-grid of components that can be represented by the normal form to tune them to behave like a single normal form actor. Such an aggregation control concept could potentially be helpful to reduce the complexity in grids with a very high number of generation units and distributed control schemes, i.e. in the context of cellular microgrids.

Instead of modeling the dynamics of individual inverters or even entire sub-grids, it would also be conceivable to use the normal form on a much smaller scale, i.e. for modeling sub-components of inverter controls. In Section 2.2.4 we assumed that there is a time scale separation between the inner and outer control loop of a grid-forming inverters and that the inner loop can therefore be modeled by only a simple first-order filter. However, when the dynamics on much higher faster timescales is needed, e.g. for EMT models, this would also require a much more detailed dynamical model of the inner control loop. For a commercial VSIs, it can be assumed that there is even less information on the detailed setup and parametrization given and therefore this would be another perfect application for the data-driven normal form approach. Alternatively, the normal form could in this context also be a good starting point for applying model reduction techniques and to derive a hierarchy of dynamic inverter models with different modeling detail.

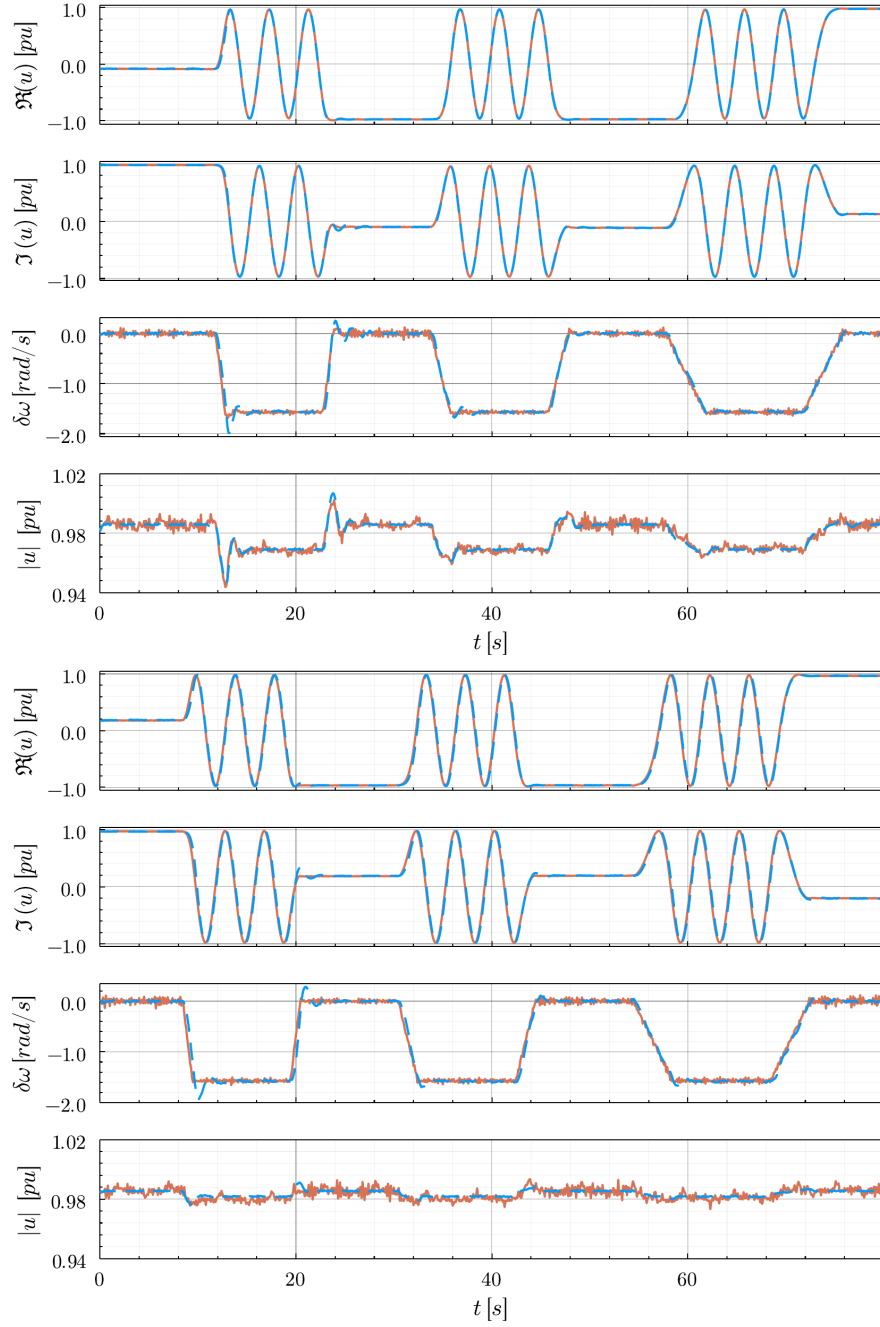


Figure 5.6: Fitting and validation of the normal form model (5.7.) The upper plot shows the fit of the model (blue) to the measured data (orange) of the Tecnalia inverter. The lower plot depicts a validation of the model with the fitted parameters for the measured data of a different test run.

Chapter 6

Hurricane-Induced Cascades of Line Failures

In the previous chapters, I analyzed the challenges of maintaining a stable operation of power grids with regard to an increasing share of renewable power generation. In this chapter, I will shift the focus towards an analysis of the resilience of power grids against extreme weather events.

Electrical grids are considered to be critical infrastructure as many other sectors such as industry, the health system or food supply heavily rely on it. The importance of the electricity sector is even further increasing as other sectors, such as mobility and heating, are becoming more and more dependent on electricity. Extreme weather events are one of the biggest threats to this infrastructure. In the U.S., weather-related events account for almost 45 % of large-scale outages with at least 50,000 customers affected [56]. Moreover, as the climate crisis progresses extreme weather events are expected to become both more frequent and more intense [45].

The causes of extreme weather-related grid incidents are manifold and sometimes difficult to foresee. For example, in July 2021 there was a system split between the Iberian Peninsula and the rest of the continental European grid. The presumed cause of this incident was a forest fire during a heatwave that affected two transmission lines. The smoke and a large concentration of thin particles reduced the insulating capacity which caused short circuit failures and eventually a tripping of the lines [43]. Another extreme weather-related incident occurred in February of the same year when severe winter storms in Texas forced the transmission grid operators to shut down parts of the grid to prevent a complete failure. All types of power plants were impacted by the winter storms and failed to operate at their expected electricity generation output levels. The major reason was, however, that natural gas production, storage, and distribution facilities failed to provide the full amount of fuel demanded by natural gas power plants due to a direct freezing of natural gas equipment [63].

From these examples it is evident that the prediction and modeling of such events is an extremely difficult task that requires a transdisciplinary approach, combining both meteorological models and models of the complex power grid infrastructure. As an exemplary study case for such an approach, we develop a model for analyzing the risk of wind-induced power outages to study the impact of hurricanes on the power grid infrastructure in the southeast US. The major reason for selecting this study case is the availability of models and data for tropical cyclones as well as synthetic test cases of the electricity grids in the affected areas. Another reason is that there are indeed regular and sometimes widespread power outages during major hurricane events which are fairly well documented. Usually, these outages are caused by damages to the transmission infrastructure, i.e. transmission towers and lines. The outage of certain transmission lines can cause overloads in other lines, potentially leading to a cascade of failures. Hence, there is a risk of large-scale blackouts even in regions that have not been directly affected by the respective hurricane.

The model for wind-induced cascading failures presented in this chapter has been developed in collaboration with Julian Stürmer and Mehrnaz Anvari. The simulations were carried out by Julian Stürmer as part of his Master thesis which I co-supervised [126]. All hurricane wind field data has been generated and provided by Thomas Vogt from the *Event-Based Impact Modeling* group at the Potsdam Institute for Climate Impact Research. Results of this project have been previously published in [127, 128].

6.1 Hurricanes & Transmission System Resilience

U.S. states on the Atlantic coastline are almost annually affected by the landfall of tropical cyclones. Figure 6.1 depicts the tracks of a number of notable tropical cyclones that made landfall in Texas and its neighboring states. Corresponding information on these tropical cyclones is gathered in Table 6.1. When a tropical cyclone has a maximum sustained wind speed of at least 33 m/s, it is classified as a hurricane [88]. Below this threshold they are classified as tropical storms. Hurricanes can reach sustained wind speeds of more than 70 m/s [88]. Such extremely high wind speeds are capable of significantly damaging the power transmission infrastructure. These damages include the breaking of transmission line cables, short circuits through contacts of trees, or even the destruction of the transmission towers that carry the lines. Generally, power grids are operated according to the $N - 1$ criterion, i.e. the outage of a single grid component must not cause a violation of security limits in any other component. However, strong hurricane events will typically cause damages of several lines and may thereby cause overloads in other lines that will eventually trigger a cascade of line failures leading to large scale outages. Accordingly, hurricanes and extreme wind conditions have been identified as one of the most significant factors for power outages [102].

Name	Year	Category	v_m [m/s]	N^{out} [10^6]	Report
Claudette	2003	1	40.07	0.074	[22]
Erin	2007	TS	22.36	0.020	[65]
Ike	2008	2	48.91	3.200	[21]
Hermine	2010	TS	29.95	0.230	[16]
Harvey	2017	4	51.05	1.670	[27]
Hanna	2020	1	37.01	0.200	[30]
Laura	2020	4	55.65	0.139	[96]

Table 6.1: Information on past hurricanes in Texas. The category indicates the hurricane intensity at landfall according to the Saffir-Simpson hurricane scale ("TS" stands for tropical storm). The parameter v_m is the maximum 10-minute sustained wind speed. The data is obtained from the simulations described in Section 6.2.2. N^{out} is the reported number of customers left without power supply. This data is gathered from news reports (see [126]).

6.2 Model for Wind-Induced Cascading Failures

In this section, I will introduce a model for wind-induced cascading failures. The wind fields are generated by using historical hurricane tracks and a hurricane pressure-wind field model. Wind-induced transmission line damages are modeled by a stochastic line fragility model. These line damages can trigger cascades of branch overload failures that potentially cause large-scale blackouts in the grid. For this, I introduce a cascading failure model that comprises the DC power flow equations, a model for branch flow overloads, and a mechanism for active power balance control. The combined model is applied to a synthetic test case resembling the Texas power grid.

6.2.1 Texas Synthetic Grid Model

In principle, several states in the southeast of the U.S. are affected by hurricanes. While the electrical grids in most of these states are part of the so-called Eastern Interconnection, the Texas Interconnection which covers most of the Texas state area is practically isolated [75]. It is therefore an ideal test case for investigating the impact of hurricanes on the power grid infrastructure without the necessity to model a large power system of continental scale.

As there is no publicly available data for the Texas Interconnection, we use a synthetic test case provided by the Texas A&M University in the *Electric Grid Test Case Repository* [25]. Despite having a completely synthetic grid topology, this test case resembles some basic properties of the real power system such as the general distribution of generation and demand over the state area.

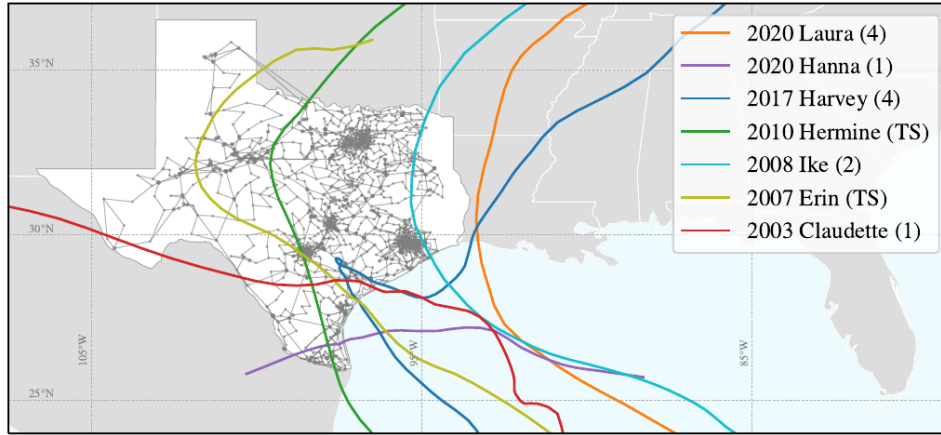


Figure 6.1: Storm tracks of tropical cyclones that passed over Texas. The tracks depict the position of the eye of the respective storm. The data is provided by the International Best Track Archive for Climate Stewardship (IBTrACS) [67, 66]. The legend lists the respective year, the official storm, and the category at landfall. (Here, "TS" stands for tropical cyclone.) The depicted grid is the Texas synthetic grid model described in Section 6.2.1.

In particular, the spatial load distribution is generated from U.S. census data [24].

The test case contains 2000 buses in 1250 substations. Each substation may contain several buses at different voltage levels which are connected by transformers. The test case contains 771 transformers and 2345 transmission lines at the voltage levels 115 kV, 161 kV, 230 kV and 500 kV. The topology of the synthetic grid is depicted in Figure 6.2.

6.2.2 Hurricane Wind Field Model

Besides latitude and longitude coordinates, the International Best Track Archive for Climate Stewardship provides data on meteorological quantities of historical hurricanes such as sustained wind speeds and minimum pressure with a time resolution of 6 h. Given these data sets, it is possible to model the wind field by using a hurricane pressure-wind model. For this we use the software package CLIMADA [17] that utilizes the model introduced in [57]. Here, the generated wind field is the sum of a rotationally symmetric wind field and a translational wind field that accounts for the movement of the tropical cyclone. In the simulations, we use a spatial resolution of 0.1° in longitude and latitude and a temporal resolution of $\tau = 5$ min.

Figure 6.3 depicts an example frame of the calculated wind field for Hurricane Harvey. It can be seen that the wind field can potentially cover a large

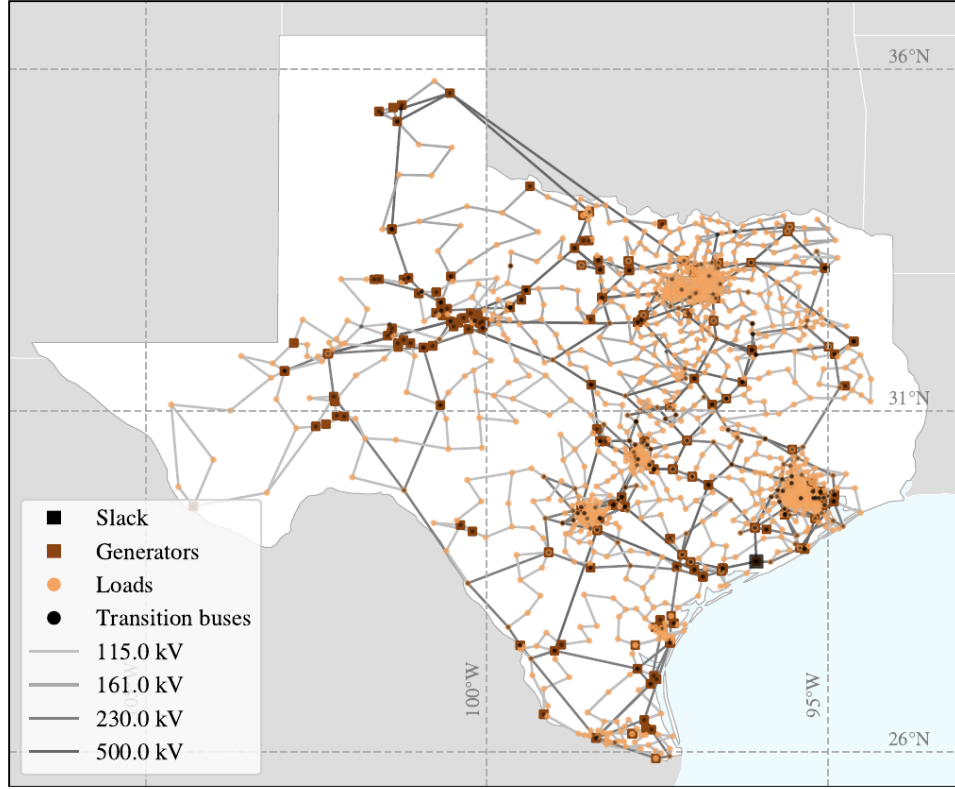


Figure 6.2: 2000-bus synthetic grid on the footprint of Texas. The data set is available at [25].

part of the synthetic grid, albeit the wind speeds are much stronger around the cyclone center. The time of the simulations depends on the specific trajectory and translational speed of the respective hurricane. For hurricane Ike the time span is only 62 h whereas the time span for Hurricane Harvey is over 188 h. With the given time resolution this results in a number of several hundreds up to a few thousand frames for the wind field.

6.2.3 Probabilistic Line Fragility Model

The transmission infrastructure is typically the most critical part of the power system during a hurricane scenario. Overhead transmission lines are carried by transmission towers and thereby divided into a large number of segments. We assume that each of those segments has an equal length of $l \approx 161$ m which corresponds to the average distance between two transmission towers in Texas [139]. Further, we assume that the transmission lines connect the buses in the shortest possible way, i.e. along the geodesic line. With this we can assign a spatial position to each line segment and determine the wind speed that it is

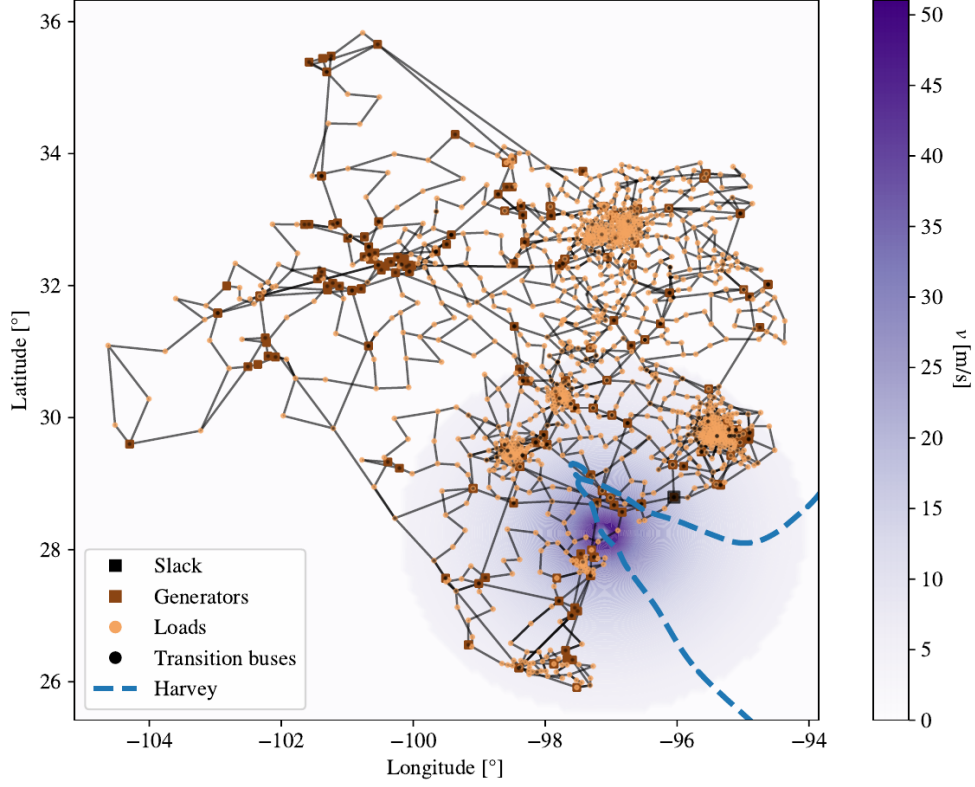


Figure 6.3: Modeled wind field of hurricane Harvey at 6:30 UTC on August 26, 2017 on top of the Texas synthetic grid. The storm track is taken from the IBTrACS data archive [67, 66] and depicted by the dashed line. The wind field at the respective time is modeled with the CLIMADA software package [17] and depicted as a contour plot.

exposed to from the wind field model.

The wind force acting on the wire of a transmission line segment k scales with the square of the wind speed $F_k(v) \propto v^2$ [143]. Motivated by a similar approach introduced in [141] we model the probability that a line segment k fails in the time interval $[t, t + \tau)$ as

$$p_k(v_t) = \min \left(\tau r^{brk} \frac{F_k(v_t)}{F^{brk}}, 1 \right).$$

Here, F^{brk} is a reference breaking force and r^{brk} is a failure rate that is used to calibrate the fragility model to recorded failure data. Unfortunately, there is no publicly available database for the number of destroyed transmission lines. We therefore use information on the number of customers without electricity supply from official reports to estimate the total power outage in terms of the final unsupplied demand in the system. Comparing the simulation results to

this data, we can narrow down the parameter value to the range

$$1 \times 10^{-4} \text{ h}^{-1} < r^{brk} < 5 \times 10^{-3} \text{ h}^{-1} ,$$

for an arbitrarily chosen reference breaking force $F^{brk} = 152.13 \text{ kN}$ [126]. In the simulations, we set the failure rate to $2 \times 10^{-3} \text{ h}^{-1}$ which yields reasonable results.

6.2.4 DC Power Flow Model

In Section 2.1.5 we introduced the AC power flow model. In our attempts to use this as part of our cascading failure algorithm, it turned out that the AC power flow solver tends to run into numerical convergence issues [126]. The main reason for this is that in a severely damaged grid the reactive power balance is no longer guaranteed. In contrast to active power that can be balanced globally, reactive power has to be balanced locally, because of high reactive power losses in the line susceptances. When the reactive power becomes unbalanced this corresponds to a bifurcation where the stable operation point vanishes and a so-called voltage collapse occurs [39]. In real power grids, it is attempted to prevent such under-voltage situations by shedding loads to regain reactive power balance. Eventually, a more detailed model for voltage collapses, load shedding or even both are needed to circumvent convergence issues in a cascading failure model [92].

Instead, we make use of a simplified model, the DC power flow model, which is based on the following additional assumptions:

1. Ohmic losses are neglected, i.e. $G_{ij} = 0$ for all branches.
2. The voltage profile is flat, i.e. $|V_i| = 1 \text{ pu}$ at all buses.
3. Voltage angle differences are small, i.e. $\sin(\theta_{ij}) \approx \theta_{ij}$ for all branches.
4. Reactive power equations are neglected.

Applying these assumptions to the AC power flow equations yields

$$P_i = \sum_j B_{ij}(\theta_i - \theta_j) . \quad (6.1)$$

Since losses are neglected, a slack node is no longer necessary. Further, neglecting reactive power and assuming a fixed voltage magnitude leaves the voltage angle θ to be the only free variable at all buses. The DC power flow equations are solved using `PowerModels.jl` [36] and the IPOPT solver [137]. For more details on the software package see Section A.3 in the appendix.

6.2.5 Line Overload Model

In the DC power flow model, the flow on transmission lines and transformers is given by

$$P_{ij} = B_{ij}(\theta_i - \theta_j) .$$

When the power flow on a branch becomes very large, it will heat up through the Ohmic losses. In real power grids, the power flow on a branch is therefore limited to avoid irreversible damage to the transmission infrastructure. In practice, this is implemented by using circuit breakers that automatically disconnected a branch once its limit is exceeded.

The synthetic test case of Texas includes such limits C_{ij} for all transmission lines and transformers. In the simulation algorithm, an overload failure is implemented by deactivating a branch if

$$P_{ij} > C_{ij} ,$$

at any time step. Overload line failures cause a relocation of power flow in the grid which eventually may lead to a cascade of line failures [38, 101, 112].

6.2.6 Active Power Balance Control Model

A cascade of line failures can cause a system split, i.e. a formation of two or more islands that are disconnected from each other¹. In these islands, there will typically be an imbalance in active power. The mismatch in each island i can be calculated by

$$\Delta P^{[i]} = \sum_{j \in \mathcal{C}_G^{[i]}} P_j + \sum_{j \in \mathcal{C}_L^{[i]}} P_j ,$$

where $\mathcal{C}_G^{[i]}$ and $\mathcal{C}_L^{[i]}$ are the sets of generators and loads in the island. The over- or undersupply of loads leads to either the acceleration or deceleration of generators. When the imbalance in the islands is small enough to be offset by the automatic control systems, they will eventually settle into a new over- or under-frequency equilibrium state. How much a generator is contributing to the primary control reserve depends on the parameter of its droop speed control.

Since there are no dynamic control parameters given for the Texas synthetic test case we assume that they contribute homogenously to the primary reserve. We can then incorporate the control power into the model by changing the dispatch of all generators as

$$P_j \rightarrow P_j - \frac{\Delta P^{[i]}}{|\mathcal{C}_G^{[i]}|} .$$

¹This includes the special case that only a single load or generator is disconnected from the rest of the grid.

However, the adjustment of each generator is limited by their minimum and maximum power capacity. Taking these into account, we iteratively only adjust those generators that have not yet reached their limit.

The case that the power imbalance in an island is larger than the total remaining capacity of all generators is treated as follows:

1. When there is an overproduction even for all generators being set to their minimum capacity, we assume that the island is blacked out completely and consequently all buses and branches are deactivated.
2. When there is an underproduction even for all generators being set to their maximum capacity, we assume a uniform load shedding until the balance is restored. This is done by iteratively adjusting the load demand, similar to the adjustment of the generator dispatches.

6.2.7 Connecting the Sub-Models

The models introduced in the previous sections are connected to a complete model of wind-induced cascading failures. Here, we assume a time scale separation: The time resolution of the wind field model is $\tau = 5$ min whereas cascades of line failures typically happen on the scale of a few seconds. For each wind field frame we therefore simulate cascading failures as long as it takes to reach a new stable grid state before going to the next wind frame. A flow chart of the full model is depicted in Figure 6.4.

Finally, it should be mentioned that since the line fragility model is probabilistic, the full model is as well. This means that it can be used to perform Monte Carlo simulations to estimate probability distributions, e.g. for the total power outage or the number of disconnected and destroyed lines. In the next section it will be shown that even for a very limited number of hurricane tracks, the Monte Carlo simulations yield a large variety of very different scenarios, that facilitate general insights on the resilience of the system.

6.3 Monte Carlo Simulation Results

In this section we will focus on the simulation results for only two historical hurricane tracks, Harvey and Ike, which tend to cause the largest outages in the grid. A detailed analysis of those scenarios can be found in [126].

For every storm track we perform $N_s = 10^4$ simulation runs. As previously mentioned, empirical data on the impact of hurricanes on the electricity grid is typically provided in terms of the number of unsupplied households which can be roughly converted to the total amount of unsupplied demand using U.S. census data [126]. Based on this approach, we quantify the outage size in the simulations by the total amount of unsupplied load at the end of the

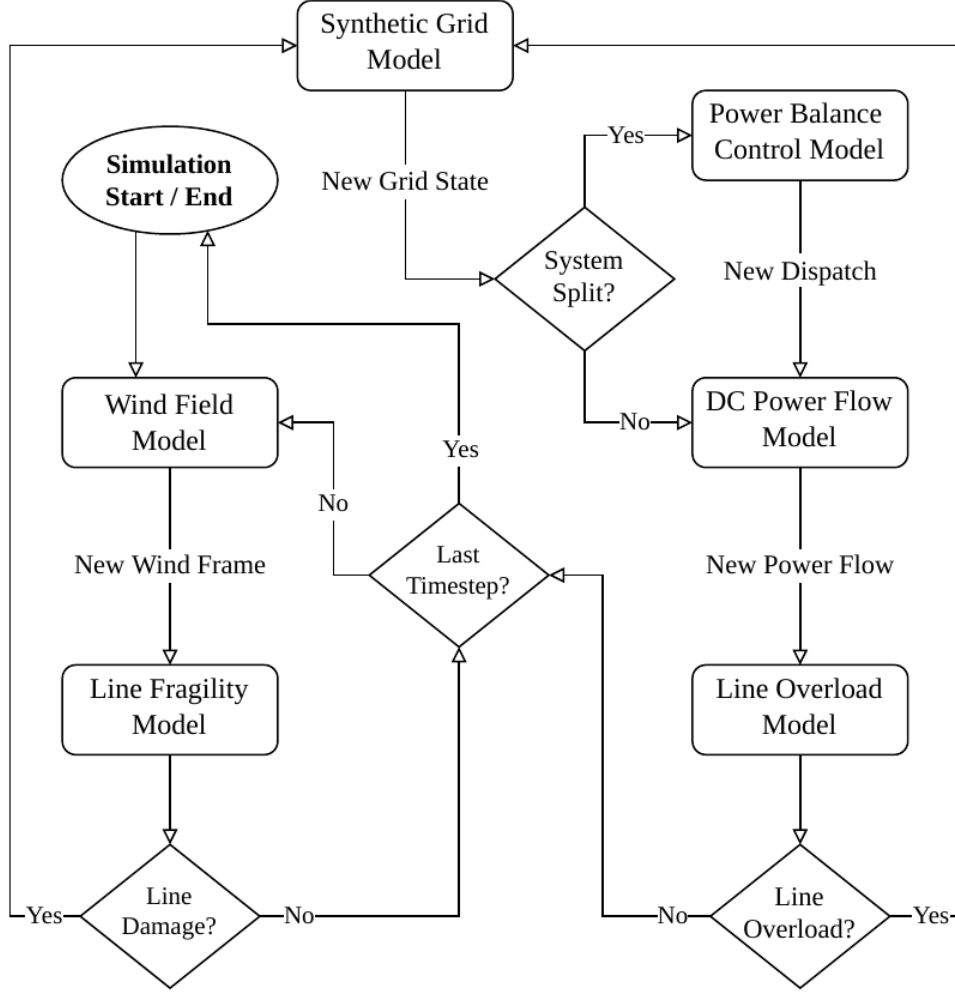


Figure 6.4: Flow Chart for the Hurricane-Induced Cascading Failure Model.

simulation run

$$P^{out} = \sum_{k \in \mathcal{C}_L} [P_k(t_{start}) - P_k(t_{end})] .$$

Additionally to this measure on the overall outage, we also calculate the outage probability of each grid element (buses and branches) to analyse which parts of the system are particularly prone to damage or failure

$$p_e = p(\text{outage of } e) .$$

The expected number of outages of an element e in N_s simulation runs is $\mathbb{E}\{N_e^{out}\} = p_e \cdot N_s$. For a large number of simulation runs ($N_s = 10^4$), the grid element outage probability can thus be estimated as $p_e \approx N_e^{out}/N_s$.

We are interested in identifying those grid elements that are particularly vulnerable and tend to fail even in low-impact scenarios as well as grid element

outages that correlate with the occurrence of large-scale outages. For this purpose, we also calculate the conditional probabilities of element outages, given that the total amount of unsupplied load lies in a certain interval $I \subset \mathbb{R}_+$

$$p_{e,I} = p(\text{outage of } e \mid P^{out} \in I) .$$

Figure 6.5 and 6.6 depict the Monte Carlo simulation results for hurricane Harvey and hurricane Ike. The violin plots depict the probability distribution for the total outage P^{out} , whereas branches and buses in the grid plots are colored according to their conditional outage probability for both small and large outage events. It can clearly be seen, that the eastern parts of the grid over which the hurricanes directly pass tend to be highly affected. However, especially for the Harvey scenario we also see that cascading failures can spread through the entire grid and lead to significant outage probabilities, e.g. in the most western part.

One remarkable observation is that for both hurricanes the probability distribution of the total amount of unsupplied load P^{out} exposes a bi-modal shape. Comparing the conditional outage probabilities of the grid elements for small and large outage events, it can be seen that the major difference is whether the grid area around the city of Houston is still intact or completely blacked out. Similar results have been observed for simulations of the hurricanes Claudette, Hanna, Erin, and Laura [126].

The total amount of load in the affected region around Houston is 17 GW and corresponds to the major share of unsupplied load for most scenarios. In the subsequent section, we will show that the outage of this region is caused by a cascade of failures that can be triggered by the failure or damage of a few particularly critical lines. The outage risk can be significantly reduced by protecting those very lines from wind damage.

6.4 Improving the Resilience of the Texas Grid

In principle, there are at least two strategies to improve resilience against hurricane-induced cascades: One approach would be to increase the capacity of lines to contain the spreading of cascading failures. In practice, this could for example be implemented by adding parallel cables to existing branches. However, in the simulations it becomes apparent that a large number of lines are involved in different cascading scenarios and therefore this strategy does not seem to be very targeted. The second approach would be to better protect individual lines from wind damage, e.g. by improving the stability of transmission towers or by replacing an overhead transmission line with an underground cable. Apart from the fact, that the length of underground cables is generally limited to lengths below 20 km [5], it is certainly a quite cost-intensive measure. Nevertheless, this could be an appropriate strategy as we find that only a small number of lines, primarily located in the Houston

area, tend to trigger large-scale cascading failures. In the previous section it was shown that the difference between small and large outage scenarios is primarily determined by whether the Houston area is blacked out or not. As previously mentioned, this area comprises a total load demand of about 17 GW. Any cascade that causes a complete blackout of this area would therefore result in a change of load supply ΔP^{out} of at least 15 GW, which we choose as an arbitrary threshold for large cascade events.

We define the number of times that in a simulation of hurricane h the exclusive destruction of the line ij causes a cascade that changes the load supply as $\Delta P^{out} > 15$ GW as $N_{ij}^{15\text{GW}}(h)$. With this, we can calculate the probability of such a single line induced large cascade event by

$$p_{ij}^{15\text{GW}}(h) \approx \frac{N_{ij}^{15\text{GW}}(h)}{N_s} .$$

We define a line priority index by averaging this probability over all hurricane scenarios depicted in Figure 6.1 to obtain a measure that is as independent as possible of a specific hurricane track

$$\kappa_{ij} = \frac{1}{|\mathcal{H}|} \sum_{h \in \mathcal{H}} p_{ij}^{15\text{GW}}(h) .$$

In Figure 6.7 it can be seen that 19 of the 20 lines with the highest priority are located within the Houston area. A wind-induced destruction of any of those lines has a high probability to trigger a cascading failure that leads to a complete outage of the Houston area which contains about 17 GW of load demand.

In Figure 6.8 it is shown that for hurricane Harvey the probability of single large cascades has decreased to almost zero, while for hurricane Ike it is significantly reduced. This also affects the probability distribution of the final amount of unsupplied load which reveals a significant shift towards scenarios with $P^{out} < 10$ GW. Thus, the strategy of protecting crucial lines seems to be remarkably effective.

6.5 Outlook: Model Improvement & Economic Analysis

In Section 6.2.4 I already indicated that the cascading failure model could be further improved by using an AC power flow model including reactive power flows and more detailed models of control schemes. This could include modeling phenomena like voltage collapses or under-voltage load shedding. Such an approach would certainly be necessary to obtain quantitatively more realistic results on the outage sizes. Another aspect of our model that could be improved is related to the power dispatch in the grid. In our simulations, we

always used the same demand distribution and the same generator dispatches that come with the synthetic test case. In reality, the demand distribution can drastically vary at different times of the day and between different seasons. The dispatch is regulated by the electricity market and may depend on current fuel prices and weather conditions. Including a variation of load distributions and generator dispatches in the Monte Carlo simulations would yield more robust results on the identification of weak points in the grid.

Besides these possible improvements to the model, our Monte Carlo-based approach opens the opportunity for a more detailed economic analysis for identifying the most suitable and cost-efficient strategies to enhance resilience in the grid. In the previous section, it was shown that protecting a small number of transmission lines can already significantly decrease the risk of large-scale outages. The most effective method of implementing this would be to put the cables underground which is, however, very cost-intensive. In principle, there is a large variety of alternative measures to prevent wind damage and the spreading of cascading failures, e.g. improving the stability of transmission towers or increasing the flow capacity of certain lines by adding extra cables. An adjustment of the synthetic grid model and the line fragility model according to these measures allows comparing the benefit of different investment strategies in the Monte Carlo simulations and could help to identify which measures give the best trade-off between investment costs and enhancement of grid resilience. Such an analysis of optimal investment strategies has already been conducted in the context of earthquake-related power system outages [90, 72].

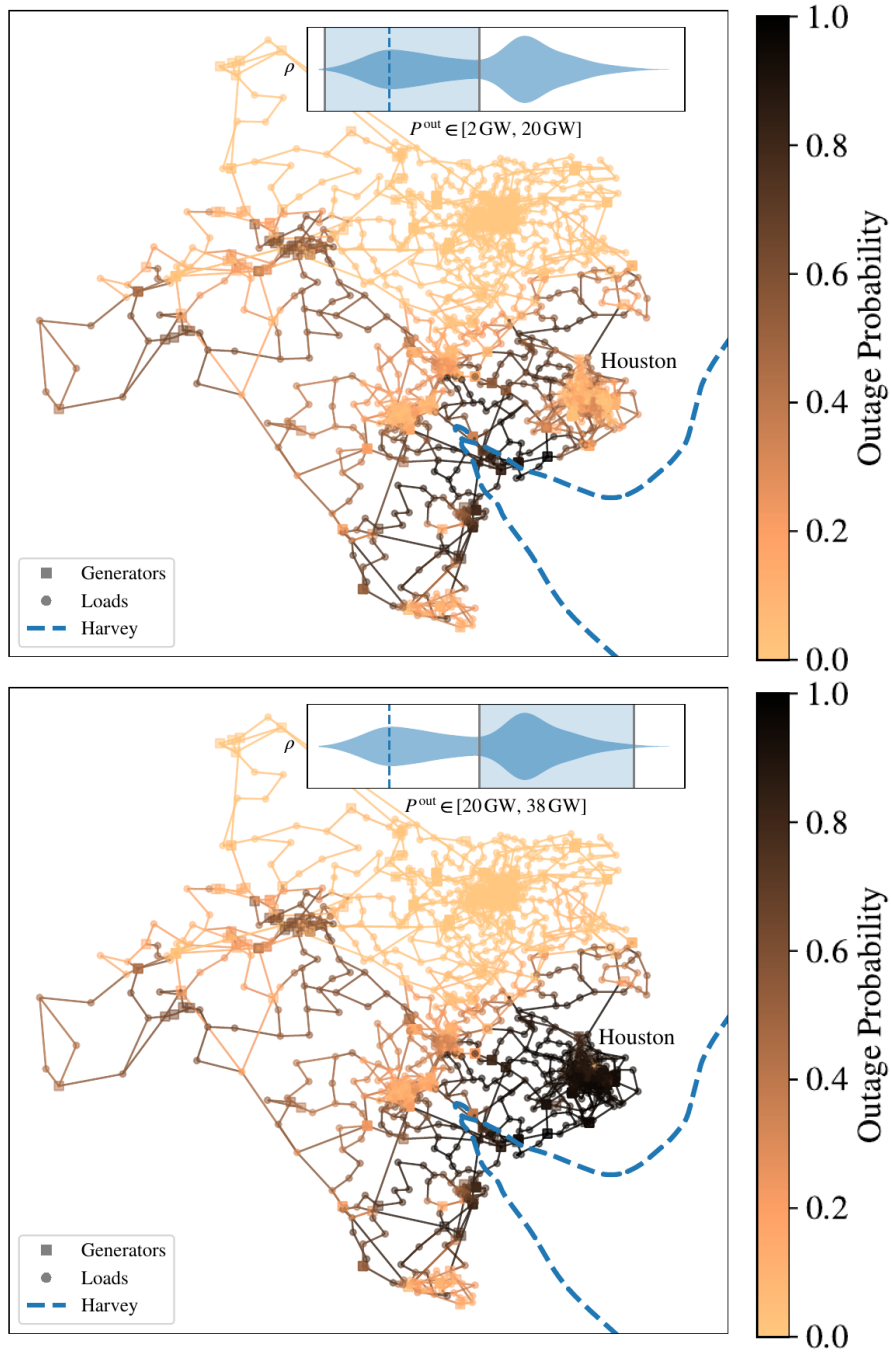


Figure 6.5: Outage probability of grid components for Hurricane Harvey. The violin plots depict the probability distribution for the total outage P^{out} . The upper plot shows the component outage probabilities for a total outage $2 \text{ GW} < P^{\text{out}} < 20 \text{ GW}$ whereas the lower plot shows the component outage probabilities for a total outage $20 \text{ GW} < P^{\text{out}} < 38 \text{ GW}$.

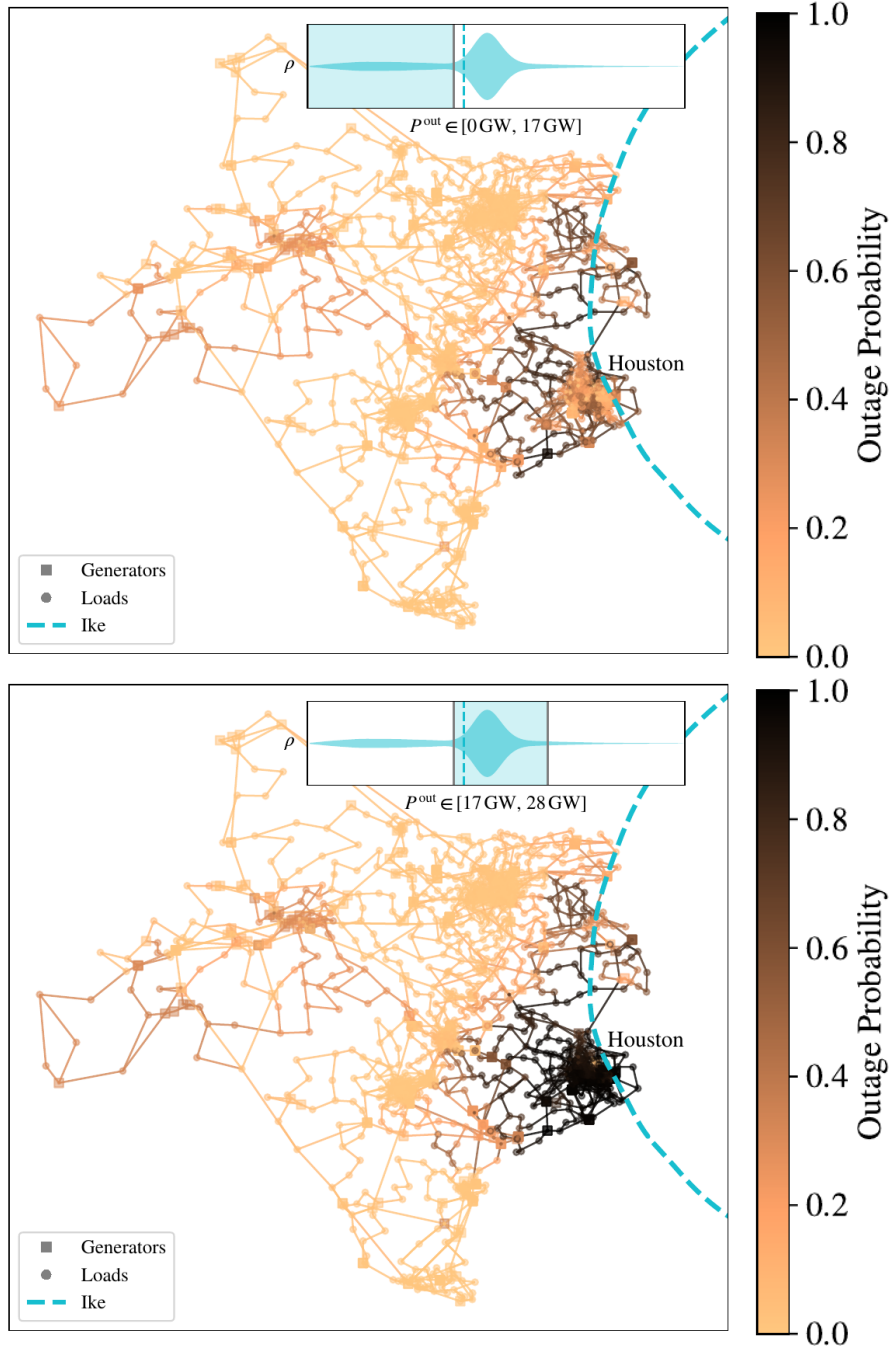


Figure 6.6: Outage probability of grid components for Hurricane Ike. The violin plots depict the probability distribution for the total outage P^{out} . The upper plot shows the component outage probabilities for a total outage $P^{out} < 17 \text{ GW}$ whereas the lower plot shows the component outage probabilities for a total outage $17 \text{ GW} < P^{out} < 28 \text{ GW}$.

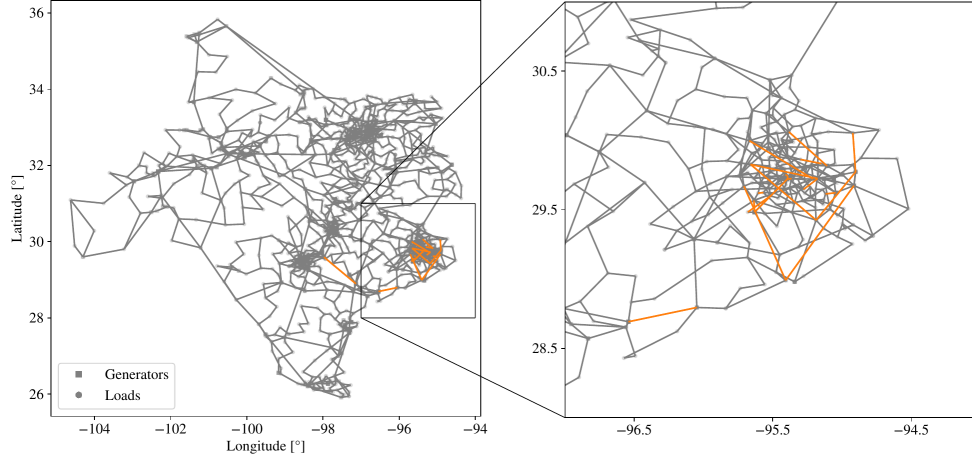


Figure 6.7: 20 most critical lines in terms of the priority index. The majority of those lines (colored in orange) lie in the Houston grid area.

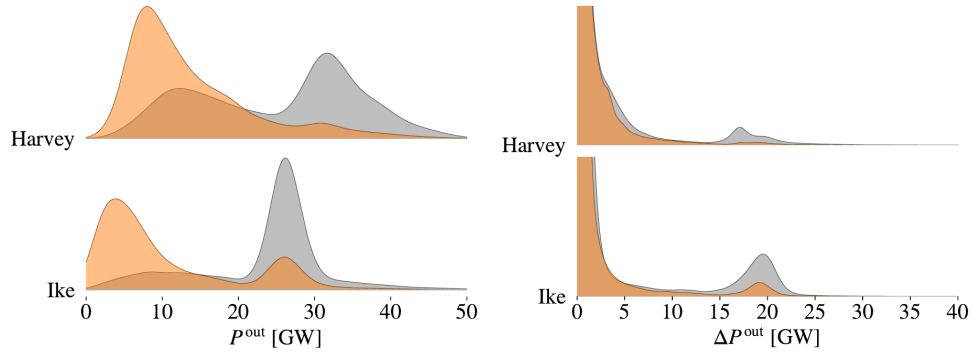


Figure 6.8: Left: Probability distributions of the total power outage P^{out} . The distribution for the default grid is depicted in grey, whereas the distribution of the improved grid (with the 20 most vulnerable lines being protected from wind damage) is depicted in orange. Right: Corresponding probability densities of the cascade sizes in terms of the induced power outage ΔP^{out} .

Chapter 7

Summary & Discussion

In the introduction, I formulated three challenges for maintaining the stability and resilience of future power grids:

1. Wind and solar power production are fluctuating even on the time scale of seconds. Within large wind parks or a solar fields, these fluctuations can be highly correlated and may potentially add up to large fluctuations that are directly fed into the grid.
2. Synchronous generators will get replaced by a very large number of inverter-interfaced generation units, which will at least be partially equipped with a grid-forming control. Due to the lack of a universal model for the large variety of proposed control schemes, it is difficult to make general statements about the collective dynamics in such inverter-dominated grids.
3. As the climate crisis progresses, extreme weather events are becoming more severe and more frequent. In some regions, this may increase the risk of large scale power outages by either imposing conditions where the transmission system is close to its capacity limits or even by a direct damage of certain grid components.

I will now give a brief summary of the results of this thesis and discuss the contributions for addressing the three challenges.

7.1 Renewable Power Fluctuations

In order to analyze the impact of short-term renewable fluctuations, I derived a linear theory for stochastic perturbations of dynamical systems on network structures. It is shown how the network response can be decomposed into the eigenmodes of the system. The susceptibility to external perturbations and the response strength of the network nodes is given by a superposition of left

and right Jacobian eigenvectors respectively. The contribution of each mode to the system response is determined by the overlap of the power spectral density of the perturbation with the eigenfrequencies of the system. For systems with homogenous parameters, the Jacobian eigenvectors can be directly related to the eigenvectors of the Laplacian and thereby to the network structure. While this is typically not the case in real-world systems, the theoretical analysis of this special case gave valuable insights and helped to understand observed phenomena in more complex and realistic systems.

Using the linear response theory and simulations in an AC microgrid, I have shown that for the typical parameter regime of realistic power grids, the response of the resonant eigenmodes is suppressed as the power spectral density of renewable fluctuations is comparatively weak at their eigenfrequencies. As a result, the network response is dominated by a single overdamped eigenmode with a homogeneous response at all network nodes. This bulk mode corresponds to a quasi-static variations of the synchronous grid frequency that are caused by a global imbalance between production and demand in the grid. In sufficiently large grids with wind and solar production at different places such variations can be expected to balance out as wind and solar fluctuations are spatially uncorrelated on the respective timescale over longer distances. However, in smaller grids (e.g. islanded microgrids) with fewer generating units on a smaller spatial scale and no connection to a higher grid level these fluctuations may play a significant role. Moreover, these grids are typically on the MV level and thus the line losses are higher. This is important to consider, as I have shown that line losses cause an amplification of the fluctuations in the opposite direction of the power flow.

Related Publication:

- A. Plietzsch, S. Auer, J. Kurths, and F. Hellmann. Linear response theory for renewable fluctuations in power grids with transmission losses. *arXiv preprint arXiv:1903.09585*, 2021. (In Review at Chaos: An Interdisciplinary Journal of Nonlinear Science)

7.2 Modeling of Grid-Forming Inverters

In Chapter 5, I presented laboratory measurements of grid-forming and grid-following inverters in a small microgrid setup. With a detailed knowledge of the control schemes and parameter settings as well as an appropriate software package, it was possible yet cumbersome to reproduce the measurements with simulations. However, in reality the circumstances are often less ideal than in a laboratory setup. Within the next couple of years, a potentially large number of grid-forming components will be implemented into the power system. It is likely that inverters with very different control laws will be part

of the same grid and interact with each other dynamically. Additionally, the parametrization or even the entire control scheme of individual inverters might be unknown, which makes it very hard to analyze the stability of such systems. Being aware of these potential problems has given the impetus to develop a normal form model for grid-forming components. This model is general as it is only based on fundamental principles such as the inherent symmetry of the operating state. In this thesis, it was shown that this model is not only capable of approximating standard models for grid-forming controllers but can even be used for an entirely data-driven modeling approach without any detailed knowledge about the underlying control laws. The normal form opens up new opportunities to study the stability of inverter-based grids from a more general and abstract point of view. This is complementary to the typical approach in the control system and power system engineering literature, that focus on a very detailed analysis of a particular control scheme.

Related Publications:

- A. Plietzsch, R. Kogler, S. Auer, J. Merino, A. Gil-de Muro, J. Liße, C. Vogel, and F. Hellmann. Powerdynamics.jl—an experimentally validated open-source package for the dynamical analysis of power grids. *SoftwareX*, 17:100861, 2022
- R. Kogler, A. Plietzsch, P. Schultz, and F. Hellmann. Normal form for grid-forming power grid actors. *PRX Energy*, 1(1):013008, 2022
- A. Büttner, H. Würfel, A. Plietzsch, M. Lindner, and F. Hellmann. An open source software stack for tuning the dynamical behavior of complex power systems. In *Proceedings of OSMSES 2022*. IEEE, 2022

7.3 Extreme Weather Events & Grid Resilience

In Chapter 6, I introduced a model for simulation large scale power outages that are caused by hurricane damages of the transmission infrastructure. This turned out to be a good study case for the impact of extreme weather events on electricity infrastructure as both historical hurricane data as well as a realistic grid model of the corresponding region are publicly available. Hurricane wind fields is modeled using a tropical cyclone model and the spreading of outages in the grid by a DC power flow based cascading failure algorithm. The interconnection between the meteorological and the power grid model are wind-induced transmission line damages that are modeled stochastically. Using Monte Carlo simulations, we estimated the outage probability of each element in the grid. We were able to identify several critical lines in the Houston area of the synthetic test case. Moreover, we could show that a better protection of a few of these lines can significantly increase the resilience of

the grid. These strong results suggest that the general approach of combining meteorological models and power grid models can help to identify vulnerabilities in the infrastructure but may even be used to analyze the feasibility of different options to strengthen the systems resilience. As the electricity infrastructure in different parts of the world is facing very distinct meteorological conditions, it is certainly necessary to adjust the model to the conditions of a respective region.

Related Publications:

- J. M. Stürmer, A. Plietzsch, and M. Anvari. The risk of cascading failures in electrical grids triggered by extreme weather events. In *Proceedings of ENERGY 2021*, pages 19–23. IARIA, 2021
- J. M. Stürmer, A. Plietzsch, M. Anvari, T. Vogt, C. Otto, and F. Hellmann. Hurricane-induced failures of critical transmission lines lead to huge power outages in texas, 2022. (In Preparation)

Appendix A

Simulation Software

I will give a brief overview of the software packages that have been used throughout this thesis. Concerning the packages `NetworkDynamics.jl` and `PowerDynamics.jl`, I also contributed to the software development, documentation, maintaining and publication (see [74, 100]).

A.1 `NetworkDynamics.jl`

`NetworkDynamics.jl` is a software package for simulating complex dynamical systems on network structures. The package is developed collaboratively by the *Complex Infrastructure Networks* group at the Potsdam Institute for Climate Impact Research (PIK). The source code and documentation are available on GitHub¹ under an open source license. A detailed description of the current functionalities accompanied by many examples and code snippets has been published in [74].

`NetworkDynamics.jl` is written in Julia, a rather young programming language that is specifically designed for scientific computing purposes [23]. Julia is a dynamically typed language using a just-in-time compiler. Its use is therefore convenient as a scripting language like Python or Matlab, while at the same time the code can be optimized to have a similar performance as C or Fortran. The Julia package `DifferentialEquations.jl`, which comes with state-of-the-art solvers for Stochastic Differential Equations (SDEs), Delay Differential Equations (DDEs), Differential Algebraic Equations (DAEs), as well as functionalities for handling discrete events is arguably one of the best differential equation solver suites available [105]. Moreover, it is compatible with a large variety of Julia’s machine learning packages.

Implementing performant simulations of large complex dynamical systems that eventually include delays, stochasticity or algebraic constraints can be a quite difficult task. The aim of `NetworkDynamics.jl` is to provide a convenient

¹<https://github.com/PIK-ICoNe/NetworkDynamics.jl>

interface for defining local dynamics of individual nodes and edges on a high level of abstraction. It uses custom-build graph data structures in order to construct an optimized, allocation-free Julia function for the whole network system which can then efficiently be solved using `DifferentialEquations.jl`. In benchmark tests with Kuramoto oscillator networks of different sizes, `NetworkDynamics.jl` has been shown to outperform similar software packages such as the Python-based `JiTCode` and even Fortran-based implementations [74].

I have used the package for simulation renewable fluctuations in the IEEE RTS-96 test case in Chapter 4. Further, `NetworkDynamics.jl` is also the basis of the `PowerDynamics.jl` package.

A.2 PowerDynamics.jl

`PowerDynamics.jl` is a software package for dynamical simulations of power grids. The package is jointly developed by the *Complex Infrastructure Networks* group at PIK and the company Elena International GmbH². The source code and documentation available on GitHub³ under an open source license.

`PowerDynamics.jl` is built on top of `NetworkDynamics.jl` with complex current and voltage being predefined variables. The package comes with a library of various component models for generators, loads, inverters, lines and transformers as well as different fault scenarios. Further, it provides utility functions such as calculating the static power flow or steady states of a system as well as a plotting recipe. Some of the models and fault scenarios have been experimentally validated in a microgrid laboratory. An exemplary comparison of measurements and simulations has been presented in Section 5.2. More details on these measurements can be found in the technical report [136]. A detailed description of the software architecture and all functionalities as well as an example simulation in the IEEE 14-bus model has been published in [100].

`PowerDynamics.jl` has shown to be much more performant than commercial competitors such as `PowerFactory` or `Simulink` [73]. Once the system is compiled, repeated simulations of the same setup run extremely fast. The package is therefore particularly suited for sampling-based methods [82, 52].

In its most recent release, `PowerDynamics.jl` comes with the new utility to define blocks of symbolic equations with certain input and output variables and to connect these blocks with each other [33]. Using the `ModelingToolkit.jl` package [77], these block-based system can then be converted into component functions that can be simulated with `NetworkDynamics.jl`. This feature is extremely useful for building models of very detailed inverter controls from basic controllers and filters in order to evaluate the performance and stability of certain control schemes in a dynamic grid simulation.

²<https://www.elena-international.de/>

³<https://github.com/JuliaEnergy/PowerDynamics.jl>

A.3 PowerModels.jl

`PowerModels.jl` is a software package for steady state power network optimization. The package is developed by the *Advanced Network Science Initiative* at the Los Alamos National Laboratory. Source code and documentation are available on GitHub⁴. A detailed description of the software architecture as well as code examples for basic simulations has been published in [36].

`PowerModels.jl` is based on JuMP, a domain-specific modeling language for mathematical optimization embedded in the Julia language. The package is designed for solving different algebraic and optimization problems including AC and DC power flow equations, optimal power flow problems and transmission network extension planning. It provides utilities for parsing data files in industry-standard data formats (Matpower and PSS/E) as well as for modifying the network data which is structured in dictionary that is designed to be mostly consistent with the file format of its commercial competitor Matpower.

The network data dictionary and the DC power flow solver have been used for the cascading failure simulations presented in Chapter 6. Further, the AC power flow solver is deployed by `PowerDynamics.jl` for calculating the static steady-state solutions.

⁴<https://github.com/lanl-ansi/PowerModels.jl>

References

- [1] 50Hertz, Amprion, Tennet, Transnet BW. Need to develop grid-forming statcom systems – position paper of the german transmission system operators, December 2020.
- [2] Agora Energiewende. Energiewende und Dezentralität – Zu den Grundlagen einer politisierten Debatte, February 2017.
- [3] Y. Aizawa. Synergetic approach to the phenomena of mode-locking in nonlinear systems. *Progress of theoretical physics*, 56(3):703–716, 1976.
- [4] H. Alatrash, A. Mensah, E. Mark, G. Haddad, and J. Enslin. Generator emulation controls for photovoltaic inverters. *IEEE Transactions on Smart Grid*, 3(2):996–1011, 2012.
- [5] Amprion. Underground cables in the transmission grid – an innovative technology for grid expansion, July 2017.
- [6] P. M. Anderson and A. A. Fouad. *Power system control and stability*. John Wiley & Sons, 2003.
- [7] M. Andreasson, E. Tegling, H. Sandberg, and K. H. Johansson. Coherence in synchronizing power networks with distributed integral control. In *2017 IEEE 56th Annual Conference on Decision and Control (CDC)*, pages 6327–6333. IEEE, 2017.
- [8] M. Anvari, G. Lohmann, M. Wächter, P. Milan, E. Lorenz, D. Heinemann, M. R. R. Tabar, and J. Peinke. Short term fluctuations of wind and solar power systems. *New Journal of Physics*, 18(6):063027, 2016.
- [9] M. Anvari, M. Tabar, J. Peinke, and K. Lehnertz. Disentangling the stochastic behavior of complex time series. *Scientific reports*, 6(1):1–12, 2016.
- [10] M. Anvari, B. Werther, G. Lohmann, M. Wächter, J. Peinke, and H.-P. Beck. Suppressing power output fluctuations of photovoltaic power plants. *Solar Energy*, 157:735–743, 2017.

- [11] M. Ardelean and P. Minnebo. HvdC submarine power cables in the world. Publications Office of the European Union, 2015.
- [12] A. Arenas, A. Díaz-Guilera, J. Kurths, Y. Moreno, and C. Zhou. Synchronization in complex networks. *Physics reports*, 469(3):93–153, 2008.
- [13] S. Auer. *The stability and control of power grids with high renewable energy share*. PhD thesis, Humboldt-Universität zu Berlin, 2018.
- [14] S. Auer, F. Hellmann, M. Krause, and J. Kurths. Stability of synchrony against local intermittent fluctuations in tree-like power grids. *Chaos: An Interdisciplinary Journal of Nonlinear Science*, 27(12):127003, 2017.
- [15] S. Auer, F. Steinke, W. Chunsen, A. Szabo, and R. Sollacher. Can distribution grids significantly contribute to transmission grids’ voltage management? In *2016 IEEE PES Innovative Smart Grid Technologies Conference Europe (ISGT-Europe)*, pages 1–6. IEEE, 2016.
- [16] L. A. Avila. Tropical cyclone report: Tropical storm hermine. *National Hurricane Center*, November 2010.
- [17] G. Aznar-Siguan and D. N. Bresch. Climada v1: a global weather and climate risk assessment platform. *Geoscientific Model Development*, 12(7):3085–3097, 2019.
- [18] R. Baile and J.-F. Muzy. Spatial intermittency of surface layer wind fluctuations at mesoscale range. *Physical review letters*, 105(25):254501, 2010.
- [19] A.-L. Barabási and R. Albert. Emergence of scaling in random networks. *Science*, 286(5439):509–512, 1999.
- [20] H.-P. Beck and R. Hesse. Virtual synchronous machine. In *2007 9th International Conference on Electrical Power Quality and Utilisation*, pages 1–6. IEEE, 2007.
- [21] R. Berg. Tropical cyclone report: Hurricane ike. *National Hurricane Center*, January 2009.
- [22] J. Beven. Tropical cyclone report: Hurricane claudette. *National Hurricane Center*, September 2003.
- [23] J. Bezanson, A. Edelman, S. Karpinski, and V. B. Shah. Julia: A fresh approach to numerical computing. *SIAM review*, 59(1):65–98, 2017.
- [24] A. B. Birchfield, T. Xu, K. M. Gegner, K. S. Shetye, and T. J. Overbye. Grid structural characteristics as validation criteria for synthetic networks. *IEEE Transactions on power systems*, 32(4):3258–3265, 2016.

- [25] Birchfield et al. ACTIVSg2000: 2000-bus synthetic grid on footprint of texas. Electric Grid Test Case Repository (Texas A&M University).
- [26] F. Blaabjerg. *Control of Power Electronic Converters and Systems: Volume 2*, volume 2. Academic Press, 2018.
- [27] E. S. Blake and D. A. Zelinsky. Tropical cyclone report: Hurricane harvey. *National Hurricane Center*, May 2018.
- [28] M. Blondeel, T. Van de Graaf, and T. Haesebrouck. Moving beyond coal: exploring and explaining the powering past coal alliance. *Energy Research & Social Science*, 59:101304, 2020.
- [29] P. Bojek and H. Bahar. Hydropower. *International Energy Agency*, November 2021.
- [30] D. P. Brown, R. Berg, and B. Reinhart. Tropical cyclone report: Hurricane hanna. *National Hurricane Center*, February 2021.
- [31] T. W. Brown, T. Bischof-Niemz, K. Blok, C. Breyer, H. Lund, and B. V. Mathiesen. Response to ‘burden of proof: A comprehensive review of the feasibility of 100% renewable-electricity systems’. *Renewable and sustainable energy reviews*, 92:834–847, 2018.
- [32] E. Brunken, S. Mischinger, J. Willke, C. Wagner, M. Greve, M. Tretschock, S. Kippelt, J. Maasmann, T. Wohlfahrt, U. Häger, and C. Rehtanz. dena-Studie Systemsicherheit 2050. Deutsche Energie-Agentur, 2020.
- [33] A. Büttner, H. Würfel, A. Plietzsch, M. Lindner, and F. Hellmann. An open source software stack for tuning the dynamical behavior of complex power systems. In *Proceedings of OSMSES 2022*. IEEE, 2022.
- [34] M. C. Chandorkar, D. M. Divan, and R. Adapa. Control of parallel connected inverters in standalone ac supply systems. *IEEE transactions on industry applications*, 29(1):136–143, 1993.
- [35] E. A. A. Coelho, P. C. Cortizo, and P. F. D. Garcia. Small-signal stability for parallel-connected inverters in stand-alone ac supply systems. *IEEE Transactions on Industry Applications*, 38(2):533–542, 2002.
- [36] C. Coffrin, R. Bent, K. Sundar, Y. Ng, and M. Lubin. Powermodels.jl: An open-source framework for exploring power flow formulations. In *2018 Power Systems Computation Conference (PSCC)*, pages 1–8. IEEE, 2018.
- [37] L. Cozzi, T. Gould, S. Bouckart, D. Crow, T. Kim, C. Mcglade, P. Olejarnik, B. Wanner, and D. Wetzel. World energy outlook 2020. *International Energy Agency*, 2020.

- [38] I. Dobson, B. A. Carreras, and D. E. Newman. A loading-dependent model of probabilistic cascading failure. *Probability in the Engineering and Informational Sciences*, 19(1):15–32, 2005.
- [39] I. Dobson and H.-D. Chiang. Towards a theory of voltage collapse in electric power systems. *Systems & Control Letters*, 13(3):253–262, 1989.
- [40] F. Dörfler, M. Chertkov, and F. Bullo. Synchronization in complex oscillator networks and smart grids. *Proceedings of the National Academy of Sciences*, 110(6):2005–2010, 2013.
- [41] W. Duesterhoeft, M. W. Schulz, and E. Clarke. Determination of instantaneous currents and voltages by means of alpha, beta, and zero components. *Transactions of the American Institute of Electrical Engineers*, 70(2):1248–1255, 1951.
- [42] ENTSO-E. High penetration of power electronic interfaced power sources – guidance document for national implementation for network codes on grid connection, March 2017.
- [43] ENTSO-E. Outage of french-spanish interconnection on 24 july 2021 (update), August 2021.
- [44] ENTSO-E. System separation in the continental europe synchronous area on 8 january 2021 (2nd update), January 2021.
- [45] C. B. Field, V. Barros, T. F. Stocker, and Q. Dahe. *Managing the risks of extreme events and disasters to advance climate change adaptation: special report of the intergovernmental panel on climate change*. Cambridge University Press, 2012.
- [46] G. Filatrella, A. H. Nielsen, and N. F. Pedersen. Analysis of a power grid using a kuramoto-like model. *The European Physical Journal B*, 61(4):485–491, 2008.
- [47] C. W. Gardiner et al. *Handbook of stochastic methods*, volume 3. springer Berlin, 1985.
- [48] L. R. Gorjão, R. Jumar, H. Maass, V. Hagenmeyer, G. C. Yalcin, J. Kruse, M. Timme, C. Beck, D. Witthaut, and B. Schäfer. Open database analysis of scaling and spatio-temporal properties of power grid frequencies. *Nature communications*, 11(1):1–11, 2020.
- [49] C. Grigg, P. Wong, P. Albrecht, R. Allan, M. Bhavaraju, R. Billinton, Q. Chen, C. Fong, S. Haddad, S. Kuruganty, et al. The ieee reliability test system-1996. a report prepared by the reliability test system task force of the application of probability methods subcommittee. *IEEE Transactions on power systems*, 14(3):1010–1020, 1999.

- [50] H. Haehne, J. Schottler, M. Waechter, J. Peinke, and O. Kamps. The footprint of atmospheric turbulence in power grid frequency measurements. *EPL (Europhysics Letters)*, 121(3):30001, 2018.
- [51] R. Heffron, M.-F. Körner, J. Wagner, M. Weibelzahl, and G. Fridgen. Industrial demand-side flexibility: A key element of a just energy transition and industrial development. *Applied Energy*, 269:115026, 2020.
- [52] F. Hellmann, P. Schultz, C. Grabow, J. Heitzig, and J. Kurths. Survivability of deterministic dynamical systems. *Scientific reports*, 6(1):1–12, 2016.
- [53] F. Hellmann, P. Schultz, P. Jaros, R. Levchenko, T. Kapitaniak, J. Kurths, and Y. Maistrenko. Network-induced multistability through lossy coupling and exotic solitary states. *Nature communications*, 11(1):1–9, 2020.
- [54] F. Hellmann, E. Zolotarevskaia, J. Kurths, and J. Raisch. Probabilistic behavioral distance and tuning-reducing and aggregating complex systems. *arXiv preprint arXiv:2111.12521*, 2021.
- [55] D. Hill and A. Bergen. Stability analysis of multimachine power networks with linear frequency dependent loads. *IEEE Transactions on Circuits and Systems*, 29(12):840–848, 1982.
- [56] P. Hines, J. Apt, and S. Talukdar. Trends in the history of large blackouts in the united states. In *2008 IEEE Power and Energy Society General Meeting-Conversion and Delivery of Electrical Energy in the 21st Century*, pages 1–8. IEEE, 2008.
- [57] G. Holland. A revised hurricane pressure–wind model. *Monthly Weather Review*, 136(9):3432–3445, 2008.
- [58] F. Holz, A. Roth, R. Sogalla, F. Meißner, G. Zachmann, B. McWilliams, C. Kemfert, et al. Zukunft des europäischen energiesystems: Die zeichen stehen auf strom. *DIW Wochenbericht*, 89(6):75–82, 2022.
- [59] International Energy Agency. Global energy review: CO₂ emissions in 2021, March 2022.
- [60] B. Johnson, M. Rodriguez, M. Sinha, and S. Dhople. Comparison of virtual oscillator and droop control. In *2017 IEEE 18th Workshop on Control and Modeling for Power Electronics (COMPEL)*, pages 1–6. IEEE, 2017.
- [61] B. B. Johnson, M. Sinha, N. G. Ainsworth, F. Dörfler, and S. V. Dhople. Synthesizing virtual oscillators to control islanded inverters. *IEEE Transactions on Power Electronics*, 31(8):6002–6015, 2015.

- [62] R. Jumar, H. Maaß, B. Schäfer, L. R. Gorjão, and V. Hagenmeyer. Power grid frequency data base. *arXiv preprint arXiv:2006.01771*, 2020.
- [63] C. King, J. D. Rhodes, J. Zarnikau, N. Lin, E. Kutanoglu, B. Leibowicz, D. Niyogi, V. Rai, S. Santoso, D. Spence, et al. The timeline and events of the february 2021 texas electric grid blackouts. *The University of Texas Energy Institute*, 2021.
- [64] D. P. Kingma and J. Ba. Adam: A method for stochastic optimization. *arXiv preprint arXiv:1412.6980*, 2014.
- [65] R. D. Knabb. Tropical cyclone report: Tropical storm erin. *National Hurricane Center*, April 2008.
- [66] K. R. Knapp, H. J. Diamond, J. P. Kossin, M. C. Kruk, C. Schreck, et al. International best track archive for climate stewardship (ibtracs) project, version 4. *NOAA National Centers for Environmental Information*, 2018.
- [67] K. R. Knapp, M. C. Kruk, D. H. Levinson, H. J. Diamond, and C. J. Neumann. The international best track archive for climate stewardship (ibtracs) unifying tropical cyclone data. *Bulletin of the American Meteorological Society*, 91(3):363–376, 2010.
- [68] R. Kogler, A. Plietzsch, P. Schultz, and F. Hellmann. Normal form for grid-forming power grid actors. *PRX Energy*, 1(1):013008, 2022.
- [69] S. M. Krause, S. Börries, and S. Bornholdt. Econophysics of adaptive power markets: When a market does not dampen fluctuations but amplifies them. *Physical Review E*, 92(1):012815, 2015.
- [70] Y. Kuramoto. International symposium on mathematical problems in theoretical physics. *Lecture notes in Physics*, 30:420, 1975.
- [71] Y. Kuramoto. *Chemical oscillations, waves, and turbulence*. Courier Corporation, 2003.
- [72] T. Lagos, R. Moreno, A. N. Espinosa, M. Panteli, R. Sacaan, F. Ordonez, H. Rudnick, and P. Mancarella. Identifying optimal portfolios of resilient network investments against natural hazards, with applications to earthquakes. *IEEE Transactions on Power Systems*, 35(2):1411–1421, 2019.
- [73] S. Liemann, L. Streng, P. Schultz, H. Hinnert, J. Porst, M. Sarstedt, and F. Hellmann. Probabilistic stability assessment for active distribution grids. In *2021 IEEE Madrid PowerTech*, pages 1–6. IEEE, 2021.

- [74] M. Lindner, L. Lincoln, F. Drauschke, J. M. Koulen, H. Würfel, A. Plietzsch, and F. Hellmann. Networkdynamics. jl—composing and simulating complex networks in julia. *Chaos: An Interdisciplinary Journal of Non-linear Science*, 31(6):063133, 2021.
- [75] R. Lloyd. Massive power failure could finally cause texas to connect with the nation’s power grids. *Scientific American*, February 2021.
- [76] E. Lorenz and D. Heinemann. Prediction of solar irradiance and photovoltaic power. In A. Sayigh, editor, *Comprehensive Renewable Energy*, pages 239–292. Elsevier, Oxford, 2012.
- [77] Y. Ma, S. Gowda, R. Anantharaman, C. Laughman, V. Shah, and C. Rackauckas. Modelingtoolkit: A composable graph transformation system for equation-based modeling. *arXiv preprint arXiv:2103.05244*, 2021.
- [78] J. Machowski, J. W. Bialek, and J. R. Bumby. *Power system dynamics: stability and control*. John Wiley & Sons, 2008.
- [79] P. C. Matthews and S. H. Strogatz. Phase diagram for the collective behavior of limit-cycle oscillators. *Physical review letters*, 65(14):1701, 1990.
- [80] H. R. Max Roser and E. Ortiz-Ospina. World population growth. *Our World in Data*, 2013.
- [81] W. Medjroubi, U. P. Müller, M. Scharf, C. Matke, and D. Kleinhans. Open data in power grid modelling: new approaches towards transparent grid models. *Energy Reports*, 3:14–21, 2017.
- [82] P. J. Menck, J. Heitzig, N. Marwan, and J. Kurths. How basin stability complements the linear-stability paradigm. *Nature physics*, 9(2):89–92, 2013.
- [83] P. Milan, M. Wächter, and J. Peinke. Turbulent character of wind energy. *Physical review letters*, 110(13):138701, 2013.
- [84] F. Milano. *Power system modelling and scripting*. Springer Science & Business Media, 2010.
- [85] G. S. Misyris, S. Chatzivasileiadis, and T. Weckesser. Grid-forming converters: Sufficient conditions for rms modeling. *Electric Power Systems Research*, 197:107324, 2021.
- [86] A.-H. Mohsenian-Rad, V. W. Wong, J. Jatskevich, R. Schober, and A. Leon-Garcia. Autonomous demand-side management based on game-theoretic energy consumption scheduling for the future smart grid. *IEEE transactions on Smart Grid*, 1(3):320–331, 2010.

- [87] A. Morales, M. Wächter, and J. Peinke. Characterization of wind turbulence by higher-order statistics. *Wind Energy*, 15(3):391–406, 2012.
- [88] National Hurricane Center. The saffir-simpson hurricane wind scale, May 2021.
- [89] C. Nauck, M. Lindner, K. Schürholt, H. Zhang, P. Schultz, J. Kurths, I. Isenhardt, and F. Hellmann. Predicting basin stability of power grids using graph neural networks. *New Journal of Physics*, 2022.
- [90] A. Navarro-Espinosa, R. Moreno, T. Lagos, F. Ordoñez, R. Sacaan, S. Espinoza, and H. Rudnick. Improving distribution network resilience against earthquakes. In *Proceedings of the International Conference on Resilience of Transmission and Distribution Networks*. IET, 2017.
- [91] J. Nitzbon, P. Schultz, J. Heitzig, J. Kurths, and F. Hellmann. Deciphering the imprint of topology on nonlinear dynamical network stability. *New Journal of Physics*, 19(3):033029, 2017.
- [92] M. Noebels, R. Preece, and M. Panteli. Ac cascading failure model for resilience analysis in power networks. *IEEE Systems Journal*, 2020.
- [93] R. Pachauri and L. Meyer. *Climate Change 2014: Synthesis Report. Contribution of Working Groups I, II and III to the Fifth Assessment Report of the Intergovernmental Panel on Climate Change*. IPCC, Geneva, Switzerland, 2014.
- [94] G. A. Pagani and M. Aiello. The power grid as a complex network: a survey. *Physica A: Statistical Mechanics and its Applications*, 392(11):2688–2700, 2013.
- [95] R. H. Park. Two-reaction theory of synchronous machines generalized method of analysis-part i. *Transactions of the American Institute of Electrical Engineers*, 48(3):716–727, 1929.
- [96] R. J. Pasch, R. Berg, D. P. Roberts, and P. P. Papin. Tropical cyclone report: Hurricane laura. *National Hurricane Center*, May 2021.
- [97] R. C. Pietzcker, S. Osorio, and R. Rodrigues. Tightening eu ets targets in line with the european green deal: Impacts on the decarbonization of the eu power sector. *Applied Energy*, 293:116914, 2021.
- [98] E. Planas, A. Gil-de Muro, J. Andreu, I. Kortabarria, and I. M. de Alegria. Design and implementation of a droop control in d-q frame for islanded microgrids. *IET Renewable Power Generation*, 7(5):458–474, 2013.

- [99] A. Plietzsch, S. Auer, J. Kurths, and F. Hellmann. Linear response theory for renewable fluctuations in power grids with transmission losses. *arXiv preprint arXiv:1903.09585*, 2021. (In Review at Chaos: An Interdisciplinary Journal of Nonlinear Science).
- [100] A. Plietzsch, R. Kogler, S. Auer, J. Merino, A. Gil-de Muro, J. Liße, C. Vogel, and F. Hellmann. Powerdynamics.jl—an experimentally validated open-source package for the dynamical analysis of power grids. *SoftwareX*, 17:100861, 2022.
- [101] A. Plietzsch, P. Schultz, J. Heitzig, and J. Kurths. Local vs. global redundancy–trade-offs between resilience against cascading failures and frequency stability. *The European Physical Journal Special Topics*, 225(3):551–568, 2016.
- [102] B. L. Preston, S. N. Backhaus, M. Ewers, J. A. Phillips, C. A. Silva-Monroy, J. E. Dagle, A. G. Tarditi, J. Looney, and T. J. K. Jr. Resilience of the u.s. electricity system: A multi-hazard perspective. *US Department of Energy*, 2016.
- [103] H.-O. Pörtner, D. Roberts, M. Tignor, E. Poloczanska, K. Mintenbeck, A. Alegría, M. Craig, S. Langsdorf, S. Löschke, V. Möller, A. Okem, and B. Rama. *Climate Change 2022: Impacts, Adaptation, and Vulnerability. Contribution of Working Group II to the Sixth Assessment Report of the Intergovernmental Panel on Climate Change*. Cambridge University Press, 2022.
- [104] C. Rackauckas, M. Innes, Y. Ma, J. Bettencourt, L. White, and V. Dixit. DiffEqFlux.jl—a julia library for neural differential equations. *arXiv preprint arXiv:1902.02376*, 2019.
- [105] C. Rackauckas and Q. Nie. Differentialequations.jl—a performant and feature-rich ecosystem for solving differential equations in julia. *Journal of Open Research Software*, 5(1), 2017.
- [106] C. Redl and B. Praetorius. Die Sonnenfinsternis 2015: Vorschau auf das Stromsystem 2030 Herausforderungen für die Stromversorgung in Systemen mit hohen Anteilen an Wind- und Solarenergie. Agora Energiewende, 2015.
- [107] H. Ritchie and M. Roser. Energy. *Our World in Data*, 2020.
- [108] H. Ritchie and M. Roser. CO₂ and greenhouse gas emissions. *Our World in Data*, 2020.
- [109] J. Rocabert, A. Luna, F. Blaabjerg, and P. Rodriguez. Control of power converters in ac microgrids. *IEEE transactions on power electronics*, 27(11):4734–4749, 2012.

- [110] P. W. Sauer, M. A. Pai, and J. H. Chow. *Power system dynamics and stability: with synchrophasor measurement and power system toolbox*. John Wiley & Sons, 2017.
- [111] B. Schäfer, C. Beck, K. Aihara, D. Witthaut, and M. Timme. Non-gaussian power grid frequency fluctuations characterized by lévy-stable laws and superstatistics. *Nature Energy*, 3(2):119–126, 2018.
- [112] B. Schäfer, D. Witthaut, M. Timme, and V. Latora. Dynamically induced cascading failures in power grids. *Nature communications*, 9(1):1–13, 2018.
- [113] J. Schiffer, D. Goldin, J. Raisch, and T. Sezi. Synchronization of droop-controlled microgrids with distributed rotational and electronic generation. In *52nd IEEE Conference on Decision and Control*, pages 2334–2339. IEEE, 2013.
- [114] J. Schiffer, R. Ortega, A. Astolfi, J. Raisch, and T. Sezi. Conditions for stability of droop-controlled inverter-based microgrids. *Automatica*, 50(10):2457–2469, 2014.
- [115] J. Schiffer, D. Zonetti, R. Ortega, A. M. Stanković, T. Sezi, and J. Raisch. A survey on modeling of microgrids—from fundamental physics to phasors and voltage sources. *Automatica*, 74:135–150, 2016.
- [116] K. Schmietendorf, J. Peinke, and O. Kamps. The impact of turbulent renewable energy production on power grid stability and quality. *The European Physical Journal B*, 90(11):1–6, 2017.
- [117] P. Schultz, J. Heitzig, and J. Kurths. A random growth model for power grids and other spatially embedded infrastructure networks. *The European Physical Journal Special Topics*, 223(12):2593–2610, 2014.
- [118] P. C. Sen. *Principles of electric machines and power electronics*. John Wiley & Sons, 2007.
- [119] G.-S. Seo, M. Colombino, I. Subotic, B. Johnson, D. Groß, and F. Dörfler. Dispatchable virtual oscillator control for decentralized inverter-dominated power systems: Analysis and experiments. In *2019 IEEE Applied Power Electronics Conference and Exposition (APEC)*, pages 561–566. IEEE, 2019.
- [120] J. Shao. *Mathematical statistics*. Springer Science & Business Media, 2003.
- [121] M. Shiino and M. Frankowicz. Synchronization of infinitely many coupled limit-cycle type oscillators. *Physics Letters A*, 136(3):103–108, 1989.

- [122] J. W. Simpson-Porco, F. Dörfler, and F. Bullo. Synchronization and power sharing for droop-controlled inverters in islanded microgrids. *Automatica*, 49(9):2603–2611, 2013.
- [123] L. Söder, P. D. Lund, H. Koduvere, T. F. Bolkesjø, G. H. Rossebø, E. Rosenlund-Soysal, K. Skytte, J. Katz, and D. Blumberga. A review of demand side flexibility potential in northern europe. *Renewable and Sustainable Energy Reviews*, 91:654–664, 2018.
- [124] I. Staffell, D. Brett, N. Brandon, and A. Hawkes. A review of domestic heat pumps. *Energy & Environmental Science*, 5(11):9291–9306, 2012.
- [125] K. Strunz. Developing benchmark models for studying the integration of distributed energy resources. In *2006 IEEE Power Engineering Society General Meeting*, pages 2–pp. IEEE, 2006.
- [126] J. M. Stürmer. Investigating the risk of hurricane-induced cascading failures in power systems of the u.s. east coast. Master’s thesis, Technische Universität Berlin, 2022.
- [127] J. M. Stürmer, A. Plietzsch, and M. Anvari. The risk of cascading failures in electrical grids triggered by extreme weather events. In *Proceedings of ENERGY 2021*, pages 19–23. IARIA, 2021.
- [128] J. M. Stürmer, A. Plietzsch, M. Anvari, T. Vogt, C. Otto, and F. Hellmann. Hurricane-induced failures of critical transmission lines lead to huge power outages in texas, 2022. (In Preparation).
- [129] E. Tegling, M. Andreasson, J. W. Simpson-Porco, and H. Sandberg. Improving performance of droop-controlled microgrids through distributed pi-control. In *2016 American Control Conference (ACC)*, pages 2321–2327. IEEE, 2016.
- [130] E. Tegling and H. Sandberg. On the coherence of large-scale networks with distributed pi and pd control. *IEEE control systems letters*, 1(1):170–175, 2017.
- [131] C. H. Tötz, S. Olmi, and E. Schöll. Control of synchronization in two-layer power grids. *Physical Review E*, 102(2):022311, 2020.
- [132] C. Tsitouras. Runge–kutta pairs of order 5 (4) satisfying only the first column simplifying assumption. *Computers & Mathematics with Applications*, 62(2):770–775, 2011.
- [133] M. Tyloo, T. Coletta, and P. Jacquod. Robustness of synchrony in complex networks and generalized kirchhoff indices. *Physical review letters*, 120(8):084101, 2018.

- [134] M. Tyloo, L. Pagnier, and P. Jacquod. The key player problem in complex oscillator networks and electric power grids: Resistance centralities identify local vulnerabilities. *Science advances*, 5(11):eaaw8359, 2019.
- [135] United Nations Framework Convention on Climate Change (UNFCCC). The paris agreement, 2016.
- [136] C. Vogel, S. Auer, T. Deß, A. Plietzsch, and R. Kogler. Validation of low-voltage energy and renewables integration analysis. Technical report, ERIGrid, April 2020.
- [137] A. Wächter and L. T. Biegler. On the implementation of an interior-point filter line-search algorithm for large-scale nonlinear programming. *Mathematical programming*, 106(1):25–57, 2006.
- [138] Y.-h. Wan, M. Milligan, and B. Parsons. Output power correlation between adjacent wind power plants. *J. Sol. Energy Eng.*, 125(4):551–555, 2003.
- [139] E. B. Watson and A. H. Etemadi. Modeling electrical grid resilience under hurricane wind conditions with increased solar and wind power generation. *IEEE Transactions on Power Systems*, 35(2):929–937, 2019.
- [140] D. J. Watts and S. H. Strogatz. Collective dynamics of ‘small-world’ networks. *Nature*, 393(6684):440–442, 1998.
- [141] J. Winkler, L. Duenas-Osorio, R. Stein, and D. Subramanian. Performance assessment of topologically diverse power systems subjected to hurricane events. *Reliability Engineering & System Safety*, 95(4):323–336, 2010.
- [142] D. Witthaut, F. Hellmann, J. Kurths, S. Kettemann, H. Meyer-Ortmanns, and M. Timme. Collective nonlinear dynamics and self-organization in decentralized power grids. *Rev. Mod. Phys.*, 94, 2022.
- [143] C. J. Wong and M. D. Miller. Guidelines for electrical transmission line structural loading. *American Society of Civil Engineers*, 2009.
- [144] R. Wood and P. R. Field. The distribution of cloud horizontal sizes. *Journal of Climate*, 24(18):4800–4816, 2011.
- [145] X. Zhang, S. Hallerberg, M. Matthiae, D. Witthaut, and M. Timme. Fluctuation-induced distributed resonances in oscillatory networks. *Science advances*, 5(7):eaav1027, 2019.
- [146] K. Zhou and J. C. Doyle. *Essentials of robust control*, volume 104. Prentice hall Upper Saddle River, NJ, 1998.

Selbstständigkeitserklärung

Ich erkläre, dass ich die Dissertation selbständig und nur unter Verwendung der von mir gemäß § 7 Abs. 3 der Promotionsordnung der Mathematisch-Naturwissenschaftlichen Fakultät, veröffentlicht im Amtlichen Mitteilungsblatt der Humboldt-Universität zu Berlin Nr. 42/2018 am 11.07.2018 angegebenen Hilfsmittel angefertigt habe und alle Quellen angegeben habe.

Datum

Unterschrift